UNIVERSITY OF TECHNOLOGY SYDNEY

Electrical Generation, Excitation and Control of Hexagonal Boron Nitride Quantum Emitters

by Ivan Zhigulin

Thesis submitted in fulfilment of the requirements for
the degree of

Doctor of Philosophy

under the supervision of Prof. Charlene Lobo & Prof. Igor Aharonovich
and co-supervision of Dr. Mehran Kianinia & Prof. Milos Toth

University of Technology Sydney

School of Maths and Physical Sciences

April 2026

Certificate of original authorship

I, Ivan Zhigulin, declare that this thesis is submitted in fulfilment of the requirements for the award of Ph.D. in Physics, in the School of Mathematical and Physical Sciences at the University of Technology Sydney.

This thesis is wholly my own work unless otherwise referenced or acknowledged. In addition, I certify that all information sources and literature used are indicated in the thesis.

This document has not been submitted for qualifications at any other academic institution.

This research is supported by an Australian Government Research Training Program (RTP) Scholarship doi.org/10.82133/C42F-K220.

Production Note:
Signature removed prior to publication.

20 April 2026

This work is dedicated to my family

When you change the way you look at things, the things you look at change — Max Planck

Acknowledgements

I am very grateful to have completed my Ph.D. as part of the Quantum Materials & Nanophotonics group at the University of Technology Sydney, led by Prof. Igor Aharonovich and Prof. Milos Toth. I thank both for their supervision and for creating a great research environment. In particular, I thank Igor for providing me with resources, equipment, supporting travel, introducing high-level collaborators, and always being available and encouraging. I am grateful for honest mentorship, for pushing me, and for challenging me under pressure, which contributed to my personal development. I also thank him for assembling a group of exceptional researchers, including Dr Mehran Kianinia and Dr Nathan Coste, from whom I learned problem solving and logical thinking through experimental work. I am particularly thankful to Mehran for his consistent help in the lab and efficient work ethic, while preaching that Physics tells us what to do. Lastly, I thank Prof. Charlene Lobo for support and encouragement during my studies.

Benefiting from the open culture of our research group I am particularly thankful to senior group members Angus, Simon, Chi, Milad, Johnny, and Minh, who guided me through early stages of my Ph.D. by showing laboratory techniques and experiments. A special thank you goes to Dr Jake Horder for numerous help with my research projects and for teaching me Python data science. Being exactly ten years senior, Jake's approaches to scientific problem solving were exemplary and motivated me to set high standards for myself with the aim of reaching an even higher level of maturity and capability in my own career by that age. I thank all current and past members of the Quantum Materials & Nanophotonics group, this thesis would not have been possible without the collective learning, discussions, and shared experiences within the group.

I am thankful to all my collaborators and co-authors, particularly the POSTECH research group. I thank Prof. Jonghwan Kim for his support, generosity with resources and time, and for playing a role akin to a co-supervisor in making the electroluminescence work possible. I am grateful for his hospitality and for making my time in Pohang productive and enjoyable. I thank Hoyoung Jung for his dedication, long hours in the lab, and commitment to our project. My deepest thanks go to Gyuna Park for co-leading challenging projects with me and for the active involvement in experimental work and problem solving, which were essential in bringing these ideas to reality. I also thank Hoyoung and Gyuna for their kindness and support outside of work, making this collaboration both scientifically rewarding and personally enjoyable.

I also thank the technical staff at University of Technology Sydney, in particular Dr. Toby Shanley and Chad Jarolimek for assistance with equipment training and maintenance, and for ensuring access to the resources that allowed me to focus on my research.

Finally, I thank my family and Karin Yamamura for their constant support, belief in my abilities, and always being available to help when needed. I am especially grateful for their encouragement during difficult times. Lastly, thank you to all my friends for their care and support outside of work, which played an essential role throughout this journey. *The most important contributions came from people.*

Abstract

Global technological leadership is increasingly determined by the ability to develop advanced information processing and communication. Classical semiconductor technologies, which have underpinned modern electronics for decades, are approaching fundamental scaling limits and are subject to growing geopolitical constraints on fabrication capabilities. In parallel, quantum technologies have emerged as a disruptive alternative, offering to surpass classical systems in computation and secure communication, while also adding atomic-scale sensing capability. Realising these technologies in practice requires scalable, robust, and miniaturised hardware platforms designed to operate fully on-chip.

This thesis explores key building blocks necessary for quantum technologies. Here, novel van der Waals (vdW) heterostructure devices are engineered for generation, excitation, and control of quantum emitters in hexagonal boron nitride (hBN). Electrical control of emitter luminescence is achieved via the Stark effect, providing insight into defect symmetry and quantifying controllable spectral tuning. Furthermore, electroluminescence (EL) from hBN quantum emitters is demonstrated operating in a quantum tunnelling regime, bypassing conventional p–n and p–i–n junction architectures. Lastly, electrical generation of emitters is demonstrated using locally applied high electric fields, enabling site-specific generation directly within device structures. Together, these results establish experimentally viable routes towards electrically generated, controlled, and driven quantum light sources and position hBN as a promising platform for scalable quantum photonic technologies.

Curriculum Vitae

First Author Publications

* Indicates Equal Authorship

1. **Coupling nitrogen vacancy centers in silicon carbide to nanophotonic resonators**

   Ivan Zhigulin*, Konosuke Shimazaki*, Samuel M Stephens, Angus Gale, Karin Yamamura, Hark Hoe Tan, Igor Aharonovich, Mehran Kianinia

   arXiv:2602.21505 - Published 25 February 2026

2. **Multi-wavelength Spin Dynamics of Defects in Hexagonal Boron Nitride**

   Ivan Zhigulin*, Nicholas P Sloane*, Konosuke Shimazaki, Benjamin Whitefield, Jean-Philippe Tetienne, Mehran Kianinia, Igor Aharonovich

   arXiv:2602.05301 - Published 5 February 2026

3. **Photodynamics and Temperature Dependence of Single Spin Defects in Hexagonal Boron Nitride**

   Benjamin Whitefield*, Ivan Zhigulin*, Nicholas P Sloane, Jean-Philippe Tetienne, Igor Aharonovich, Mehran Kianinia

   ACS Nano, 20, 7, 6200–6207 - Published 9 February 2026

4. **Electrical Generation of Color Centers in Hexagonal Boron Nitride**

   Ivan Zhigulin*, Gyuna Park*, Karin Yamamura, Kenji Watanabe, Takashi Taniguchi, Milos Toth, Jonghwan Kim, Igor Aharonovich

   ACS Applied Materials & Interfaces, 17, 16, 24129-24136 – Published 10 April 2025

5. **Narrowband electroluminescence from color centers in hexagonal boron nitride**

   Gyuna Park*, Ivan Zhigulin*, Hoyoung Jung, Jake Horder, Karin Yamamura, Yerin Han, Hyunje Cho, Hyeon-Woo Jeong, Kenji Watanabe, Takashi Taniguchi, Myungchul Oh, Gil-Ho Lee, Moon-Ho Jo, Igor Aharonovich, Jonghwan Kim

   Nano Letters 24, 48, 15268-15274 – Published 21 October 2024

6. **Stark effect of blue quantum emitters in hexagonal boron nitride**

   Ivan Zhigulin*, Jake Horder*, Viktor Ivády, Simon JU White, Angus Gale, Chi Li, Charlene J Lobo, Milos Toth, Igor Aharonovich, Mehran Kianinia

   Physical Review Applied, 19, 4, 044011 - Published 1 April 2023

7. **Photophysics of blue quantum emitters in hexagonal boron nitride**

   Ivan Zhigulin*, Karin Yamamura*, Viktor Ivády, Angus Gale, Jake Horder, Charlene J Lobo, Mehran Kianinia, Milos Toth, Igor Aharonovich

   Materials for Quantum Technology, 3, 1, 015002 - Published 7 March 2023

Co-Author Publications

1. **Facile Van der Waals hBN Encapsulation and Stabilization of Perovskite Quantum Dots Emission**

   Jiyun Kim, Karin Yamamura, Jake Horder, Jehyeok Ryu, Ivan Zhigulin, Nathan Coste, Alexey Y Nikitin, Yury Rakovich, Igor Aharonovich

   Advanced Functional Materials, 36, 23, e27591 – Published 31 December 2025

2. **Nanoscale patterning of epitaxial $La_{0.67}Sr_{0.33}MnO_3$ films by XeF_2 gas assisted electron beam etching**

   Jeremy Hyams, Karin Yamamura, Ivan Zhigulin, Charlene Lobo

   Under review

3. **An Inverse-Design Wavelength Demultiplexer for On-Chip Photoluminescence Sorting in TMDC Heterostructures**

   Anastasiia Zalogina, Chi Li, Ivan Zhigulin, Nathan Coste, Hossein Alijani, Otto Cranwell Schaeper, Hugo Charlton, Joseph Ward, Haoran Ren, Igor Aharonovich

   ACS Photonics, 12, 7, 3901-3908 – Accepted 16 July 2025

4. **Toward Emission Enhancement of Blue Emitters in hBN Using Plasmonic Lattices**

   Karin Yamamura, Shu An, Ivan Zhigulin, Mehran Kianinia, Yiming Wu, Zhaogang Dong, Igor Aharonovich

   ACS Applied Optical Materials, 3, 1, 64-69 – Accepted 17 December 2024

5. **Manipulating the charge state of spin defects in hexagonal boron nitride**

   Angus Gale, Dominic Scognamiglio, Ivan Zhigulin, Benjamin Whitefield, Mehran Kianinia, Igor Aharonovich, Milos Toth

   Nano Letters, 23, 13, 6141-6147 – Accepted 26 June 2023

Conference proceedings

1. **Electroluminescence from isolated colour centres in hexagonal boron nitride**

   Gyuna Park, Ivan Zhigulin, Hoyoung Jung, Jake Horder, Karin Yamamura, Yerin Han, Hyunje Cho, Hyeon-Woo Jeong, Kenji Watanabe, Takashi Taniguchi, Myungchul Oh, Gil-Ho Lee, Moon-Ho Jo, Igor Aharonovich, Jonghwan Kim

   CLEO-PR 2024, Technical Digest Series (Optica Publishing Group, 2024), paper PDP_2

2. **Room Temperature Electroluminescence from Isolated Colour Centres in Van Der Waals Semiconductors**

   Gyuna Park, Ivan Zhigulin, Hoyoung Jung, Jake Horder, Karin Yamamura, Yerin Han, Hyunje Cho, Hyeon-Woo Jeong, Kenji Watanabe, Takashi Taniguchi, Myungchul Oh, Gil-Ho Lee, Moon-Ho Jo, Igor Aharonovich, Jonghwan Kim

   CLEO 2024, Technical Digest Series (Optica Publishing Group, 2024), paper FTh5B.2

Conference presentations

1. **Room temperature electroluminescence from isolated colour centres in van der Waals semiconductors**

   Gyuna Park, Ivan Zhigulin, Hoyoung Jung, Jake Horder, Karin Yamamura, Yerin Han, Hyunje Cho, Hyeon-Woo Jeong, Kenji Watanabe, Takashi Taniguchi, Myungchul Oh, Gil-Ho Lee, Moon-Ho Jo, Igor Aharonovich, Jonghwan Kim

   IEEE, 2024 Conference on Lasers and Electro-Optics (CLEO), Charlotte NC USA

   Post Deadline Oral Presentation

2. **Near-coherent quantum emitters in hexagonal boron nitride with discrete polarization axes**

   Jake Horder, Dominic Scognamiglio, Adám Ganyecz, Viktor Ivády, Nathan Coste, Mehran Kianinia, Milos Toth, and Igor Aharonovich

   Presenter: Ivan Zhigulin

   IEEE, 2024 Conference on Lasers and Electro-Optics (CLEO), Charlotte NC USA

   Post Deadline Oral Presentation

3. **Narrowband Electroluminescence from Colour Centres in hexagonal Boron Nitride**

   Gyuna Park, Ivan Zhigulin, Hoyoung Jung, Jake Horder, Karin Yamamura, Yerin Han, Hyunje Cho, Hyeon-Woo Jeong, Kenji Watanabe, Takashi Taniguchi, Myungchul Oh, Gil-Ho Lee, Moon-Ho Jo, Igor Aharonovich, Jonghwan Kim

   Transformative Meta Optical Systems, 2024 Meta Together Conference, Adelaide WA Australia

   Nominated Student Oral Presentation

4. **Stark Effect of Blue Quantum Emitters in Hexagonal Boron Nitride**

   Ivan Zhigulin, Jake Horder, Viktor Ivády, Simon JU White, Angus Gale, Chi Li, Charlene J Lobo, Milos Toth, Igor Aharonovich, Mehran Kianinia

   Boron Nitride Workshop, 2023, Montpellier France

   Poster Presentation

5. **Stark Effect of Blue Quantum Emitters in Hexagonal Boron Nitride**

   Ivan Zhigulin, Jake Horder, Viktor Ivády, Simon JU White, Angus Gale, Chi Li, Charlene J Lobo, Milos Toth, Igor Aharonovich, Mehran Kianinia

   Australian Institute of Physics, 2022 Congress, Adelaide SA Australia

   Oral Presentation

6. **Stark Effect of Blue Quantum Emitters in Hexagonal Boron Nitride**

   Ivan Zhigulin, Jake Horder, Viktor Ivády, Simon JU White, Angus Gale, Chi Li, Charlene J Lobo, Milos Toth, Igor Aharonovich, Mehran Kianinia

   Australian Institute of Physics, 2022 Postgraduate Awards, Sydney NSW Australia

   Oral Presentation

Awards and Recognitions

- **MIT Quantum Initiative Postdoctoral Fellowship recipient**

  Massachusetts Institute of Technology, 2026

- **Seal of Excellence for a Postdoctoral Fellowship Proposal**

  Marie Skłodowska-Curie Actions, 2026

- **Post-Thesis Scholarhip recipient of AU$3000 (single award per round)**

  University of Technology Sydney, 2026

- **Winner Student Paper of the Month**

  University of Technology Sydney, 2025

- **Selected Participant for Moiré Quantum Matter Nanofabrication Workshop at Prof. Pablo Jarillo-Herrero laboratory**

  Massachusetts Institute of Technology, 2024

- **Student SEED funding recipient of AU$2000**

  University of Technology Sydney, 2024

- **Postgraduate Awards Finalist**

  Australian Institute of Physics, 2022

- **Ph.D. scholarship recipient (3.5 years)**

  Australian Government Research Training Program, 2022

Contents

1 Introduction **1**
- 1.1 Motivation . . . 1
- 1.2 Document Structure . . . 2

2 Background & Literature Review **5**
- 2.1 Quantum Technologies . . . 5
- 2.2 Quantum Light . . . 7
  - 2.2.1 Historical Context . . . 8
  - 2.2.2 Photon Statistics . . . 8
  - 2.2.3 Coherence Functions and Photon Correlations . . . 10
- 2.3 Quantum Light Sources . . . 12
  - 2.3.1 Overview of Quantum Light Sources . . . 13
    - 2.3.1.1 Operation Principles of Defects in Wide-Bandgap Semiconductors . . . 15
- 2.4 Hexagonal Boron Nitride . . . 17
  - 2.4.1 Material Properties . . . 17
  - 2.4.2 Quantum Emitters . . . 18
    - 2.4.2.1 Overview and Challenges . . . 18
    - 2.4.2.2 Optoelectronic Device Integration . . . 20

3 Materials & Methods **23**
- 3.1 Materials . . . 23
  - 3.1.1 hBN and Graphitic Materials . . . 23
- 3.2 Experimental Methods . . . 24
  - 3.2.1 Exfoliation . . . 24

3.2.2 hBN Emitter Generation . . . 27
3.2.3 Align Transfer . . . 28
3.2.4 Lithography . . . 29
3.2.5 Metal Deposition . . . 30
3.2.6 Confocal Microscopy . . . 31

4 Electrical Control of hBN Quantum Emitters 35
4.1 Context . . . 35
4.2 Results . . . 37
4.3 Summary . . . 45

5 Electrical Excitation of hBN Quantum Emitters 47
5.1 Context . . . 47
5.2 Results . . . 48
5.3 Summary . . . 59

6 Electrical Generation of hBN Quantum Emitters 61
6.1 Context . . . 61
6.2 Results . . . 63
6.3 Summary . . . 74

7 Conclusions & Outlook 77
7.1 Thesis Summary . . . 77
7.2 Outlook and Future Directions . . . 79
7.2.0.1 Electrical Control . . . 80
7.2.0.2 Electrical Excitation . . . 81

Appendix A Stark Effect 83
A.1 Theoretical Description . . . 83

Appendix B Quantum Tunnelling 85
B.1 Charge Injection Mechanisms . . . 85
B.2 Electrical Characterisation of Emitter Generation . . . 89

Bibliography 91

List of Abbreviations

2D two-dimensional . . . 2
3D three-dimensional . . . 2
QKD quantum key distribution . . . 6
CMOS complementary metal-oxide-semiconductor . . . 13
QD quantum dot . . . 13
TMDC transition metal dichalcogenide . . . 13
NV nitrogen vacancy . . . 14
SiV silicon vacancy . . . 14
hBN hexagonal boron nitride . . . ix
vdW van der Waals . . . ix
TMDC transition metal dichalcogenides . . . 13
ZPL zero phonon line . . . 15
PSB phonon sideband . . . 15
PL photoluminescence . . . 18
NIR near-infrared . . . 18
AFM atomic force microscopy . . . 21
ODMR optically detected magnetic resonance . . . 20
PLE photoluminescence excitation . . . 35
EL electroluminescence . . . ix
FWHM full width at half maximum . . . 37
MLG multilayer graphene . . . 38
I-V current-voltage . . . 49
NIMS National Institute for Materials Science . . . 23

APD avalanche photodiode detector 34
UV ultraviolet 8
PVA polyvinyl alcohol 28
PPC polypropylene carbonate 28
PDMS polydimethylsiloxane 28
EBL electron beam lithography 29
SEM scanning electron microscope 30
PMMA polymethyl methacrylate 30
PSF point spread function 31
MFD mode field diameter 32
CVD chemical vapour deposition 18

1

Introduction

This chapter introduces the motivation, scope, and objectives of the research presented in this thesis. It outlines why the electrical generation, excitation, and control of hBN single photon emitters represents a non-trivial and timely problem, and defines the specific aims addressed in the following chapters. The chapter concludes with an overview of the thesis structure.

1.1 | Motivation

The desire to understand and control the physical world has driven scientific progress for centuries, from the formulation of classical mechanics to the development of modern electronics. At the beginning of the twentieth century, description of behaviour of matter at sub-nanometre length scales revealed that nature operates in ways that cannot be captured by classical descriptions alone and resulted in the emergence of quantum mechanics. Today, research aims to harness quantum effects, such as particle spin, superposition, and entanglement, to enable a new generation of technologies, referred to as quantum technologies. These are now actively being researched and developed by both academic and industrial communities. Of particular interest are applications in communication, computation, and sensing, which promise capabilities that extend well beyond those of classical systems. As with the early development of classical electronics, realising this vision requires new physical hardware capable of reliably generating, manipulating, and reading out quantum states.

Light plays a central role in this effort. Photons are particularly attractive carriers of quantum information due to their weak interaction with the environment and their ability to transmit quantum states over long distances. Consequently, many quantum technologies rely on precise control of light at a single photon level. Yet, generating and controlling single photons remains a non-trivial challenge. The development of practical sources of

quantum light is therefore a critical bottleneck in the advancement of scalable quantum photonic architectures. As a result, technological perspective implies a strong motivation to realise fully integrated photonic platforms in which single photons can be generated, excited, modulated, and detected fully on-chip. Ideally, single photon emitters should be created at deterministic locations with reproducible emission energies, excited electrically to minimise optical complexity, and actively tuned or controlled within a device environment. Achieving this level of integration is essential for scalable quantum photonic systems, yet remains an open challenge across many material platforms.

Among the various approaches to single photon generation, defect-based emitters in wide-bandgap semiconductors have emerged as particularly promising candidates. hBN has recently attracted significant attention as a host for bright and stable single photon emitters that operate at room temperature. As a two-dimensional (2D) wide bandgap material, hBN occupies a unique position at the intersection of quantum photonics and vdW electronics, offering opportunities for device integration and control that are difficult to realise in bulk three-dimensional (3D) materials. Importantly, this platform enables alternative charge injection strategies based on vdW heterostructures and quantum tunnelling mechanisms, bypassing conventional p–n or p–i–n junction architectures that are inherently challenging to implement in hBN due to the absence of native doping.

Despite these advantages, several fundamental and technological challenges remain. The origin of many hBN emitters is still under active investigation, deterministic generation of emitters with controlled properties remains elusive, and methods for electrical excitation are only beginning to emerge. Addressing these challenges is essential for transforming hBN single photon emitters from laboratory demonstrations into practical building blocks for integrated quantum photonic systems. This thesis is therefore motivated by the need to establish experimentally viable routes for the electrical generation, excitation, and control of hBN single photon emitters within scalable vdW device architectures.

1.2 | Document Structure

This thesis is organised to progressively develop the conceptual background, experimental methodology, and original contributions required to establish electrical generation, excitation, and control of single photon emitters in hBN.

Chapter 2 presents the theoretical background and literature review necessary to contextualise this work. It introduces the broader landscape of quantum technologies and the role of single-photon emitters as enabling hardware components. Fundamental concepts of quantum light are developed through photon statistics and coherence functions,

alongside experimental methods for verifying non-classical emission. The chapter then surveys solid-state single photon emitters, with particular emphasis on defect-based systems in wide-bandgap materials, and positions hBN as a promising platform for quantum photonic architectures.

Following, **Chapter 3** describes the experimental techniques and device fabrication methods employed throughout this thesis. It outlines the exfoliation, transfer, and assembly of vdW heterostructures, alongside lithography and metal deposition procedures used to realise electrically contacted devices. The chapter also introduces the optical characterisation techniques, particularly confocal microscopy and its operating principles, which form the basis for identifying and analysing single photon emitter characteristics under both optical and electrical excitation.

Chapter 4 focuses on the electrical control of hBN single photon emitters via the Stark effect. Specifically, B-centre emitters are integrated into tailored vdW device geometries that enable controlled application of in-plane and out-of-plane electric fields. Resonant excitation spectroscopy is used to probe field-induced energy shifts, providing insight into defect symmetry and origin, while establishing electrical tuning as a viable route for spectral alignment of emitters.

Chapter 5 demonstrates electrically driven single-photon emission from hBN emitters. Graphene–hBN–graphene heterostructures are engineered to sustain extremely high electric fields, allowing charge injection via quantum tunnelling rather than conventional junction-based architectures. The resulting EL is shown to be spectrally narrow, stable up to room temperature, polarised, and of quantum nature, promoting hBN as a viable platform for electrically excited quantum light sources.

Subsequently, **Chapter 6** investigates the site-specific electrical generation of single photon emitters in hBN through high-field operation of multi-slot vdW devices. This chapter analyses defect formation induced by electrical stress, identifies device operating regimes that enable stable, prolonged electrical excitation, and outlines guidelines for optimum signal-to-noise ratio of emitter EL. The results demonstrate a viable pathway towards on-chip generation of single photon emitters directly within fabricated devices, enabling subsequent electrical tuning and operation without the need for external irradiation or high-temperature annealing.

Finally, **Chapter 7** summarises the main achievements of the thesis and discusses their broader implications for quantum photonic technologies. Future research directions are outlined, including electrically tunable emitter–cavity coupling, electrically driven spin readout and control.

2

Background & Literature Review

This chapter introduces avenues of emerging quantum technologies, showing how they can be realised with single photons and quantum states hosted in solid-state materials. It outlines the photon statistics and coherence functions required to characterise single-photon emission, and surveys the landscape of solid-state emitters, with particular emphasis on wide-bandgap defect-based systems. The chapter then presents hBN as a material platform explored in this thesis for implementing next-generation quantum photonic architectures.

2.1 | Quantum Technologies

Optical technologies based on classical light sources, such as lasers and light emitting diodes, have revolutionised the telecommunications infrastructure and modern devices and today form the backbone of the internet. Now, the currently unravelling quantum revolution aims to harness quantum properties of matter and light to enable a completely new class of technologies (Figure 2.1) [1, 2], which demand sources of non-classical light, also referred to as quantum light that is comprised of a stream of single photons [3, 4]. Many of these quantum technologies rely on single photon emitter systems, particularly in the solid-state [5, 6], which can interface with atomic spins [7] enabling a broad range of novel applications including sensing [8] and storage [9].

Quantum computing is one of the most developed and highly publicised frontiers of the quantum technology landscape [10]. Unlike classical computers, which encode information in binary bits (0 or 1) using transistor-based logic gates, quantum computers use quantum bits (qubits) that can exist in superpositions of 0 and 1. This property, combined with entanglement, allows for exponentially greater computational power in solving specific classes of problems. Among various physical realisations, photons are particularly attractive as qubits for optical quantum computing, where quantum gates are implemented through interfer-

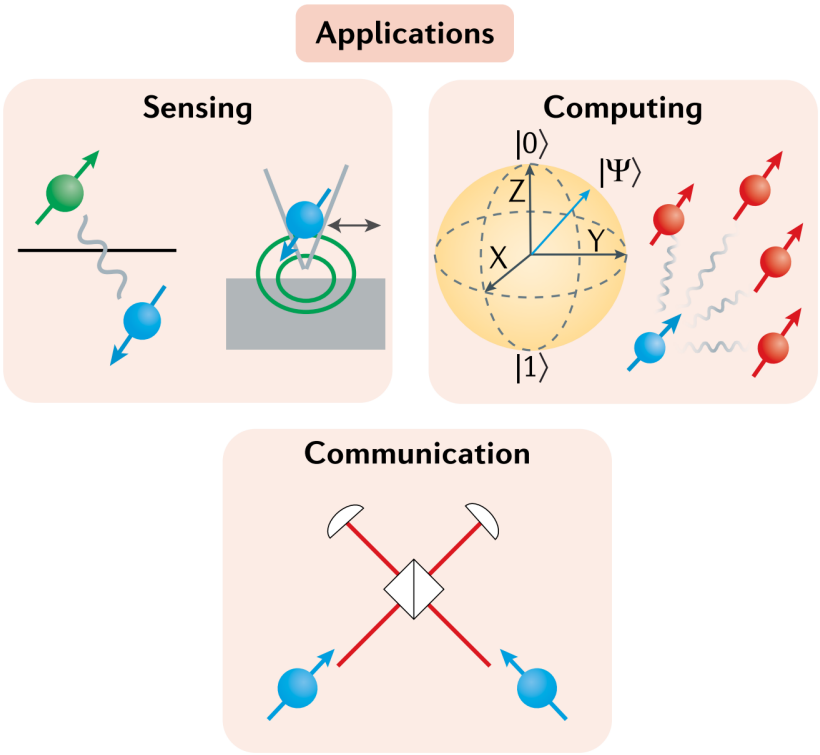


Figure 2.1: ***Quantum technology applications.*** *Illustrations of quantum sensing, computation, and communication as the three main aspects of technological applications. Reproduced from reference [5].*

ence and entanglement of indistinguishable single photons [4, 11, 12]. However, achieving fault-tolerant quantum computation requires single photons to be generated deterministically, with reproducible wavelength, high purity and indistinguishability. Nevertheless, in recent years, photonic quantum computing has driven substantial investment, with startups such as PsiQuantum [13], Quandela [11], and Xanadu [14] developing their own architectures, while major technology companies including Google [15], IBM [16], and Microsoft [17] pursue approaches based on superconducting qubits and other solid-state platforms.

In quantum communication, the most mature application is quantum key distribution (QKD), which uses single photons to securely transmit encryption keys between two parties [18, 19]. Since any attempt at interception disturbs the quantum state and introduces errors, QKD offers a level of security unattainable with classical channels. The concept relies on having exactly one photon per time bin, necessitating the use of true single-photon emitters [5, 7]. When implemented in solid-state systems, single-photon emitters can also offer spin control and memory capabilities. Spin-photon interfaces where a stationary qubit (e.g., an atomic spin associated with a nearby emitter) is coherently coupled to a flying qubit

(a single photon), forming long-distance quantum networks [7, 20]. They allow quantum information to be stored in long-lived atomic spin states [21], entangled via photon interference [22], thus enabling qubit teleportation across distributed nodes [23]. Such systems significantly advance modern communication technologies.

Quantum sensing represents another frontier of quantum technology, offering sensitivity that surpasses existing technologies. Spin-active single-photon emitters can act as atomic-scale sensors, as their spin states are highly susceptible to changes in the local environment. This sensitivity enables precise measurements of magnetic [24] and electric fields [25–27], current flow [28, 29], pressure and temperature at the nanoscale [30, 31]. These capabilities have also led to the emergence of dedicated quantum sensing companies such as Qnami [32], which leverage spin-based quantum systems for applications in materials science and bioimaging.

Deterministically generating and harnessing single photons unlocks a wide range of novel technologies based on quantum light–matter interactions. Single photons serve as essential building blocks across all three aspects of quantum technologies, enabling secure communication, high-speed computation, and atomic-scale sensing. The following section explores in detail the definition of single photons, their mathematical description, and the physical systems used to emit them.

2.2 | Quantum Light

Single-photons, also referred to as quantum light, are electromagnetic fields whose properties cannot be fully described by classical electrodynamics. Of particular importance is the generation of such single-photons, light fields composed of individual quanta, which as discussed earlier, serve as fundamental building blocks for quantum communication, computation, and sensing. In many applications, the emitted photons must also be indistinguishable, meaning sharing identical energy and polarisation.

Given the critical role of quantum light in emerging quantum technologies, significant research over the past two decades has been dedicated to developing efficient, robust, and scalable single-photon sources. This section will first outline the historical emergence of quantum light, introduce the key statistical properties of photon emission, and describe experimental methods for verifying true single-photon behaviour via intensity correlation measurements.

2.2.1 | Historical Context

At the beginning of the 20th century, light was still regarded purely as a continuous electromagnetic wave, fully described by Maxwell's equations. However, this classical view led to a major theoretical problem: it predicted that a blackbody should emit infinite energy at ultraviolet (UV) frequencies, often recalled as the *ultraviolet catastrophe*. Yet, experimental observations clearly contradicted this prediction, revealing a finite spectral profile instead.

In 1900, Max Planck introduced the idea that electromagnetic energy could only be emitted or absorbed in discrete packets, or quanta, proportional to the light's frequency [33]. This quantisation assumption is expressed as:

$$E = nhv \tag{2.1}$$

where E is the energy, h is Planck's constant, v is the frequency, and n is an integer representing the number of quanta. While this relation does not fully describe spectral distribution of blackbody radiation, it successfully resolved the ultraviolet catastrophe and was initially regarded as a mathematical necessity rather than as a fundamental property of nature.

A more profound shift came with Albert Einstein's explanation of the photoelectric effect in 1905 [34]. By proposing that light itself consists of discrete particles, or photons, Einstein provided a theoretical explanation consistent with experimental observations of the quantised nature of electromagnetic fields. His work demonstrated that the energy of ejected electrons depends on the photon energy, not on the intensity of the light wave, fundamentally challenging the classical wave model. This discovery laid the groundwork for the development of quantum mechanics and ushered in a deeper understanding of the dual wave-particle nature of light [35].

Today, it is understood that light can exhibit both classical and quantum behaviour depending on how it is measured. Many phenomena, such as laser emission, are often approximated by classical electromagnetic theory, while others, such as single-photon generation, antibunching, and quantum entanglement, require a fully quantum description. As the goal of this thesis is the study and engineering of quantum light sources, the next section introduces photon statistics that distinguish classical from quantum regimes.

2.2.2 | Photon Statistics

When considering a stream of photons, their temporal characteristics can be used to statistically classify the nature of their source. Photon statistics describe the probability distribution of detecting a given number of photons within a defined time window and distinguish between classical and non-classical light. These statistics are revealed through repeated observations of intensity fluctuations and photon arrival times, and form the basis for classifying

emission into three primary regimes: **super-Poissonian** (thermal), **Poissonian** (coherent), and **sub-Poissonian** (includes single-photon states) light.

Super-Poissonian light, such as that emitted from an incandescent bulb or blackbody radiator, is chaotic in nature and consists of many incoherent electromagnetic modes fluctuating in phase and amplitude. The resulting photon bunching behaviour, where photons tend to arrive together in time, is described by a Bose–Einstein distribution:

$$P_n = \frac{\bar{n}^n}{(1+\bar{n})^{n+1}}, \tag{2.2}$$

where $\bar{n}$ is the mean photon number. This distribution exhibits large fluctuations ($\Delta n^2 = \bar{n} + \bar{n}^2$), making the variance greater than the mean, characteristic of super-Poissonian statistics.

Poissonian light, most commonly emitted by lasers, exhibits no amplitude or phase fluctuations over time. Nevertheless, the number of photons in a coherent state fluctuates and follows a Poisson distribution:

$$P_n = \frac{\bar{n}^n e^{-\bar{n}}}{n!}. \tag{2.3}$$

In this case, the variance equals the mean ($\Delta n^2 = \bar{n}$), indicating that photons are uncorrelated, neither bunched nor antibunched, and the intensity noise scales with the square root of photon number.

Sub-Poissonian light is characterised by reduced photon number fluctuations ($\Delta n^2 < \bar{n}$), indicating non-classical emission where photons are more regularly spaced in time. A prominent example is a single-photon (Fock) state, for which the photon number is fixed. In the ideal case:

$$P_n = \begin{cases} 1 & \text{for } n = 1, \\ 0 & \text{for } n \neq 1, \end{cases} \tag{2.4}$$

This represents perfect antibunching and is a key requirement for quantum communication and computing applications that rely on one photon per time bin.

Experimentally, distinguishing between statistical regimes, especially sub-Poissonian light, is complicated by optical losses, background noise, detector inefficiencies, and limited time resolution. These factors make photon number statistics alone insufficient, particularly at low photon flux. To overcome this, time-resolved correlation measurements between photon detection events are used. This leads to the formalism of intensity correlation functions, that provide quantitative metrics for identifying bunching, antibunching, and coherent light sources, and will be discussed in the following section.

2.2.3 | Coherence Functions and Photon Correlations

The statistical nature of light can be described using correlation functions, which quantify how the electromagnetic field or intensity behaves over time or space. Coherence functions express the degree of correlation between two (or more) points in the optical field. The n^{th} order coherence function describes correlations between $2n$ field values. These functions are used in both classical and quantum optics, as they characterise the coherence properties of light and enable experimental distinction between different types of light sources.

Two coherence functions are of particular importance. The first-order coherence function, $g^{(1)}(\tau)$, characterises the ability of two parts of the field to interfere and is related to the phase and amplitude stability of the light. The second-order coherence function, $g^{(2)}(\tau)$, measures the correlation between photon intensities at different times. While $g^{(1)}(\tau)$ is relevant for understanding phase coherence, relating to interference phenomena, $g^{(2)}(\tau)$ verifies the quantum nature of light. Moreover, $g^{(2)}(\tau)$ also directly probes the source, quantifies its purity, emission lifetime and reveals bunching dynamics.

Following, both $g^{(1)}(\tau)$ and $g^{(2)}(\tau)$ are derived from their classical definitions and show how they translate into the quantum formalism used to characterise light from single photon sources.

For classical electromagnetic fields, the first-order coherence function measures the correlation between the electric field at time t and at a delayed time $t + \tau$. Mathematically, it is defined as:

$$g^{(1)}(\tau) = \frac{\langle \mathbf{E}^*(t)\mathbf{E}(t+\tau)\rangle}{\langle |\mathbf{E}(t)|^2\rangle} \tag{2.5}$$

Physically, it determines whether the light field can produce interference fringes – hence it is a measure of phase coherence. An example arises from a classical monochromatic field with single polarisation along a unit vector ϵ, constant amplitude E_0, frequency ω and phase φ that is described as

$$\mathbf{E}(t) = E_0\epsilon \cdot e^{-i(\omega t-\varphi)} \tag{2.6}$$

and can be generally identified as light produced by an ideal laser. This leads to a fully coherent $g^{(1)}(\tau)$ function, expressed as $g^{(1)}(\tau) = e^{-i\omega\tau}$ that evaluates to $|g^{(1)}(\tau)| = 1$. For light sources producing incoherent photons, $|g^{(1)}(\tau)| = 0$. Thus, the decay of $g^{(1)}(\tau)$ gives the coherence time τ_c, linked to the spectral linewidth described as $\Delta\nu = \tau_c^{-1}$.

In quantum optics, light is described using the electric field operator. Since the field is quantised, instead of treating the electric field $E(t)$ as a classical wave, it is promoted to an

operator $\hat{E}(t)$ that acts on the quantum state of the field. For a single mode of the field, the positive frequency part of the electric field operator is written as:

$$\hat{E}^{(+)}(t) = \mathcal{E}\hat{a}(t) \tag{2.7}$$

and the negative frequency part as:

$$\hat{E}^{(-)}(t) = \mathcal{E}^*\hat{a}^\dagger(t) \tag{2.8}$$

Here $\hat{a}(t)$ and $\hat{a}^\dagger(t)$ are the annihilation and creation operators of photons at time t. $\mathcal{E}$ is a constant representing the field amplitude. Quantum mechanical form of the first-order coherence function is then written as:

$$g^{(1)}(\tau) = \frac{\langle \hat{\mathbf{E}}^{(-)}(t)\hat{\mathbf{E}}^{(+)}(t+\tau)\rangle}{\langle \hat{\mathbf{E}}^{(-)}(t)\hat{\mathbf{E}}^{(+)}(t)\rangle} \tag{2.9}$$

Next, the second-order coherence function is described. It characterises light intensity correlations at two time intervals separated by a delay τ. Classically, it is defined via the electric field amplitudes as:

$$g^{(2)}(\tau) = \frac{\langle \mathbf{E}^*(t)\mathbf{E}^*(t+\tau)\mathbf{E}(t)\mathbf{E}(t+\tau)\rangle}{\langle |\mathbf{E}(t)|^2\rangle^2} \tag{2.10}$$

This equation can be rearranged to express the $g^{(2)}(\tau)$ function in terms of intensities [36–38]:

$$g^{(2)}(\tau) = \frac{\langle I(t)I(t+\tau)\rangle}{\langle I(t)\rangle^2} \tag{2.11}$$

Different light sources exhibit distinct behaviour in their $g^{(2)}(\tau)$ signatures. **Thermal light** exhibits *photon bunching*, where photons arrive in clusters, leading to $g^{(2)}(0) = 2$. **Coherent light**, such as that from an ideal laser, has no correlations between detection events, resulting in $g^{(2)}(\tau) = 1$ for all τ. In contrast, **single-photon emitters** display *antibunching*, where the probability of detecting two photons simultaneously vanishes due to the quantum nature of the source. In this case, $g^{(2)}(0) = 0$ and the function rises to 1 at longer delays.

To express the second-order coherence function in quantum mechanical context, electric field operators can be replaced with their operator equivalents, giving:

$$g^{(2)}(\tau) = \frac{\langle \hat{\mathbf{E}}^{(-)}(t)\hat{\mathbf{E}}^{(-)}(t+\tau)\hat{\mathbf{E}}^{(+)}(t+\tau)\hat{\mathbf{E}}^{(+)}(t)\rangle}{\langle \hat{\mathbf{E}}^{(-)}(t)\hat{\mathbf{E}}^{(+)}(t)\rangle^2} \tag{2.12}$$

This form links the intensity correlation function directly to photon creation and annihilation processes. In terms of photon number states, the zero-delay case simplifies to:

$$g^{(2)}(0) = \frac{\langle \hat{n}(\hat{n}-1) \rangle}{\langle \hat{n} \rangle^2} \tag{2.13}$$

Which, in turn, leads to a useful classification of light sources:

$$g^2(0) \begin{cases} > 1 & \text{thermal (bunched) light} \\ = 1 & \text{coherent light} \\ = \frac{n-1}{n} & n\text{-photon Fock state (quantum)} \end{cases} \tag{2.14}$$

Antibunching is a definitive signature of non-classical light and a key figure of merit for evaluating the purity of single-photon sources. Ideally, a perfect emitter would yield $g^{(2)}(0) = 0$, although background light or multiple emitters in proximity can raise this value. For example, two single-photon sources already elevate $g^{(2)}(0)$ to 0.5.

Experimentally, the measurement of $g^{(2)}(\tau)$ is performed using a Hanbury-Brown and Twiss interferometer [39], which splits the collected light into two paths directed to separate avalanche photodiodes. Detection events are time-tagged, and correlations between the two detectors are used to construct the histogram of delay times, from which $g^{(2)}(\tau)$ is extracted.

2.3 | Quantum Light Sources

The ability to generate and control quantum light underpins the development of quantum photonic technologies. A practical quantum light source must emit non-classical states of light with high purity, brightness, and indistinguishability [5]. Over the past two decades, significant efforts have focused on identifying and engineering systems capable of producing such states on demand [9]. These include isolated atoms [40, 41], trapped ions [42, 43], quantum dots [44, 45], nonlinear methods [46, 47], and defect-based solid-state systems [20, 48–55]. Among these, the latter, colour centres in wide-bandgap semiconductors, have emerged as a promising platform due to their stability, scalability, and compatibility with nanophotonic integration.

Current technologies seek quantum emitters tailored to specific requirements; thus, no single source currently satisfies all performance metrics. Instead, different host systems and types of single-photon emitters address distinct challenges with varying degrees of success. That said, the "holy grail" remains the realisation of a stable, bright, room temperature single-photon emitter with spin, in the solid state, that is either readily integrable into

existing foundries or compatible with complementary metal-oxide-semiconductor (CMOS) platforms, and emits photons at telecommunication wavelengths.

This section introduces key classes of quantum light sources and provides a focused discussion on defect-based emitters, particularly in materials relevant to this thesis.

2.3.1 | Overview of Quantum Light Sources

As a natural starting point, early demonstrations of quantum light phenomena were carried out using isolated atomic systems, where sodium atoms were laser-trapped in high-vacuum environments [40]. The emission from such a system inherently consists of single photons, with near-ideal antibunching behaviour and long coherence times [43]. These properties established trapped atoms and ions as textbook examples of quantum emitters. However, their extreme sensitivity to environmental fluctuations, complex experimental setups, and challenging scalability limited their practicality for quantum technologies.

To overcome these limitations, the field turned to quantum dot (QD) — nanoscale semiconductor islands that confine charge carriers in all spatial dimensions. QDs offered a route toward integration and miniaturisation, while retaining single-photon emission properties [56]. They can be embedded into solid-state photonic structures such as microcavities or waveguides, enabling enhanced light extraction and on-chip integrated photonics [57, 58]. Furthermore, QDs based on well established platforms such as GaAs benefit from mature growth and fabrication techniques [59]. However, QD systems pose their own challenges. Phonon-induced dephasing becomes significant above liquid nitrogen temperatures, leading to degraded photon indistinguishability and antibunching values that fall outside the single photon regime [60]. In addition, quantum dot growth is inherently inhomogeneous, making it difficult to fabricate two identical emitters [56]. Even small variations in strain or dot size shift its emission wavelength, complicating large scale reproducibility.

To expand the range of host systems, researchers explored colloidal quantum dots [61], organic molecules [62–64], and bound excitons in 2D materials such as in transition metal dichalcogenides (TMDC) [65–68]. These systems offer the advantage of solution-processability, facile integration, and compatibility with diverse substrates. Yet, quantum emitters in those hosts often suffer from photobleaching [64, 69], blinking [70], or poor spectral stability [69], and generally require cryogenic operation to suppress linewidth broadening and maintain single photon purity [67].

In parallel, efforts emerged to harness nonlinear optical processes such as spontaneous parametric down-conversion and four-wave mixing for quantum light generation [46]. These sources probabilistically generate entangled photon pairs, which are widely used in fundamental quantum optics experiments and quantum communication protocols [71]. However,

their stochastic nature and low brightness per pulse make them unsuitable for deterministic, on-demand single-photon applications. Moreover, the requirement for post-selection or heralding reduces overall efficiency and scalability.

In response to these limitations, research expanded to defect-based solid-state emitters, particularly colour centres in wide-bandgap semiconductors [9, 72, 73]. Rather than isolating individual atoms in vacuum, these systems embed atomic-scale point defects within a rigid crystal lattice. The resulting energy level structure mimics that of an isolated atom, supporting discrete electronic transitions and enabling stable emission of single photons even at room temperature. Importantly, reproducing the same defect within a given host material allows for deterministic generation of emitters with identical energy level structures [5, 73]. As a result, the emission wavelength remains consistent across samples, an essential criterion for scalable, on-chip quantum photonic integration [74].

Significant research was given to colour centres in diamond [75], notably nitrogen vacancy (NV) [73, 74, 76, 77] and silicon vacancy (SiV) [20, 78–80], which provide optically addressable spin states, enabling applications in nanoscale sensing and quantum networks. However, diamond itself presents integration challenges due to its chemical inertness that makes nanofabrication difficult and limits development in industry standard foundries [74]. This has led to growing interest in materials with established global fabrication infrastructure (e.g., silicon [81–83]) or with materials compatible with CMOS processing (e.g., silicon carbide [31, 84, 85], gallium nitride [86–88], silicon nitride [89]). Although these materials host a range of quantum emitters, they still suffer from either non-deterministic creation or strong phonon coupling, which, as in the example of silicon, limits operation of emitters to cryogenic temperatures [81].

The recent discovery of quantum emitters in hBN provided an alternative path, particularly in 2D material quantum emitters. hBN defects offer room temperature stability [90], high purity [91, 92], accompanied by bright and narrowband emission [90, 93]. hBN itself is chemically robust, isolating from environment, can be nanofabricated into photonic structures, and, being a vdW materials, provides seamless integration into 2D materials heterostructures via deterministic stacking, making it well suited for exploring electrically and optically driven emitters incorporated into novel 2D quantum optoelectronic devices [67, 94, 95].

Since the focus of this thesis is on emitters in hBN, defects in large bandgap semiconductor, the following subsection covers operating principles and recent advances of defect-based quantum light sources.

2.3.1.1 | Operation Principles of Defects in Wide-Bandgap Semiconductors

Point defects in wide-bandgap semiconductors and insulators can localise electronic wavefunctions deep within the bandgap, forming discrete energy levels that closely resemble those of isolated atoms [5, 75]. These defects may be intrinsic (vacancies or antisites), extrinsic (substitutional dopants), or a combination of both (substitutional dopant next to a vacancy), effectively acting as artificial atoms embedded within a crystalline host [5, 96]. Their localised orbitals confine electrons or holes, enabling optical transitions of a single electron between quantised states, thus operating as a single-photon emitter. Figure 2.2a shows a defect present in hBN lattice that consists of an impurity atom next to a vacancy, thus forming sub-bandgap energy levels.

Excitation of the defect (either optical, electrical, or with electron-beam) promotes an electron from ground to an excited energetic level. The subsequent relaxation back to the ground state can produce a single photon whose energy corresponds to the energetic separation of the electronic states (see Figure 2.2b). Because the defect resides within a crystal lattice that includes vibrational modes of atoms, this process is governed by the Franck–Condon principle (demonstrated in Figure 2.2c) where electronic transitions occur much faster than nuclear motion, so the electron is excited between vibrational sublevels of the ground and excited energy states [97].

Under off-resonant optical excitation, the pump photon energy promotes an electron from the lowest vibrational sublevel of the ground energy state to a higher vibrational sublevel of the excited energy state, provided that the vibrational wavefunctions overlap sufficiently. Rapid phonon-assisted relaxation brings the electron to the lowest vibrational sublevel of the excited energy state, from which it undergoes spontaneous emission back to the ground energy state. This decay may occur directly into the lowest vibrational sublevel, producing a sharp zero phonon line (ZPL) photon, or into higher vibrational sublevels of the ground energy state, producing red-shifted phonon sideband (PSB) emission.

As a result, the photon energy corresponds not only to the difference between electronic levels but is also modulated by vibrational coupling to the crystal lattice. This leads to the appearance of a sharp ZPL accompanied by a broader PSB at lower photon energies. Debye–Waller factor measures the ratio of ZPL intensity to the total emission.

The emission profile of a system is directly related to the excited-state lifetime of an electron, typically in the range of nanoseconds for solid-state defect emitters. Lifetime and spectral linewidth are fundamentally linked through the Heisenberg uncertainty principle, which determines the lowest limit on the range of the transition energy. The relationship is expressed as:

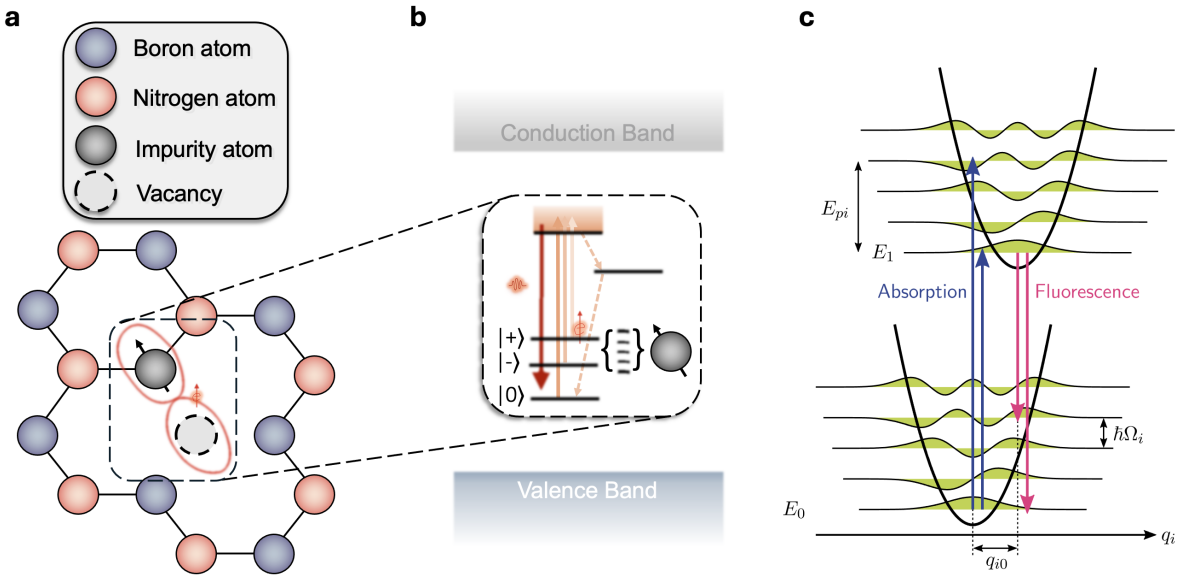


Figure 2.2: ***Illustrations of lattice defect that forms intra-bandgap energy levels and Frank-Condon diagram.*** ***(a)*** *Schematic of an example host crystal lattice, in this case hBN, which hosts a defect consisting of an impurity atom next to a vacancy, thus creating sub-bandgap energy levels.* ***(b)*** *Diagram of energy levels of a spin-active quantum emitter, where spin transitions go through a metastable state and allow interfacing with nucleus spin.* ***(c)*** *Frank-Condon diagram of energy levels, where overlaps of wavefunctions dictate probability of an electron transition between those levels during an excitation event (absorption), and subsequent photoluminescence (fluorescence) through a spontaneous electron decay, mediated via phonon transitions that give rise to PSB emission.*

$$\Delta E, \Delta t \geq \frac{\hbar}{2}, \tag{2.15}$$

which, in the frequency domain, gives the lifetime-limited (also referred to as Fourier-limited) linewidth

$$\Delta\nu_{\text{min}} = \frac{1}{2\pi\tau}, \tag{2.16}$$

where τ is the excited-state lifetime. Although, shorter lifetimes correspond to broader linewidths, they also allow higher emission rates, which are necessary for quantum photonic architectures.

In solid-state emitter systems, however, the observed linewidth often exceeds the lifetime limit due to spectral diffusion [98–100], electric noise from local charge traps [101], and electron–phonon interactions, with the latter giving rise to phonon sideband [5, 102]. These govern the resulting spectral lineshape of an emitter. The ideal lifetime-limited transition exhibits a Lorentzian lineshape, reflecting homogeneous broadening governed by the finite excited-state lifetime. Inhomogeneous broadening mechanisms such as spectral diffusion,

local charge noise, and strain fluctuations lead to a distribution of transition energies over time, resulting in a Gaussian lineshape. In practice, the observed emission profile is often described by a convolution of these effects (a Voigt profile), although in many cases it can be approximated by either a Lorentzian or Gaussian function depending on the dominant broadening mechanism.

Therefore, when investigating a single-photon emitter system, properties such as lifetime, spectral linewidth and shape, and phonon coupling jointly determine the suitability of the defect for quantum applications. Emitters with short lifetimes, narrow (ideally lifetime-limited) ZPLs, and high Debye–Waller factors are most desired as they enable bright, coherent, and spectrally pure single-photon emission. Furthermore, having metastable state and access to a nearby atomic spin adds capabilities discussed earlier in this chapter, such as sensing, quantum memory and networks.

2.4 | Hexagonal Boron Nitride

hBN is the central material platform explored throughout this thesis, serving both as a dielectric building block in vdW heterostructures and as the host for quantum emitters. It is one of the oldest known semiconductors, first synthesised in 1842 by W.H. Balmain [103]. Its appeal lies in a unique combination of properties: a wide bandgap, high chemical and thermal stability, excellent mechanical strength, high breakdown field, atomically smooth surfaces [104]. Additionally, it has strong vdW adhesion to other layered materials [105]. These characteristics make hBN a staple in vdW device fabrication; commonly used as a pickup layer for deterministic flake transfer, a protective barrier against environmental contamination, and an encapsulation layer that introduces a clean flat interface free from dangling bonds or substrate-induced charge noise [106]. These properties have also established hBN as a robust host of bright, narrowband, room-temperature quantum emitters [67, 107]. This section outlines the atomic structure and intrinsic material properties of hBN, and the optical properties of defect-based quantum emitters.

2.4.1 | Material Properties

A single layer of hBN adopts a honeycomb lattice composed of alternating boron and nitrogen atoms, forming a centrosymmetric D_{6h} crystal structure. The strong in-plane polar covalent bonds between boron and nitrogen arise from their large electronegativity difference, and result in a wide bandgap of approximately 6 eV [108–110]. Although the bandgap is indirect in bulk, the internal quantum efficiency of hBN emission can reach up to 40% [104]. In addition to its wide bandgap, hBN is also highly robust under ambient conditions and

does not oxidise even under prolonged exposure to elevated temperatures. These properties are preserved even as the number of out-of-plane hBN layers increases [109]. Adjacent layers are weakly coupled by vdW forces and generally exhibit an *AA'* stacking, where boron atoms sit above nitrogen atoms. This configuration locks layers in place, suppresses interlayer slippage, and maintains mechanical rigidity [104]. Unlike many other 2D materials, the mechanical and electronic properties of hBN remain relatively insensitive to thickness, contributing to its reliability as a dielectric material and protective layer.

While hBN exhibits excellent material properties for both photonic and electronic applications, certain challenges limit its broader scalability. Mechanical exfoliation from bulk crystals remains the primary method for obtaining high-quality, defect-free flakes, but this approach is inherently non-scalable and produces random flake sizes and thicknesses. Although chemical vapour deposition (CVD) methods have enabled the growth of large-area hBN films, these typically suffer from higher defect densities, smaller grain sizes, and lower crystallinity compared to exfoliated flakes [111, 112]. Another fundamental limitation lies in the difficulty of achieving intentional electronic doping, as no reliable method currently exists for producing stable n-type or p-type hBN [113]. Despite significant research efforts, doping remains fundamentally challenging due to the relatively deep valence band maximum and conduction band minimum of hBN, which cause most introduced impurities to form deep trap states within the bandgap [113, 114]. This poses challenges for future device designs that require active electrical control, as further explored later in this thesis. These limitations underscore the importance of exfoliated, high-quality hBN for quantum emitter studies and vdW device fabrication.

2.4.2 | Quantum Emitters

Point defects in hBN often form isolated sub-bandgap energy levels that behave as quantum emitters. Since their first observation in 2016 [115], numerous single colour centres have been reported, with emission wavelengths spanning UV to near-infrared (NIR) range. Beyond being an attractive host of very bright and stable UV emitters [116, 117], hBN also hosts three groups of quantum emitters in the visible-NIR range, which are more practical for quantum optics, and comprise of **the B-centre**, **the VB^-**, and **the visible-NIR emitters**. Each group presents distinct advantages but brings unique limitations. Example room temperature photoluminescence (PL) spectra of the three groups are presented in Figure 2.3.

2.4.2.1 | Overview and Challenges

The B-centre system offers multiple advantages, most notably its simple and high precision site-specific on-demand generation [118]. B-centres can be deterministically activated

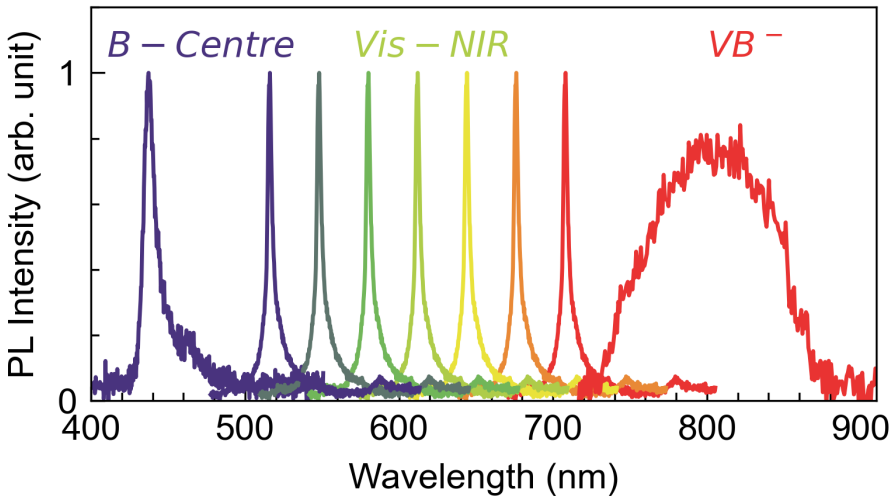


Figure 2.3: ***Room temperature PL spectra of hBN quantum emitters.*** *The B-Centre has ZPL at 436 nm and VB^- has broad emission centred around 820 nm, while other hBN emitters span visible-NIR wavelength range.*

by electron beam irradiation of hBN flakes that exhibit a characteristic triplet UV emission, detectable via cathodoluminescence[116, 119, 120]. The atomic structure of B-centre is still largely under debate, however, later in this thesis (Chapter 4) it will be shown that it consists of either nitrogen or carbon interstitial configurations. Additional advantageous properties of the B-centre include photostable emission from cryogenic to room temperatures, a highly polarised in-plane emission dipole, a high Debye–Waller factor, and coherent photon emission [118, 121, 122]. The B-centre shows a radiative lifetime of approximately 2 ns and appears to lack metastable or charge-fluctuating states [123]. However, considering the system's high-energy emission (2.72 eV, corresponding to 436 nm) it imposes significant challenges for photonic integration, as dimensions of the optical cavities must be small to efficiently couple to modes at this wavelength [124]. Despite this, the B-centre remains an attractive emitter platform due to its robustness, ease of deterministic creation, and ability to produce coherent, polarised single photons, which are promising for applications in quantum information and quantum photonic architectures.

The VB^- colour centre is currently the only hBN quantum emitter with a well established atomic structure. It consists of a missing boron atom (boron vacancy) combined with an additional electron to form a negatively charged luminescent state [125, 126]. This crystal configuration makes generation of VB^- trivial, as ion irradiation deterministically produces VB^- centres in virtually any exfoliated hBN flake [127]. The emission wavelength of VB^- lies in the NIR range. However, a significant drawback is its strong phonon coupling to

the hBN lattice, resulting in an extremely dim ZPL emission. To date, a single isolated VB^- quantum emitter has not been optically resolved. As a result, its emission spectrum remains broad at both ambient and cryogenic conditions [126]. Nevertheless, VB^- centres offer a major advantage in possessing a spin-triplet ($S = 1$) ground state and a metastable energy level, enabling optically detected magnetic resonance (ODMR). These properties allow PL measurements alongside microwave control, making the VB^- centre an atomic-scale, room-temperature quantum sensor of temperature [30], pressure [30], and strain [128]. Recently, integrating hBN VB^- with vdW heterostructures extended sensing capabilities to detection of electric and magnetic fields, and current flow within graphene channels [29, 129].

The third group is referred to as **the visible–NIR** emitters. As the name suggests, it encompasses a broad range of luminescent defects with ZPLs spanning between 400 nm and 850 nm. These centres have attracted significant interest due to their robustness, favourable emission wavelengths, short radiative lifetimes ($\sim$2 ns), highly polarised in-plane emission dipoles, high photon purity and brightness, and narrow linewidths even at room temperature [90, 93, 107, 130–132]. Many of these emitters can be activated through a variety of methods, including high-temperature annealing [131], ion irradiation [133], strain activation [134], or physical damage [135, 136], making them experimentally accessible. However, despite their practical advantages, the atomic structures responsible for most visible–NIR emission lines remain unidentified [107, 137–139]. Consequently, current generation methods lack deterministic control over emitter position, ZPL wavelength, and linewidth. In addition, visible–NIR emitters commonly exhibit spectral diffusion, charge-state instability, strong electric field sensitivity, and blinking behaviour, particularly under high excitation powers [99–101]. Although considerable progress has been made in stabilising certain emitters [140], the lack of atomic-level control still limits their reproducibility and integration into scalable quantum photonic architectures. Nevertheless, considering their excellent optical properties, and more recently, the observation of room temperature spin with long coherence times [141] in some visible–NIR centres, this group of emitters remains of high interest within the community. Thus, further investigation into their origin, properties, and deterministic generation is highly sought after.

2.4.2.2 | Optoelectronic Device Integration

Given the vdW nature of hBN, early efforts naturally focused on integrating quantum emitters into heterostructure devices to enable electrical control. Initial demonstrations primarily looked at the Stark effect to tune the ZPL energies of visible–NIR emitters. Depending on the defect configuration and local symmetry, linear, quadratic, or V-shaped Stark shifts were observed [142], reflecting the diversity of defect structures in hBN. For detailed de-

scription and mathematical interpretation of Stark effect see Appendix A.1. Further studies reported very large ZPL shifts of several nanometres that remained resolvable even at room temperature [143]. Yet again, this was only a case by case, depending on emitter. However, since the B-centre corresponds to a single defect configuration, Stark tuning provides a powerful probe of its atomic structure, an approach explored in detail in Chapter 4. Intriguingly, beyond dynamic wavelength control, vdW device architectures also offer a route towards stabilising emission linewidth by suppressing local charge noise, enabling near lifetime-limited emission, as recently demonstrated for visible hBN emitters in vertical graphene–hBN–graphene stacks [140]. These show great potential in further research of hBN emitter integration into electrical devices.

Beyond ZPL tuning, vdW heterostructure integration was also used to improve brightness and stability limitations of visible–NIR hBN emitters. Electrical gating and Fermi-level alignment were shown to enhance PL through charge-state control (see Figure 2.4a,b) [144, 146, 147], while in some cases emitter brightening was correlated with current flow [148], suggesting alternative modulation pathways and leading to more research avenues. Most device geometries employed graphite or graphene electrodes encapsulating hBN and gating through silica substrate, although comparable Stark shifts and emission enhancements were also observed using electrolyte gating [149]. Despite these advances, room-temperature electrical control of emitter brightness and the controlled emergence of multiple ZPL transitions from a single emitter remain largely unexplored. Such capabilities would be particularly attractive for wavelength-multiplexed quantum light sources and are partially addressed in Chapter 6. Recent progress in graphene nanofabrication, including atomic force microscopy (AFM) etching [150], further enables the creation of multiple independently addressable electrode gaps within a single heterostructure, allowing site-specific emitter generation across several locations in one device, a concept also explored in this thesis (Chapter 6).

Despite the rapid progress in electrical control and PL enhancement, EL from hBN quantum emitters remained largely unachievable for several years following their discovery in 2016 [115]. This stems from the lack of dopants in hBN to create p-n or p-i-n junctions for efficient charge injection. Instead, charge injection mechanism must rely on quantum tunnelling effects, bringing fabrication challenges, and necessitating high-quality heterostructures that are capable of sustaining large electric fields and current densities without degradation. Furthermore, their operation had to be reliable enough to operate for hours to conduct measurements on quantum emitters, which given the young timeline of vdW materials research, is still a highly active research area. While electrical excitation of hBN band-edge states [151] and UV defects [152] was demonstrated in graphene–hBN–graphene devices. Visible EL was recently shown in highly carbon-doped hBN (representative spectra are shown in Figure 2.4c) [145], but it was limited to cryogenic operation and was of non-

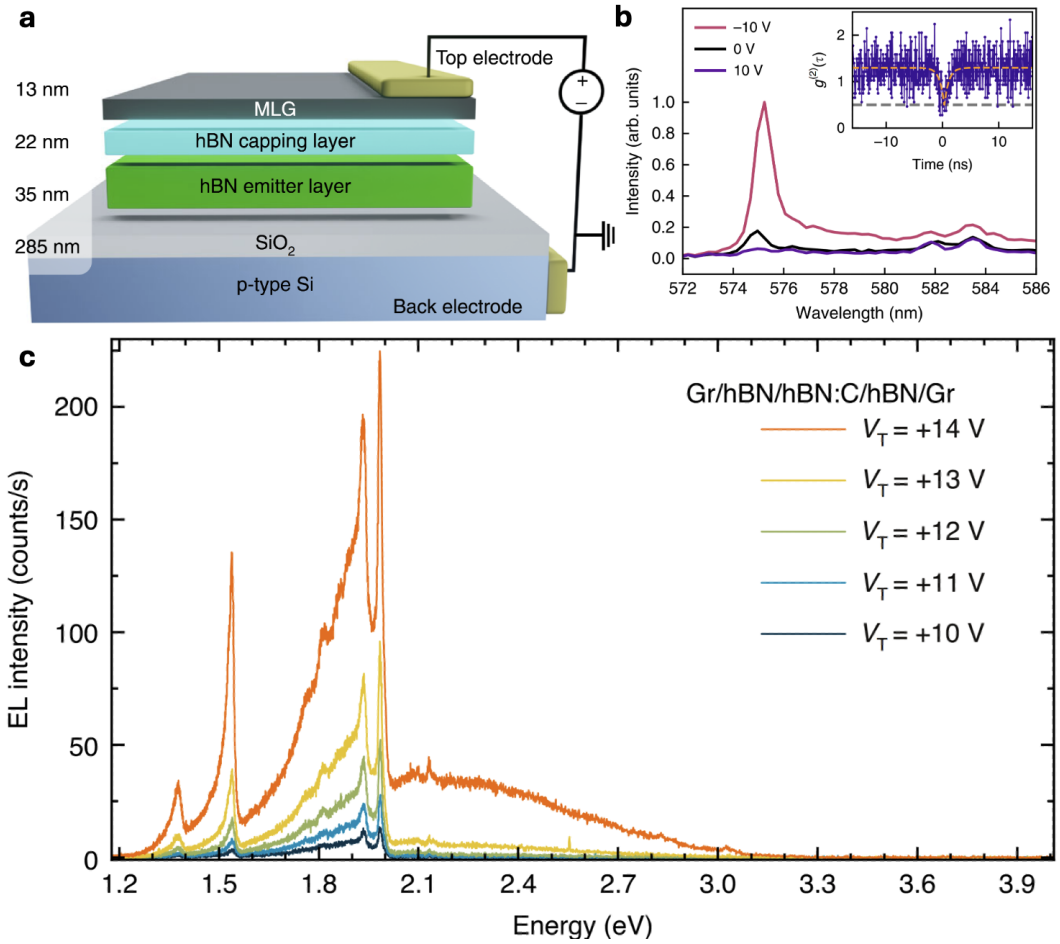


Figure 2.4: ***Literature examples for electrical control of hBN quantum emitters and electrical excitation of visible ensembles of hBN emitters.*** ***(a)*** *Illustration of a graphene-hBN gated devices for charge state manipulation of hBN quantum emitters.* ***(b)*** *Cryogenic PL spectra of hBN quantum emitter found in the device presented in (a) and showing bias dependent emission brightness. Inset shows antibunching of the studied emitter. Reproduced from reference [144].* ***(c)*** *Cryogenic EL spectra of ensembles found in carbon doped hBN flakes. Reproduced from reference [145].*

localised non-quantum nature, originating from large ensembles of defects. Chapter 5 of this thesis addresses this gap by demonstrating narrowband electrically driven emission covering the whole visible–NIR spectrum from hBN quantum emitters using vdW heterostructures. The chapter confirms quantum origin through antibunching in second-order correlation measurements. Additionally, fabricated devices operate at room temperature and still exhibit narrowband emission. Chapter 6 then further investigates robustness of these systems, demonstrating stable electrical excitation over prolonged operation times up to 36 hours, and explores electrical generation and control of emitters under high- and low-field conditions.

3

Materials & Methods

The purpose of this chapter is to provide detailed information on the fabrication and optical characterisations of electrical vdW devices. It will describe in detail the materials used, exfoliation and transfer techniques for stacking 2D layers, lithography and metal depositions, and confocal microscopy.

3.1 | Materials

The quality of materials used in vdW heterostructure fabrication plays a central role in determining the performance and stability of the resulting quantum optoelectronic devices. This section outlines the specific sources and properties of hBN and graphite crystals employed throughout this work.

3.1.1 | hBN and Graphitic Materials

High-quality hBN crystals used in this thesis were provided by the National Institute for Materials Science (NIMS), synthesised using high-pressure high-temperature growth methods. This process produces hBN with exceptional crystallinity, large lateral dimensions, and low impurity concentration [108]. These characteristics make NIMS-grown hBN ideal for fabricating vdW heterostructures, where hBN serves as a dielectric layer that both insulates underlying materials from substrate-induced charge noise and provides environmental isolation [106]. However, the high material quality also means that pristine NIMS hBN typically lacks native optically active quantum emitters. To address this, additional treatments are applied. Prior to exfoliation, high-temperature carbon doping can be carried out at NIMS to introduce luminescent centres [153]. Additionally, exfoliated flakes can be annealed under specific gaseous environments to activate emitters within the flake [131]. Alternatively, com-

mercially available lower-grade hBN (HQ Graphene) is more likely to host native emitters after in-house annealing and are thus more suitable when quantum emission is the primary objective.

Graphite crystals were sourced commercially (HQ Graphene). These high quality natural graphite crystals were used for exfoliation of monolayer and multilayer flakes that served as conductive channels, tunnel contacts, or local gates in vdW heterostructure devices. Throughout this thesis, the term **graphene refers to exfoliated flakes of monolayer graphene**, while **thicker flakes (few nanometres) are referred to as multilayer graphene**.

3.2 | Experimental Methods

Detailed fabrication steps, transfer procedures, and characterisation results are provided in the subsequent sections. General methods used for the integration of hBN single photon emitters into vdW heterostructures are discussed. In particular, exfoliation of hBN and graphene flakes, aligned transfer techniques for stacking, optical and electron beam lithographies, and metal deposition.

Characterisation of the fabricated devices was carried out both electrically through current-voltage measurements, and optically via confocal microscopy to probe the quantum emitters.

3.2.1 | Exfoliation

Mechanical exfoliation has become a widely adopted method for producing high-quality 2D materials. Original exfoliation conducted by K. Novoselov and A. Geim involved direct scotch tape exfoliation of small mesas of graphite [154]. Since then, the general approach method has remained.

Bulk crystals of material are first placed on a scotch tape. The crystal is then thinned down by exfoliating it onto several other scotch tapes. From that, when a thinned-down crystal of a vdW material is pressed on the substrate, it experiences adhesion to both the tape and the substrate. During peel-off process of the tape, adhesion between bottom flake layers and the substrate holds the flake down while adhesion of the tape sticks to the top layer of the flake. Upon exfoliation, the flake cleaves between its layers, thus separating the flake into two pieces, with bottom layers staying on the substrate and top layers remaining on the tape (Figure 3.1). As shown, exfoliation produces high-quality atomically clean vdW flakes since crystals are cleaved along the basal plane.

Challenges associated with mechanical exfoliation include the lack of control over the shape, size, and thickness of the resulting flakes, as well as their random distribution across

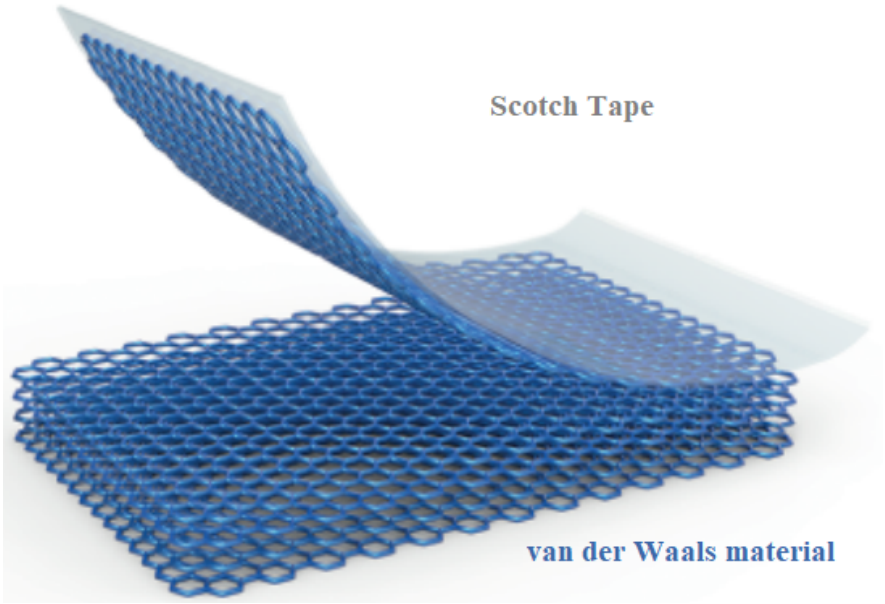


Figure 3.1: ***Schematic illustration of exfoliation principle.*** *Top layer of a vdW flake is peeling off with the tape, while bottom layers are left on the substrate. Reproduced from reference [155].*

the substrate. Since it is impossible to predict at which layer a crystal will cleave, achieving uniform or reproducible flake thickness is inherently difficult. This renders exfoliation a non-scalable technique, although recently there has been progress in automating this process with machine learning and robotics [156]. While commonly used 3M Scotch tape provides sufficient tackiness to isolate flakes with atomically clean interfaces, it often leaves adhesive residues around the exfoliated regions, necessitating additional cleaning steps. Additionally, due to differences in interlayer bonding strengths among various vdW materials, exact exfoliation techniques must be tailored to each material individually.

For exfoliating larger-area flakes, it is necessary to start with a large-area single crystal that is placed on a master tape and thinned using additional tapes. Due to uneven adhesion across the surface, crystals tends to fracture into smaller pieces during each thinning step. Therefore, exfoliated thin flakes of any material are generally laterally smaller. Thus, using larger crystals increases the likelihood of exfoliating thin flakes with larger lateral dimensions.

Exfoliation of hBN typically involves placing few crystals on master tape, compared to graphene, where a significantly larger crystal can be used by itself. Master tapes that contain the original crystal are typically duplicated several times and thinned down. For hBN, tape with a dense area of shiny crystals is desired. For graphene, large transparent crystals on the tape are ideal. To aid exfoliation yield, surface of target substrate can be made more reactive,

thus increasing its adhesion with exfoliated flakes. Common methods include pre-treating the substrates in plasma or UV-ozone environments, or annealing at 150-200 °C. The former approach is commonly used, since exfoliation yield is still high, while flake adhesion to substrates is weak enough for subsequent flake pickup used in device fabrication. Post exfoliation, majority of polymer residue from tape can be removed using hydrogen annealing via the hydrogenation process [157].

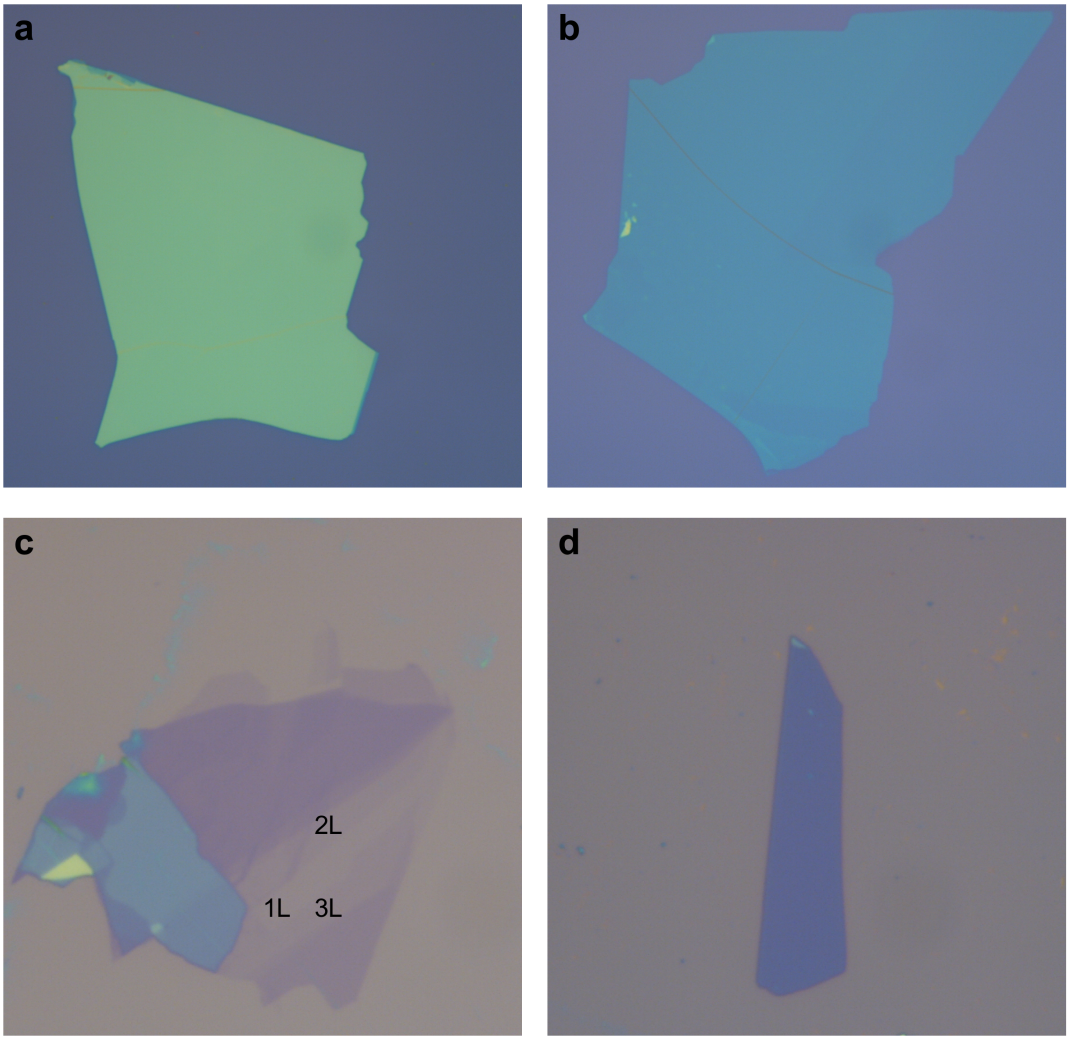


Figure 3.2: ***Optical microscope image of exfoliated hBN, graphene and graphite flakes.*** ***(a)*** *hBN flake of typical uniform thickness, suitable as quantum emitter host.* ***(b)*** *Thin hBN flake of typical thickness used as a capping layer in heterostructures.* ***(c)*** *Multilayer graphene flake showing monolayer (1L), bilayer (2L), and trilayer (3L) regions.* ***(d)*** *Graphite flake used as a conducting layer or contact material in device fabrication.*

Thickness of exfoliated flakes is typically identified via optical contrast using a white-light microscope. hBN exhibits a characteristic colour pattern due to thin-film interference, allowing for an approximate thickness estimation with nanometre-scale precision. Graphene appears nearly transparent in the monolayer and few-layer regimes, while thin graphite flakes (several nanometres thick) tend to display a consistent purple hue. Exact thickness can be confirmed using Raman measurement and atomic force microscopy. Figure 3.2 shows representative hBN and graphene flakes used in device fabrication. The hBN layer hosting quantum emitters typically ranges from 10 to 60 nm in thickness. Top and bottom flakes of hBN used as protective buffers for devices, also referred to as capping hBN, and are usually around 10 nm. They provide sufficient insulation from substrate doping and environmental effects, and serve as a flat smooth substrate instead of silica to avoid dangling bonds. Monolayer, bilayer, and trilayer graphene flakes offer excellent tunability, while few nanometre thick graphite exhibits high conductivity. By combining these, vdW quantum devices of almost unlimited configurations can be fabricated.

3.2.2 | hBN Emitter Generation

Generation of the three groups of hBN emitters explores different approaches, as discussed earlier in Chapter 2, however, initial flake preparations follow the same procedure. To begin, hBN flakes are mechanically exfoliated onto SiO_2/Si substrates with 285 nm oxide layers. The samples are then cleaned from residue following aforementioned annealing procedures. A consecutive cleaning step of 2-3 hours UV/ozone treatment removes any leftover carbon contamination. After this, the process depends on the group of emitters that will be generated. Given that the next chapter discusses optoelectronic devices for addressing B-centres, while the following two chapters explore novel methods of generation hBN emitters via electrical fields, B-centre generation method is briefly discussed here.

The flakes are annealed once more, this time for 1 hour at 1000 °C in a quartz tube furnace in the N2 atmosphere set to a flow rate of 50 sccm and ramp heating rate of 120 °C/min. The cool down to room temperature process is 3 hours. Flakes of desired thickness are then screened via cathodoluminescence to find the characteristic UV triplet emission that is indicative of hosting B-centres upon electron beam irradiation [119]. Finally, after spot mode irradiation to generate arrays of B-centres and prior to device fabrication, flakes are treated to 1 hour UV/ozone once more.

3.2.3 | Align Transfer

Aligned transfer is a laboratory technique specifically developed for working with vdW materials. It enables deterministic pick-up and placement of flakes exfoliated onto new target locations. The setup has optical imaging, similar to standard microscope, but incorporates an additional three-axis arm designed to hold a polymer stamp used for lifting flakes from their original substrates. The transparent nature of the polymer, combined with a cutout in the arm aligned with the microscope's optical axis, allows clear visualisation through the stamp. This makes it possible to align the polymer precisely with a target flake. After picking up the top flake, the operator can then see through it to align and pick up next flake, and so on, thus enabling construction of vdW heterostructures layer by layer. This method offers micrometer precision in the placement of individual flakes and allows for deterministic stacking of materials such as graphene and hBN with control over relative orientation and lateral alignment, both of which are critical for emitter placement and junction geometry.

The transfer process is performed using a custom-built align transfer setup, shown in Figure 3.3. A combination of lenses and a beamsplitter directs light from a white-light source to the sample plane. Multiple objectives can be used, depending on the required field of view and magnification. The sample rests on a micro-positioning rotating stage, with its vertical height controlled by a high-precision motorised z-stage (0.0001 mm resolution). An X-Y-Z micromanipulator is used to hold the arm that carries the polymer. The transparent polymer film, typically polyvinyl alcohol (PVA) or polypropylene carbonate (PPC), is drop-cast onto a dome-shaped polydimethylsiloxane (PDMS) stamp (a few millimetres in diameter and $\sim$1 mm in height) attached to a glass slide. This viscoelastic stamp is then used to pick up and sequentially stack exfoliated flakes.

For heterostructure assembly, a capping hBN layer is usually picked up first, as it not only protects the stack from environmental exposure but also adheres strongly to other layered materials via vdW forces [105], facilitating the subsequent pick-up of graphene, which otherwise does not adhere well to polymers. Flakes are aligned and brought into contact with the polymer at 40–60 °C. Once the full stack is assembled, it is released onto the target substrate by melting the polymer at elevated temperatures (110–125 °C).

To achieve clean and smooth interfaces between vdW flakes, the polymer stamp should be brought into contact gently, from a single edge and at a steep angle. This improves layer uniformity, minimises the chances of trapping air bubbles, and reduces interfacial strain. Precision over the approach angle can be achieved by incorporating additional two-axis tilt control of the stamp arm. By ensuring atomically flat contacts, quantum tunnelling is more uniform and quantum emitters within the stack experience consistent vertical coupling across the heterostructure. For increased reproducibility and minimised contamina-

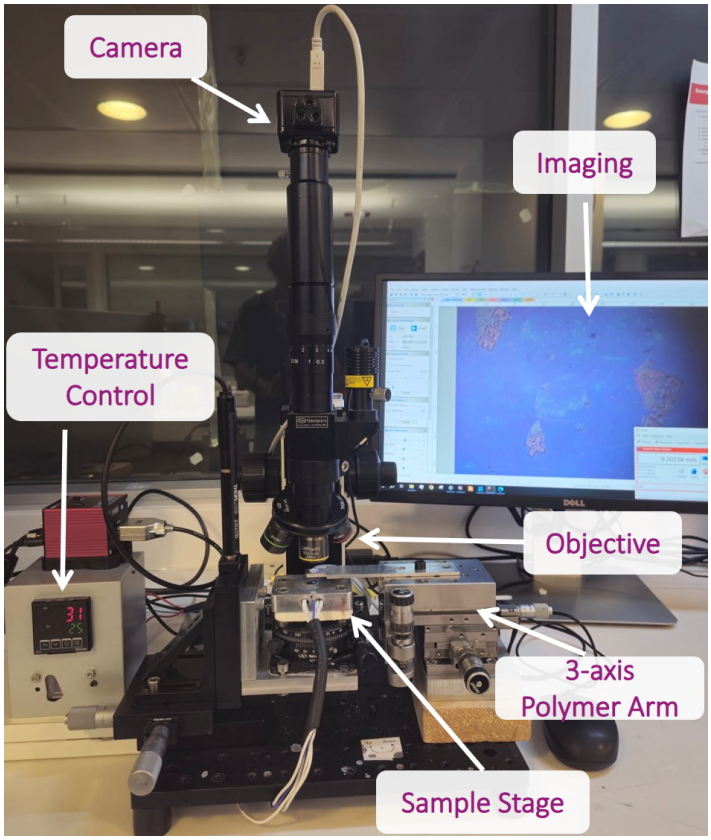


Figure 3.3: ***Annotated image of an align transfer setup.*** *Key components include a sample mounted on a three-axis stage, which is imaged using a camera through an optically aligned white-light illumination path and displayed on a desktop monitor. A temperature controller sets and monitors the sample stage temperature. A second three-axis stage is used to position and align the polymer arm for deterministic pickup and placement of vdW flakes.*

tion, entire transfer process could be carried out in a cleanroom environment. Particularly, air-sensitive materials may require a nitrogen glovebox.

3.2.4 | Lithography

Lithography was used to define metal contacts used for electrical connections to stacked heterostructures. Depending on purpose and resolution, two lithographic techniques were employed: standard UV photolithography for large-area patterning and electron beam lithography (EBL) for precise alignment to smaller features with sub-micrometre accuracy. Each method involves the same fundamental steps: coating substrate with a photosensitive resist, exposing selected regions to a radiation source, and developing the exposed areas in a chemical solution to define the desired pattern.

In UV photolithography, the substrate is coated with a positive-tone photoresist (AZ1518) that becomes soluble in developer upon UV exposure. UV light illuminates the sample from above, through the mask that contains electrode pattern. In the exposed regions, incident radiation induces a photochemical reaction that changes the molecular structure of resist, increasing its solubility in developer solution. Since this method relies on optical shadowing, the achievable resolution is limited by light diffraction and mask alignment accuracy, with a typical UV lithography resolution limit of 1 μm. After exposure, the sample is developed in AZ MIF 726 that selectively removes the exposed regions in the shape of the intended pattern. This technique is well suited for defining alignment markers, contact pads, and other features with dimensions in the micrometer range. Additionally, vdW flakes remain visible beneath the resist prior to exposure, allowing the exposed area to be aligned directly to a specific region of a flake or heterostructure stack.

For instances where a custom or high-precision pattern is required, EBL approach can be used. EBL is performed inside a scanning electron microscope (SEM), where a tightly focused electron beam is scanned over the sample surface, allowing for high-resolution imaging by detecting backscattered or secondary electrons. The same beam can be repurposed for lithography by selectively exposing a resist-coated sample. Unlike UV lithography, EBL does not require a physical mask; instead, patterns are digitally defined and written by controlling the beam deflection. A beam blanker is used to rapidly switch the beam on and off within each write field, enabling selective exposure of arbitrary shapes with nanometre precision. Commonly used resist is a positive-tone polymethyl methacrylate (PMMA) A5, which becomes more soluble in developer after electron exposure due to chain scission of its polymer backbone. Similar to UV lithography, the resist can be spin-coated over the heterostructure, however, the non-conductive nature of polymers prevents direct imaging of flakes in SEM. This necessitates the use of pre-fabricated metal alignment markers beneath the resist to perform accurate EBL on vdW flakes. Despite this constraint, high resolution and patterning flexibility of EBL make it ideal for defining small features over heterostructures or in confined geometries where conventional UV lithography is insufficient.

3.2.5 | Metal Deposition

Metal deposition onto lithographically patterned heterostructures was carried out using thermal evaporation. In this technique, both sample and deposition metal are loaded into a high-vacuum chamber, with the sample mounted face-down on a rotating stage at the top of the chamber, while the target metal is placed at the bottom in a resistive boat (typically made of tungsten). Bias is applied on the tungsten boat, thus flowing current which heats up the boat due to its high resistivity. At sufficiently high current levels, the boat reaches

temperatures sufficient to melt and evaporate the metal. Vaporised atoms travel upwards and condense onto the cooler surface of the sample, forming a uniform thin film. This process allows for smooth, low-energy deposition that minimises thermal damage to sensitive materials such as monolayer graphene, which can degrade or oxidise under elevated temperatures [158–160]. As a result, thermal evaporation is a preferred technique for metal deposition onto vdW materials.

Standard procedure involves deposition of a thin sticking chromium layer first, which has higher adhesion to silica compared to gold. A gold layer is then deposited on top to form low-resistance electrical contacts that remain stable under ambient conditions. Typical metal thicknesses are 5–10 nm for the adhesion layer and 40–90 nm for the gold layer. Prior to deposition, bare silica substrates are cleaned using a brief oxygen plasma treatment to remove resist residues and improve metal adhesion. The metal is evaporated using a thermal evaporator system operating at a base pressure below 1×10^{-7} mbar. After deposition, samples are immersed in acetone at 50 °C for eight hours for lift-off, dissolving the resist and removing unwanted metal on top of it. Acetone is cleaned with a gentle isopropanol rinse to assist the lift-off process without damaging the underlying flakes. Fabricated devices are then inspected under an optical microscope.

3.2.6 | Confocal Microscopy

Optical characteristics of hBN quantum emitters can be probed using PL spectroscopy, employing a standard widefield PL microscope. These systems consist of two optical paths, laser excitation and emission collection, aligned through a single microscope objective. A beamsplitter or dichroic mirror is used to separate the two paths, acting as a filter that reflects the excitation laser while transmitting the longer-wavelength emitted light. PL photons are directed to detectors such as spectrometers or high-sensitivity cameras. Typical objectives in such setups have moderate numerical apertures (e.g., NA = 0.6), allowing widefield imaging of the sample surface. However, this also results in the collection of fluorescence from a larger spatial area and out-of-focus regions. Since quantum emitters are atomic-scale, diffraction-limited photon sources, proper characterisation of individual emitters requires a confocal microscopy setup.

The term *confocal* refers to the configuration in which the focal plane of the excitation beam at the sample is optically conjugate to the focal plane of the detector in the collection path. Additionally, a confocal system achieves optical sectioning and improved resolution by placing a spatial pinhole in the image plane before the detector. This pinhole transmits only light originating from the focal volume, while rejecting out-of-focus background. Optimal pinhole diameter corresponds to one Airy unit, derived from the point spread func-

tion (PSF) of a microscope, and is defined by the size of the diffraction limited spot produced by the objective lens. The Airy disk diameter is given by:

$$d_{Airy} = 1.22 \cdot \frac{\lambda}{NA} \tag{3.1}$$

where λ is emission wavelength and NA is numerical aperture of the objective. High-NA objectives (typically NA $\geq$ 0.9) are used to minimise the Airy disk size, thereby maximising resolution, enhancing photon collection efficiency, and improving signal-to-background ratio, which are key factors in resolving and analysing single quantum emitters.

Since a confocal microscope uses two effective lenses, an objective for excitation and a collection lens before the pinhole, their magnification must be taken into account when evaluating microscope confocality. Because the Airy disk is formed at the sample plane while the pinhole is placed at the conjugate image plane, its projected size must be scaled by the system magnification, such that the projected Airy disk diameter becomes:

$$d_{proj} = 1.22 \cdot \frac{\lambda}{NA} \cdot (\frac{f_{lens}}{f_{obj}}) \tag{3.2}$$

To ensure optimal confocality, the physical pinhole placed at the image plane should closely match this projected Airy disk diameter. A pinhole that is too large allows more out-of-focus light, while one that is too small reduces signal throughput.

In fibre-based confocal systems, where PL collection light is coupled into a fibre, the pinhole is effectively replaced by either the core or the mode field diameter (MFD) of the collection fibre. For a multimode fibre, the core diameter determines the effective pinhole size, and Equation 3.2 still applies. In the case of a single-mode fibre, the MFD defines the effective pinhole. Confocality is then evaluated by comparing the MFD to the projected Airy disk size:

$$Confocality = \frac{MFD}{d_{proj}} \tag{3.3}$$

For single mode fibres, MFD is typically well-matched to the projected Airy disk, giving a confocality close to 1, which provides optimal spatial filtering. Multimode fibres, by contrast, have larger cores, leading to higher confocality values (e.g., 2–3), which increases signal collection at the cost of reduced background rejection. The choice between single-mode and multimode collection depends on the measurement type, signal strength, and noise tolerance.

Confocal microscopy becomes substantially more powerful with the addition of sample scanning capability. Having the excitation and collection spots focused to near the diffraction limit means that raster-scanning this small spot across the sample allows the construction of spatial emission maps capable of resolving multiple emitting systems across a large

area. There are two methods for achieving this. The first relies on a high-precision piezoelectric nanopositioner stage that physically moves the sample in front of the objective in the X-Y plane with nanometre resolution. This approach, while precise, is relatively slow and may exhibit hysteresis or drift, making it difficult to return to the exact same position repeatedly. The second method keeps the sample stationary and uses galvanometric or scanning mirrors to optically steer both the excitation and collection beams simultaneously. This configuration requires a pair of identical lenses positioned in a *4f* configuration between the scanning mirror and the objective. As shown in Figure 3.4, the lenses are spaced such that the first is one focal length from the scanning mirror, the second is one focal length from the back focal plane of the objective, and the two lenses are separated by *2f*. In this setup, angular deflections introduced by the scanning mirror are converted into lateral translations at the sample image plane, enabling distortion-free, diffraction limited scanning across the field of view. The same principle applies in the collection path, preserving spatial alignment with the detection pinhole or fibre and maintaining confocality throughout the scan.

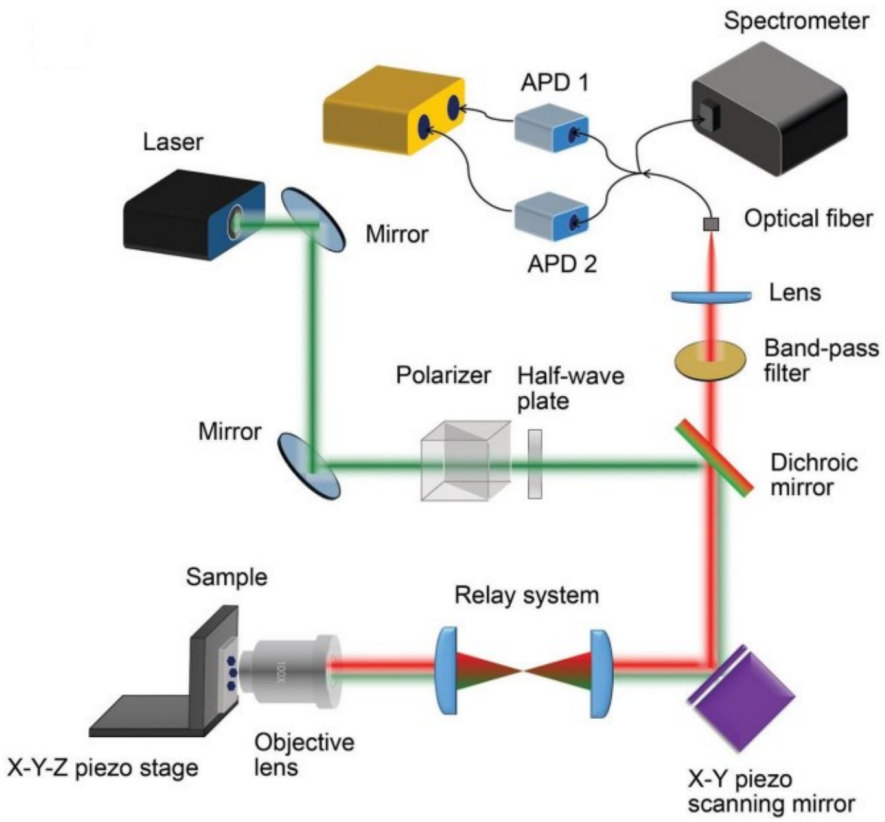


Figure 3.4: ***Schematic illustration of a scanning confocal microscope****. Optical paths and components of a scanning confocal microscope used to study quantum emitters. Relay system is the 4f dual lens configuration. Reproduced from reference [90].*

Layout demonstrating the complete excitation and collection optical paths is also shown in Figure 3.4, along with other key components of the system. The excitation path may include polarisation control elements, such as waveplates or polarisers, which are useful for optimising excitation coupling into quantum emitter systems. The collection path typically incorporates long-pass or band-pass filters to suppress background fluorescence or residual laser scatter before photons are directed to either fibre-coupled avalanche photodiode detector (APD) or a spectrometer. The former have high sensitivity and fast temporal response allowing for individual photon detection via generation of a measurable avalanche current from a single absorption event. APDs are thus commonly used for spatial emission mapping and second-order correlation experiments.

4

Electrical Control of hBN Quantum Emitters

This chapter investigates the integration of hBN B-centres into vdW-based electrical device heterostructures to study their response to externally applied electric fields via the Stark effect. Because hBN is a two-dimensional material, electric fields must be applied both out-of-plane and in-plane with respect to the defect. Consequently, two device architectures were fabricated, each designed to provide a field along one of these directions. photoluminescence excitation (PLE) spectroscopy was employed to resolve the ZPL shifts of the B-centre under applied electric fields. This work reports extremely low susceptibility to out-of-plane fields, while in-plane fields produced a well-defined quadratic Stark shift.

Results presented in this chapter were published in *Physical Review Applied* titled *"Stark Effect of Blue Quantum Emitters in Hexagonal Boron Nitride"* [161] and provide an insight into the structure of the B-centre as well as serve as a guideline for dynamic ZPL tuning for coupling B-centre to optical cavities or other emitters.

4.1 | Context

Quantum emitters in hBN are recognised for their brightness and robustness with regard to high temperature and harsh environments [90, 135, 162–166]. Most recently, optical access to spin properties for some of these defects was demonstrated at room temperature [9, 125, 167–169]. Moreover, the vdW structure of the host crystals provides compelling opportunities for the development of quantum technologies based on quantum emitters in hBN [170, 171]. However, broad adoption of hBN quantum emitters in integrated quantum photonics has been limited by inhomogeneous broadening of the emission lines.

The dominant cause of inhomogeneous broadening is fluctuating electric fields resulting from charge transitions in the vicinity of quantum emitters. The fields interact with the electric dipoles of the defects and give rise to spectral diffusion. The effect has been studied extensively in various solid state systems, such as NV centres in diamond [172], point defects in silicon carbide, and rare earth doped crystals [173]. In the case of hBN, this interaction is very strong for some emitters, and has been used to realise massive Stark shifts through the use of applied electric fields [142, 143, 174]. As a result, defects with inversion symmetry have been explicitly excluded during theory calculations when searching for possible candidates of quantum emitters in hBN.

To this end, some work has focused on eliminating spectral diffusion by surface passivation and by optical repumping [175, 176]. A lifetime limited linewidth was achieved for a defect in hBN by charge manipulation or depletion using heterostructure devices [140]. An alternative approach to overcome spectral diffusion is to identify point defects with small or ideally zero permanent electric dipole moments, such as the SiV centre in silicon carbide or centrosymmetric defects such as group IV defects in diamond [177, 178]. The absence of a permanent electric dipole moment in these defects results in reduced sensitivity to electric fields and small inhomogeneous linewidth broadening.

Recently, the B-centre in hBN was identified as being spectrally stable with a narrow emission centred at 436 nm [118, 179]. These defects can be created deterministically using electron beam irradiation and have been associated with the presence of UV emission at 4.1 eV [119]. Interestingly, the B-centres exhibit stable single photon emission at cryogenic temperatures with spectral diffusion that is negligible compared with that of other quantum emitters studied to date in hBN [121]. Sub-gigahertz linewidths have been measured in this group of quantum emitters in the absence of applied electric fields or post processing treatments.

This work investigates the Stark shift of B-centre quantum emitters in hBN. Coherent excitation to measure the Stark shift upon applying in-plane and out-of-plane electric fields is used to characterise the electric dipole interaction for B-centres. Building on these results, a discussion on implications for defect symmetry and density functional theory are used to identify the likely defect structure. These results constitute an important step toward identifying spectrally stable quantum emitters in hBN and are particularly valuable for creating site specific quantum emitters that are resonant with optical cavities or with other quantum emitters.

4.2 | Results

B-centres are created by exposing mechanically exfoliated hBN flakes to a focused electron beam using a commercial scanning electron microscope. Single B-centres are identified using an autocorrelation measurement as shown in Figure 4.1b. While the emission energy of single photon emitters in hBN spans a broad spectral range, from the UV region to the NIR region, the ZPL of B-centres is centred consistently at 436 nm as in Figure 4.1c, varying by less than 1 nm [118, 121]. To measure the linewidth of these emitters, the sample is cooled to 5 K. By scanning the ZPL with a narrow continuous-wave laser, the full width at half maximum (FWHM) of this particular B-centre is found to be 1.91 GHz. In this resonant PLE measurement, the wavelength of a narrow excitation laser is tuned across the ZPL transition while recording the phonon sideband emission intensity. As the laser becomes resonant with the optical transition, an increase in PL signal is observed, producing a resonance peak as a function of excitation frequency. The linewidth is extracted by fitting this resonance profile, with repeated scans averaged to account for spectral diffusion and temporal fluctuations of the emitter. The resonant PLE scan shown in Figure 4.1d is the average of ten individual scans over the ZPL to account for temporal fluctuations of the emission. The best peak fit is Gaussian, indicative of inhomogeneous broadening caused by spectral diffusion.

Note that the range of spectral diffusion observed in PLE measurements differs between emitters, but is insufficient to be observed in PL spectra acquired with a spectral resolution of 130 GHz. This degree of inhomogeneous broadening is small compared with that of other emitters studied previously in hBN, indicating an inherent insensitivity of the B-centres to environmental effects such as electric field fluctuations in the hBN lattice.

To characterise the interaction of B-centres with an external electric field, Stark shift of the B-centre ZPL was measured. A detailed description of physical and mathematical interpretation of the Stark effect is provided in appendix A.1. Here, the Stark shift ΔE has a first order dependence on the electric field F characterised by $\Delta\mu_{perm}$, the difference in permanent dipole moments between the ground and excited states, and a second order dependence characterised by $\Delta\alpha$, the difference between the polarisabilities of the ground and excited states. This relation has the form [178, 180]

$$\Delta E = -\Delta\mu_{perm}F - \frac{1}{2}\Delta\alpha F^2 \tag{4.1}$$

Here, higher order Stark shifts related to hyperpolarisabilities are not considered as their contribution is negligible. A nonlinear electric field dependence is observed when the linear term vanishes, either due to the vanishing permanent dipole moment in both the ground

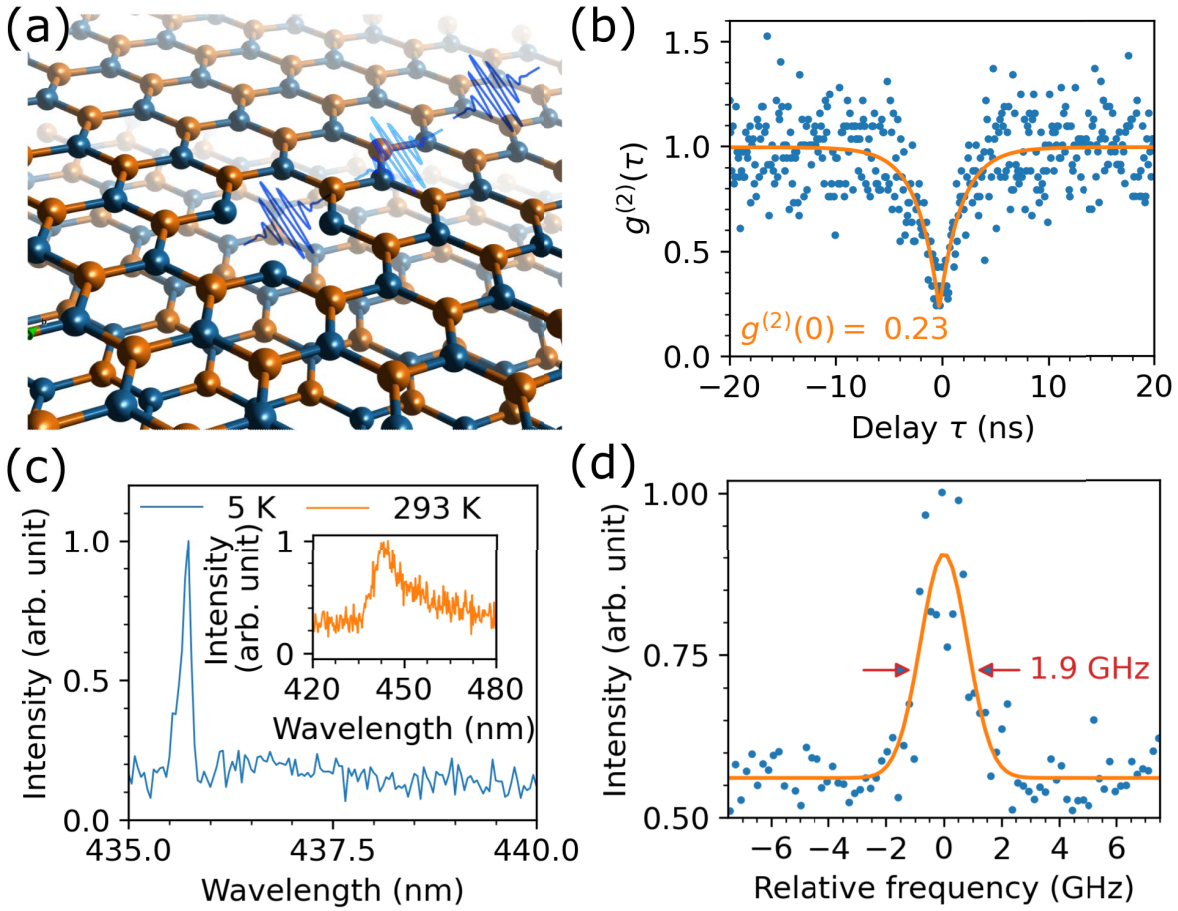


Figure 4.1: ***Characteristic B-centre quantum emission.*** ***(a)*** *Schematic illustration of hBN crystal lattice with an emitter.* ***(b)*** *Room temperature autocorrelation measurement of a single B-centre in hBN emitting photons at 436 nm wavelength. The solid line is a fit to the data.* ***(c)*** *Cryogenic PL spectrum of the same B-centre.* ***(d)*** *Resonant excitation of the B-centre, with a Gaussian fit yielding a linewidth of 1.91 GHz.*

state and the excited state or due to the perfect cancellation of the permanent dipoles of the ground and excited states. The latter is less frequent and appears only in special cases [181].

Two devices were engineered to apply in-plane and out-of-plane fields to B-centres. First, vertical device (which produces an out-of-plane electric field) was fabricated by transferring a 36 nm hBN flake containing B-centres over gold electrodes, as shown in Figrue 4.2a. An optical image of the fabricated vertical device is shown in Figure 4.2b. The hBN flake containing B-centres is highlighted with a blue line around its periphery. As a top contact, multilayer graphene (MLG) was used because of its semitransparency, although a capping hBN layer was also introduced on top to protect MLG from oxidation. The MLG and capping hBN layers are indicated by black and yellow lines, respectively. The device was loaded

into a cryostat, and the measured leakage current was limited to a few tens of nanoamperes at biases from -15 V to 15 V applied to the electrodes as shown in Figure 4.2c.

The emission polarisation of the candidate B-centre is measured to determine that the emission dipole is aligned in-plane, and hence that the vertical structure was applying an electric field perpendicular to the transition dipole. The inset in Figure 4.2d shows a strong linear polarisation visibility of 0.83, indicating the transition dipole is predominantly in-plane.

When applying the out-of-plane electric field to the emitter, a small linear Stark shift as observed is shown in Figure 4.2d. Strength of the externally applied field $F_{\text{mac}} = V_g/d$ does not directly correspond to the microscopic field experienced by the defect due to dielectric screening and local polarisation effects within the hBN lattice. To account for this, the local electric field at the emitter site is estimated using the Lorentz local field approximation [142]:

$$F = (\epsilon_{hBN} + 2)\frac{V_g}{3d} \tag{4.2}$$

where $\epsilon_{hBN} = 3.76$ is the out-of-plane dielectric constant [182], V_g is the applied potential field, and $d = 36$ nm is the electrode gap, equal to the thickness of the hBN flake containing the B-centre. A relatively large electric field is required to produce the observed ZPL shift. A linear fit yields a sensitivity of 0.01 GHz per MV.m^{-1}, or 2 mD, indicating that the permanent dipole moment between ground and excited states is either very small or oriented predominantly within the plane of the hBN lattice, and hence perpendicular to the electric field. Similarly, the lack of an obvious quadratic dependence suggests that the system has a low transition polarisability in the out-of-plane direction. The emission linewidth is approximately constant (Figure 4.2e), and does not change systematically with applied electric field, confirming that heating caused by the leakage current is negligible. Note that for this particular B-centre, emission intensity gradually decreases with increasing negative bias, until PLE emission is no longer observable, which occurs below -200 MV.m^{-1}. Similar behaviour has been observed in other quantum emitters in hBN and was attributed to charge transfer caused by tuning of the Fermi level [144, 146].

Next, lateral device was fabricated for application of in-plane electric fields, as shown in Figure 4.3a and Figure 4.3b. hBN flake with thickness of approximately 100 nm is transferred onto an interdigitated gold electrode pattern. The local electric field is assumed to be predominantly in the plane for emitters positioned equidistant between two neighbouring electrodes, so the field strength at the emitter is taken to be equal to the maximum field strength given by the electrode geometry. As with the vertical device, here the local applied electric field is approximated by Equation 4.2, although it is now appropriate to use the in plane dielectric constant $\epsilon_{hBN} = 6.93$ [182], while $d = 2$ μm is given by the separation of the

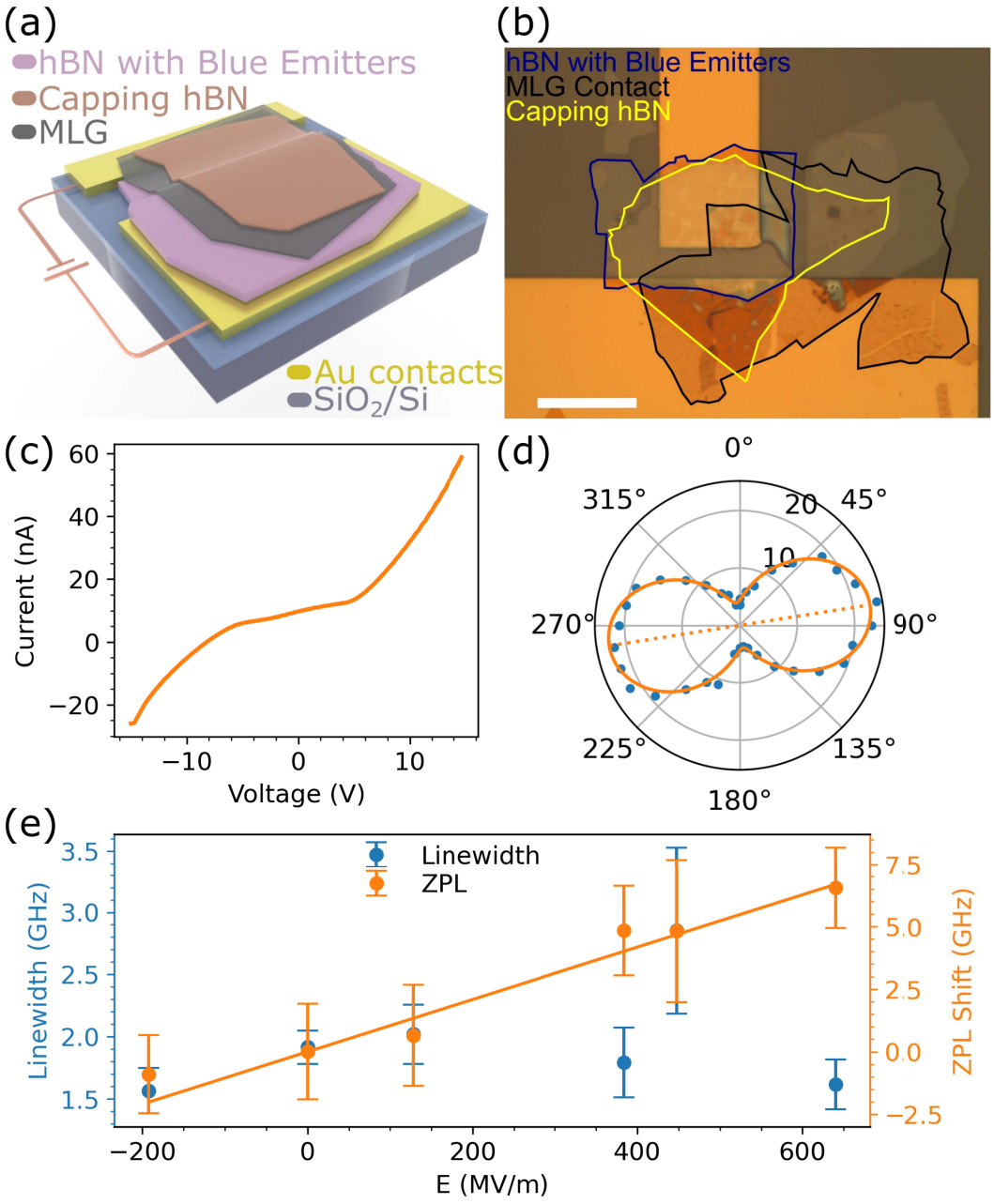


Figure 4.2: ***Vertical structure for investigation of the out-of-plane Stark effect.*** ***(a)*** *Schematic of the structure with hBN between the bottom gold electrode and a top MLG electrode.* ***(b)*** *Microscope image of the vertical device. Scale bar 20 µm. Coloured outlines show the edges of each layer.* ***(c)*** *Current-voltage characteristic measured at 5 K.* ***(d)*** *Emission polarisation of the examined emitter, with a polarisation visibility of 0.83.* ***(e)*** *PLE linewidth under applied electric field and shift of ZPL where a linear fit yields a gradient of 0.01 GHz per MV.m^{-1}.*

electrodes. Figure 4.3b shows an optical image of the hBN flake overlaying the gold electrodes. The hBN flake is then irradiated by an electron beam to generate B-centres in the gap between the electrodes. PL characterisation of the emitter is performed after confirming that the lateral device does not show any detectable leakage current, as shown in Figure 4.3c.

In contrast to out-of-plane electric field, the lateral device produces a clear quadratic shift of the emitter ZPL, as shown in Figure 4.3d. The shift magnitude per unit electric field strength is more than 200 times greater than the corresponding shift in the vertical device which implemented the in-plane electric field. Measurement of the emission polarisation, presented in the inset in Figure 4.3d, shows that for this particular emitter, the light is linearly polarised at an angle of 18° with respect to the direction of the local applied electric field. Assuming that the optical transition dipole moment is aligned parallel to the polarisation of the emitted light [178], projection of the optical transition can be estimated relative to the applied electric field. Using Equation 4.1 to fit the ZPL data in Figure 4.3d, obtain $\Delta\mu = 0.10$ D for the difference in permanent dipole moments between the ground and excited states, and $\Delta\alpha = 1078$ Å^3 for the corresponding difference in polarisability along the local field direction. A positive transition polarisability indicates that the excited state has greater polarisability than the ground state [180]. These results suggest that the B-centre has a relatively small permanent transition dipole moment, and a large transition polarisability, relative to visible emitters studied previously in hBN [142, 143, 174]. No correlation is observed between the applied electric field and the B-centre linewidth or maximum intensity.

In the same lateral structure, a second emitter was found to also display quadratic ZPL dependence in response to the applied electric field, though smaller in magnitude. Results for both emitters found in the lateral structure are compared, in Figure 4.4, with two published Stark shift values for the change in permanent dipole moment and the change in polarisabilities of longer wavelength quantum emitters in hBN. Noh *et al*. [142] reported values of -0.22 D and 149 Å^3 for the transition dipole moment and the polarisability, respectively. Nikolay *et al*. [143] obtained values of around 2.1 D and 770 Å^3 for the transition dipole moment and the polarisability, respectively. The values of $\Delta\mu_{perm}$ obtained in this study lie between those described in the literature, around the 0 D mark. The polarisability values are also comparable in magnitude to those reported in the literature, although a negative value is obtained for the second emitter, likely due to both strain [178] and the orientation of the applied field [180, 183]. This further suggests that the Stark response of the B-centre is dominated by the polarisability term, while the contribution from the difference in permanent dipole moments is comparatively small.

Using these results, geometry and composition of the defect can be proposed. Point group symmetry determines whether a permanent electric dipole moment can exist. In particular, the presence of inversion symmetry (as in D_{3d}) enforces a zero permanent dipole

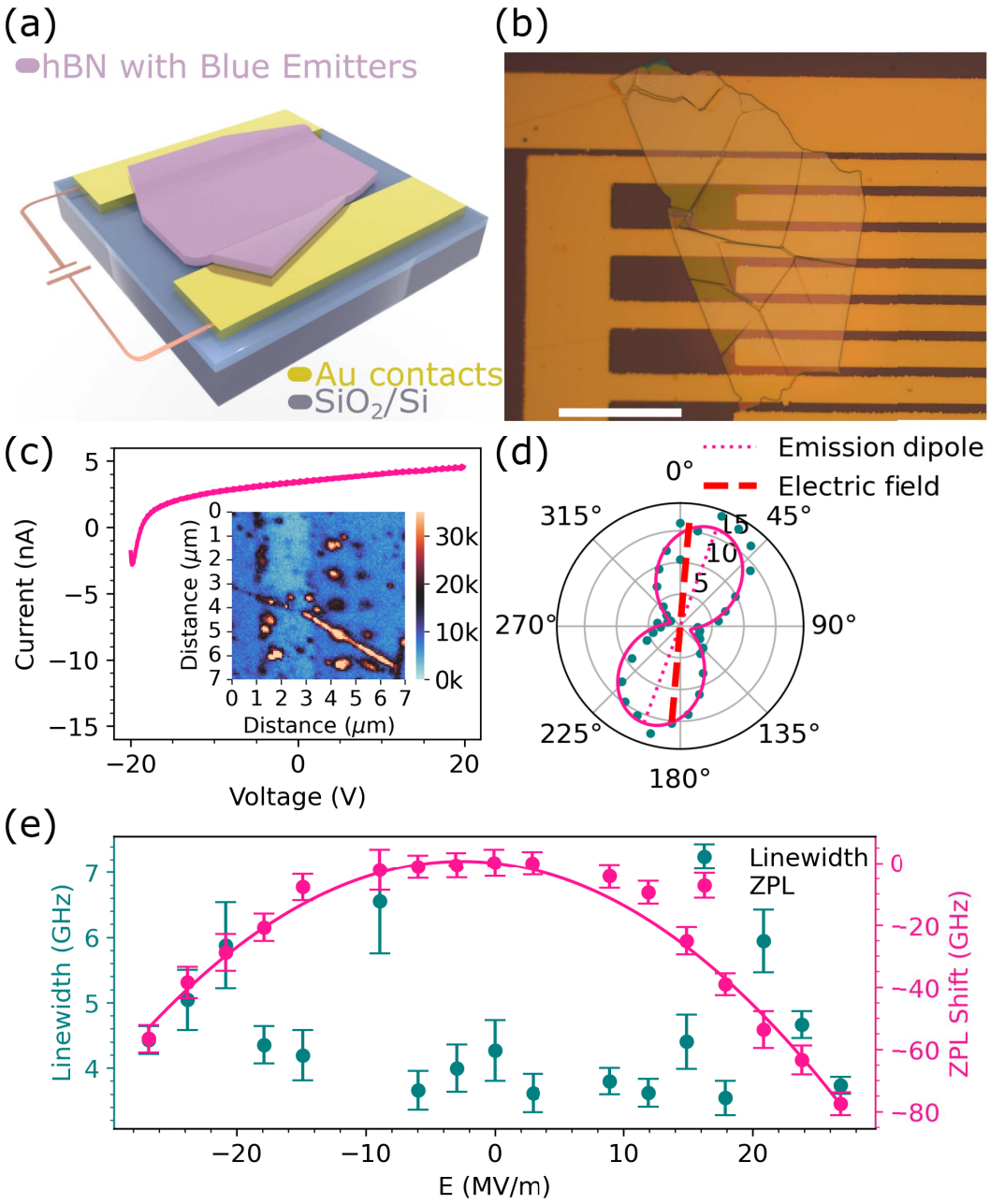


Figure 4.3: ***Lateral structure for investigation of in-plane Stark effect.*** ***(a)*** *Schematic of a lateral structure with hBN between two gold electrodes.* ***(b)*** *Microscope image of the lateral device. Scale bar 50 µm. An hBN flake is positioned on top of interdigitated gold electrodes, with gap separations of 2 µm.* ***(c)*** *Current-voltage characteristic measured at 5 K. Inset: Confocal map scan.* ***(d)*** *Emission polarisation of the examined emitter, with a polarisation visibility of 0.77. The electric field is closely aligned with the emission dipole.* ***(e)*** *PLE linewidth and shift of ZPL under applied electric field. A quadratic with linear component model (Equation 4.1) is used to fit the raw data, yielding* $\Delta\mu = 0.10\ D$ *and* $\Delta\alpha = 1078\ Å^3$.

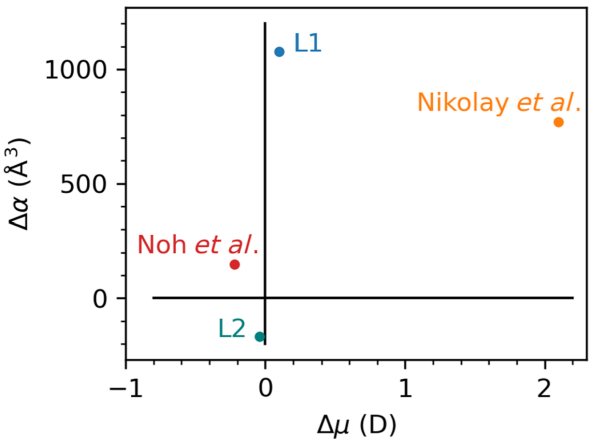


Figure 4.4: ***Comparison of components of the transition dipole moment for emitters in hBN.*** *Values at L1 correspond to the first B-centre examined in the lateral device. Values at L2 correspond to the second emitter in the same device. The other values are taken from Noh et al. [142] and Nikolay et al. [143].*

moment, as any dipole would be reversed under inversion and must therefore vanish. In the case of D_{3h} symmetry, although inversion symmetry is absent, combination of threefold rotational symmetry and horizontal mirror symmetry constrains the charge distribution such that any in-plane or out-of-plane dipole components cancel. As a result, defects with D_{3h} symmetry can also exhibit a vanishing permanent dipole moment.

The absence of a permanent dipole can be a consequence of defect symmetry. Indeed, group IV vacancy complexes in diamond may possess D_{3d} symmetry, where the inversion symmetry element of the group ensures a vanishing permanent dipole for these defects. The nonlinear Stark effect was recently reported for several such complexes in diamond [178]. The D_{3d} point group symmetry of hBN does not contain inversion symmetry. However, the combination of the threefold rotation symmetry and the in-plane reflection symmetry may also forbid the presence of a permanent dipole. With the use of symmetry arguments, the defect that exhibits a nonlinear Stark effect due to the absence of a permanent dipole must have D_{3h} point group symmetry in both the ground state and the excited state.

The observation of a nonlinear Stark shift helps us to narrow down the possible point defect configurations that may give rise to the B-centre quantum emission in hBN. The simplest configurations that have D_{3h} symmetry are in-plane single site defects, such as antisites, substitutional impurities, and vacancies. Boron and nitrogen vacancies are well known in the literature [184, 185], but according to the current understanding of these defects, they are not related to the B-centre in hBN. Furthermore, exclude both antisite and carbon interstitial defects. These defects form strong sp^2 hybrid bonding states with the neighbouring atoms, within the valence band of hBN. The defect states that appear in the

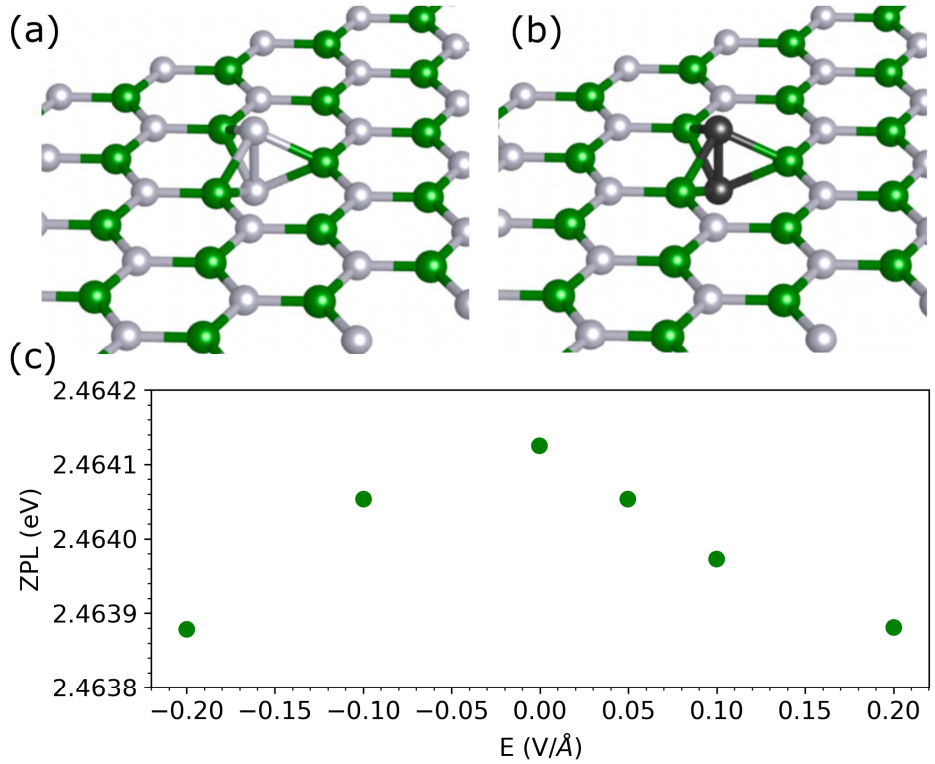


Figure 4.5: ***Density functional theory modelling.*** ***(a)*** *Schematic representation of the nitrogen split interstitial defect.* ***(b)*** *Schematic representation of the C_N^2 defect.* ***(c)*** *The electric field dependence of the ZPL energy of the nitrogen split interstitial defect as obtained from first principles calculations.*

band gap for these defects are related to the p_z state of the antisite or the substitutional carbon. Because of the lack of other defect states in the band gap, the possible optical transitions involve excitations from the valence band to the conduction band of the host.

For more complex defects, the symmetry requirements are fairly restrictive. In-plane two site defects can be ruled out due to the lack of threefold rotation symmetry. Consequently, the C_BC_N defect (associated with the 4.1 eV emission) and related defects can also be ruled out.

Next, consider interstitial defects. The most favourable configuration of the nitrogen interstitial is a split interstitial configuration [184], where two out-of-plane nitrogen atoms sit at a nitrogen site, as depicted schematically in Figure 4.5a. The negative charge state of the defect retains its D_{3h} symmetry in the first optical excited state and possesses no permanent dipole in the ground and excited states. In Figure 4.5c, the ZPL energy is calculated at the Perdew-Burke-Ernzerhof level of density functional theory. It depends nonlinearly on the electric field, which is in qualitative agreement with conducted measurements [186–188]. Note, however, that the B-centres are generated by electron irradiation of hBN flakes

characterised by the 4.1 eV emission that is associated with carbon [119]. Therefore, consider a related atomic structure obtained by replacing the two nitrogen atoms with two carbon atoms as shown in Figure 4.5b. This configuration is referred to as C_N^2. Interestingly, this configuration adopts D_{3d} symmetry, exhibits similar properties of a nitrogen split interstitial defect, and can be obtained from C_BC_N by the addition of a boron interstitial as

$$C_BC_N + B_i \rightarrow C_N^2 + 2.0 \text{ eV}. \tag{4.3}$$

Alternatively, dissociation of the 4.1 eV emitter due to the electron irradiation as previously suggested [119, 121] may lead to interstitial carbon atoms, which could recombine with a carbon substitutional defect and form the C_N^2 complex as

$$C_N + C_i \rightarrow C_N^2 + 2.8 \text{ eV}. \tag{4.4}$$

The positive energy gain of the reconstruction of the defects ensures the stability of C_N^2 in both processes. Furthermore, since interstitial boron and carbon atoms are both mobile at room temperature [184], the formation of the C_N^2 defect may happen without any annealing step and may happen solely due to electron irradiation.

4.3 | Summary

In conclusion, the emission tunability of B-centre quantum emitters in hBN is investigated through the use of two separate devices used to generate in-plane and out-of-plane electric fields. The transition energy is influenced by out-of-plane fields, but the magnitude of the observed linear Stark shift is small relative to the linewidth. In contrast, in-plane electric fields produce significantly greater ZPL modulation, yielding a clear quadratic Stark shift response. Using these results, this chapter provides insight into the possible atomic structure of defects responsible for the reported B-centres in hBN. Results suggest that the electric field response of the defect is predominantly within the plane of the hBN lattice, which may lead to decreased sensitivity to local field fluctuations that cause spectral diffusion.

5

Electrical Excitation of hBN Quantum Emitters

Advancing fabrication methods from previous chapter, here, multi-slot graphene–hBN devices are engineered specifically to enable application of very high electric fields that promote quantum tunnelling of both types of charge carriers into hBN layer hosting emitters. It is shown that upon simultaneous injection of electrons and holes, strong EL is observed from hBN colour centres. The emission is localised, polarised, is of quantum nature, displays a spectral profile that closely matches optically excited hBN quantum emitters, and remains stable even at room temperature.

Results presented in this chapter were published in *Nano Letters* under the title *"Narrowband Electroluminescence from Colour Centres in Hexagonal Boron Nitride"* [189], representing a key milestone in hBN emitter research as the first demonstration of non-classical EL from hBN colour centres and room temperature operation.

5.1 | Context

Colour centres in wide bandgap materials such as diamond or silicon carbide offer a unique opportunity to realise scalable quantum photonic circuitry [3, 12, 67, 72]. The colour centres, commonly referred to as "artificial atoms" or defects, can often be engineered on demand and exhibit narrowband (∼few nm) emission, even at room temperature. In most cases, the defects possess a ground and an excited state deep within the bandgap of the host crystal, which prohibits charge carrier thermalisation and hence enables room temperature operation. Luminescence from the defects is commonly induced by using optical excitation. However, for many applications, specifically for on-chip quantum devices and scalable quantum circuitry, electrical excitation of emitters is highly sought after [12, 72, 190, 191].

Electrical excitation of quantum dots [192, 193], molecules [194, 195], or carbon nanotubes [196] has been thoroughly investigated but is limited mostly to cryogenic temperatures. The EL from these systems relies on electron and hole injection using standard p-n or p-i-n junction geometries. On the other hand, EL from solid state defects in wide bandgap semiconductors is in its infancy, due to the challenges in efficiently doping these materials and achieving appropriate charge injection. So far, only a few platforms have been explored in the context of EL, limited to defects in diamond [197, 198] and silicon carbide [199], while also relying on p-i-n mechanism. Furthermore, even in these systems, on demand fabrication of optically active defects within a nanoscale vertical or lateral electrical junction integrated with a photonic resonator has remained elusive. To this end, vdW materials offer a fascinating opportunity to design a new generation of nanoscale quantum circuitry with electrically driven light sources [200–202]. hBN – the only wide bandgap vdW crystal – exhibits a unique feature in its ability to host a variety of optically active defects [107, 115]. Preliminary EL studies from hBN have been attempted; however, the emission was mostly confined to the near band edge (>5.5 eV) at the ultraviolet spectral range [151]. Critically, these band-to-band or band-to-defect recombination pathways typically result in a spectrally broad emission, which is not ideal for quantum applications. In this context, EL from narrowband defects at the visible and near-infrared spectral range would be highly desired for scalable quantum applications. Furthermore, most existing attempts to generate EL from hBN defects, were limited to cryogenic temperatures [145], which hinders practical room temperature operation, often needed for quantum sensing applications.

This chapter addresses this long-standing goal and realises vdW heterostructure devices that exhibit EL from hBN across the visible and the NIR spectral ranges. Employing vertical tunnel junctions of graphene-hBN-graphene, efficient electrical excitation of deep defects in hBN is achieved, with a persistent EL up to room temperature. Remarkably, localised emission that is fully polarised and stable over hours of operation was observed, making the emitters suitable for practical applications. The second order correlation measurement verifies the nature of these defects and confirms their quantised light emission. This work marks a turning point for the future employment of hBN and vdW heterostructures in on-chip, integrated quantum technologies [3, 67, 72, 190].

5.2 | Results

Figure 5.1a schematically illustrates device structure in which monolayer graphene, hBN, and monolayer graphene are vertically stacked to form a tunnel junction. Figure 5.1b shows an optical microscope image of a representative device. For an emissive layer, hBN crystals

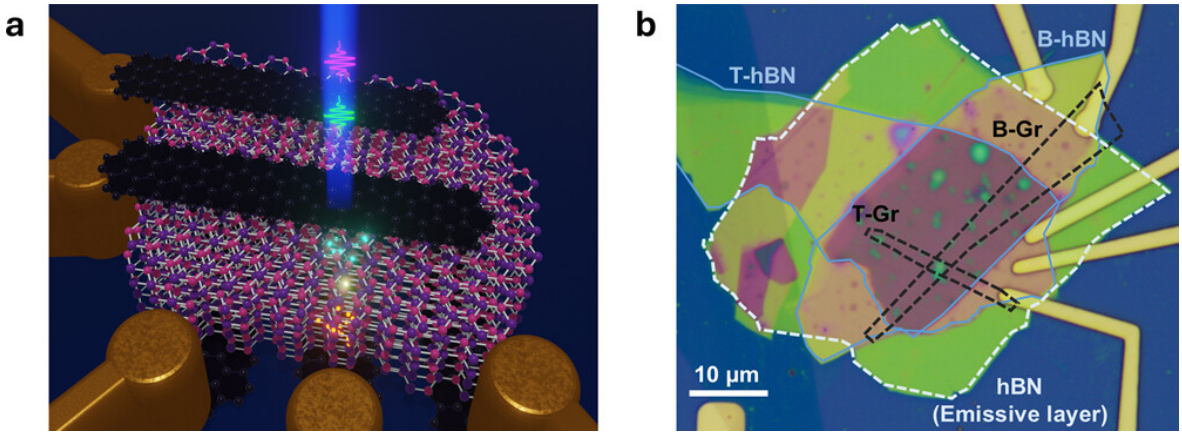


Figure 5.1: ***EL device to trigger hBN emitters in a vdW heterostructure.*** ***(a)*** *Schematic illustration of the vdW device. An emissive layer of hBN is stacked between the top and bottom graphene electrodes.* ***(b)*** *Optical microscope image of a heterostructure device. The hBN emissive layer is highlighted with a white dashed line. Top (T-Gr) and bottom (B-Gr) graphene electrodes are marked with black dashed lines. Blue lines indicate top (T-hBN) and bottom hBN (B-hBN).*

(white dashed line labelled as emissive layer) with thicknesses over 20 nm were used to prevent direct tunnelling between graphene electrodes. Black dashed lines indicate top and bottom graphene electrodes (labelled as T-Gr and B-Gr, respectively). The heterostructure is encapsulated with additional hBN layers, at the top (T-hBN) and bottom (B-hBN).

To begin, EL from defects at cryogenic temperatures (10 K) was first measured. Application of bias voltage resulted in prominent EL from hBN emitters with ZPL transitions centred at 490 and 801 nm, respectively, as shown in Figure 5.2(a, b). The intensity of the EL increases with an increased tunnelling current. Importantly, however, both spectra reach saturation as clearly shown in Figure 5.2c. Unlike traditional excitonic or bandgap emission from delocalised states, EL from individual defects is expected to saturate, as observed in the results. For the two different defects shown here, the saturation current varies, from under 1 to a few μA, depending on the immediate local electrostatic environment. Additionally, EL was measured from colour centres emitting at 4.1 eV, which form large ensembles in hBN crystals (Figure 5.3). In contrast to the previous saturation behaviour from few isolated emitters with ZPL at 490 and 801 nm, high-density defect clusters show a linear increase in EL intensity as a function of injection current. This provides evidence that the intensity saturation in Figure 5.2c is due to the limited number of defect sites.

To investigate the electrical excitation mechanism, current-voltage (I-V) characteristics of devices (Figure 5.2d) at a temperature of 10 K were recorded. Due to the ultrawide bandgap of hBN ($\sim$6 eV), the Fermi level in graphene and band edges of pristine hBN exhibit large energy barriers which mostly do not allow carrier injection under low electric fields [203]. It

was found that the devices in this work show a drastic increase of current from an applied voltage of ∼12.3 V eventually exceeding 1 μA (orange solid line in Figure 5.2d). Concurrently, voltage-EL intensity (V-L) characteristics (magenta circles in Figure 5.2d, corresponding to the 490 nm defect shown in Figure 5.2a) show that EL intensity increases exponentially from a voltage of ∼18 V.

Field emission model can be used to analyse electrical characteristics of the graphene-hBN-graphene heterostructures as schematically described in Figure 5.2f. The band diagram uses monolayer graphene electrodes, for which the linear dispersion and bias-dependent Fermi level shift are appropriate. For the case of high-quality hBN with low impurity density, previous studies [203, 204] show that the current is dominated by Fowler-Nordheim tunnelling of holes at the interface of graphene and hBN (blue arrow in Figure 5.2f). The tunnelling current satisfies the following equation where $\ln(I/V^2)$ and $1/V$ hold a characteristic linear relationship [205]:

$$\ln\left(\frac{I}{V^2}\right) = \ln\left(\frac{A_{\text{eff}} q^3 m}{8\pi h \Phi_B m^* d^2}\right) - \frac{8\pi\sqrt{2m^*}\Phi_B^{3/2} d}{3hq} \cdot \frac{1}{V} \tag{5.1}$$

V and d represent the bias voltage and insulator thickness, respectively. A_{eff} is the effective tunnelling area; q is the elementary charge; h is the Planck's constant; m is the free electron mass; m^* is the effective mass of the charge carriers in the insulator; and Φ_B is the tunnelling barrier height for charge carriers at the electrode-insulator interface. Tunnelling current in the fabricated device (orange solid line in Figure 5.2e) shows excellent linearity between $ln(I/V^2)$ and $1/V$ under high bias voltage. The slope is determined by the tunnelling barrier height (Φ_B). Assuming the effective mass of $0.5m$ for holes in hBN [203], most of the devices exhibit a barrier height of ∼1.7 eV, which is close to high-quality hBN without defects (∼1.8 eV). Therefore, the I-V characteristics of the fabricated devices are consistent with Fowler–Nordheim tunnelling, with hole injection from graphene into the valence band edge of hBN being the dominant contribution to the current. The slightly reduced barrier height in the devices is potentially due to trap assisted tunnelling. A detailed analysis of Fowler-Nordheim tunnelling in graphene-hBN heterostrcutres and the effects induced by defect-assisted mechanisms are provided in appendix B.1. On the other hand, tunnelling injection of electrons (red arrow in Figure 5.2f) requires higher voltages than holes because of the larger barrier height (i.e., $\Phi_B^e > \Phi_B^h$) [203, 204]. As a result, EL can emerge at higher voltages than the tunnelling current (Figure 5.2d). Then, considering the EL process itself, charge injection may occur via both band-edge states and in-gap defect states. Following injection, electrons and holes can travel through the hBN layer and be captured by luminescent defects, where recombination gives rise to the observed emission. The schematic in Figure 5.2f represents a simplified illustration of the carrier injection and recombination

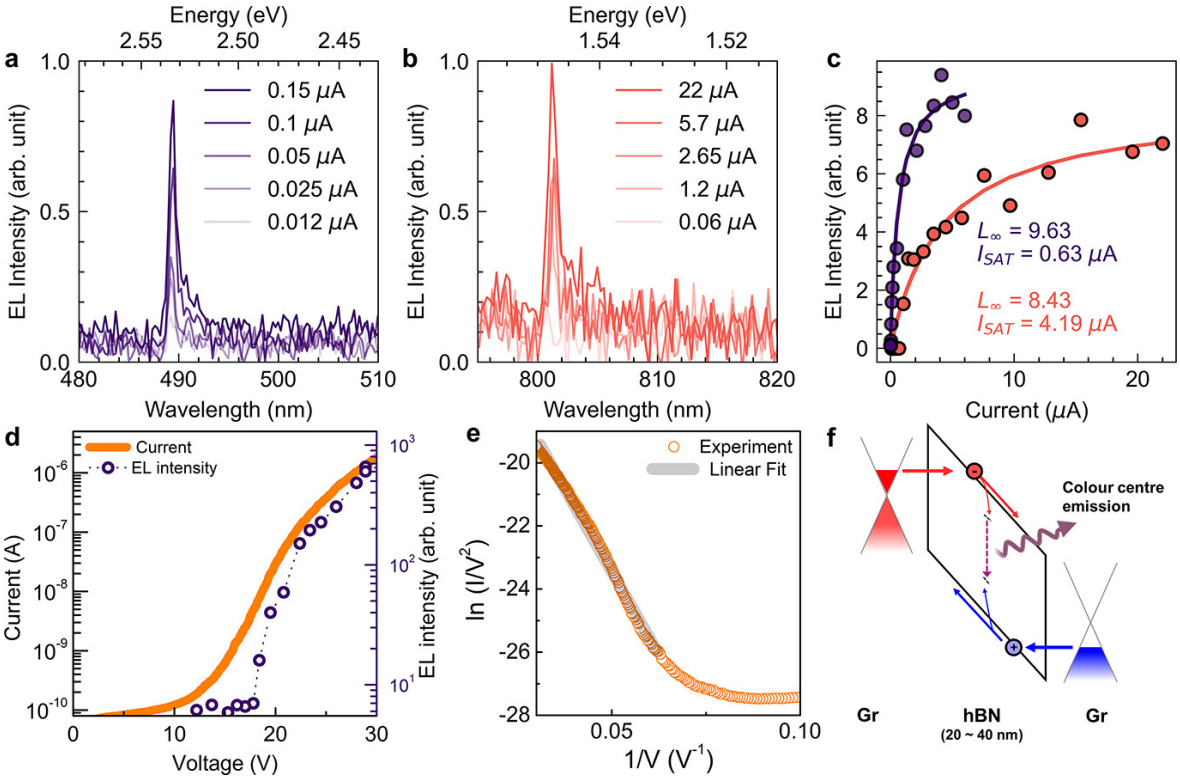


Figure 5.2: ***Electrical excitation mechanism of hBN colour centres in vdW heterostructures at cryogenic temperatures (10 K).*** ***(a)*** *EL spectrum of an emitter with ZPL at 490 nm.* ***(b)*** *EL spectrum of an emitter with ZPL at 801 nm.* ***(c)*** *EL intensity-current characteristics of emitter in (a) and (b). All spectra are taken at 10 K temperature.* ***(d)*** *I-V characteristic and applied voltage-dependent EL intensity of a visible emitter at temperature of 10 K.* ***(e)*** *Fowler-Nordheim plot corresponding to the I-V characteristics in (d).* ***(f)*** *Schematic illustration of the electrical excitation mechanism of the colour centre emission in monolayer graphene encapsulated hBN.*

pathways.

Following, detailed optical properties of the electrically driven colour centres were investigated. Measurements were carried out at a temperature of 10 K, to provide a better signal-to-noise ratio of the narrowband emitters observed in EL. Figure 5.4a shows a narrowband EL from a defect with a ZPL at ∼519 nm. Under electrical excitation, full emission polarisation profile of the same defect is shown in the inset of Figure 5.4a. The EL exhibits an apparent dipole emission pattern. A linearly polarised photon emission is a common feature of visible single photon emitters in hBN [132, 206]. The high visibility value of the dipole pattern suggests that the ZPL emission could stem from a single colour centre, which is reinforced by the idea of a single electric dipole transition between ground and excited energy states [132, 207]. These results also indicate that the optical transition dipole moment is largely in-plane, which is common for most emitter classes in hBN [132, 207]. Example spec-

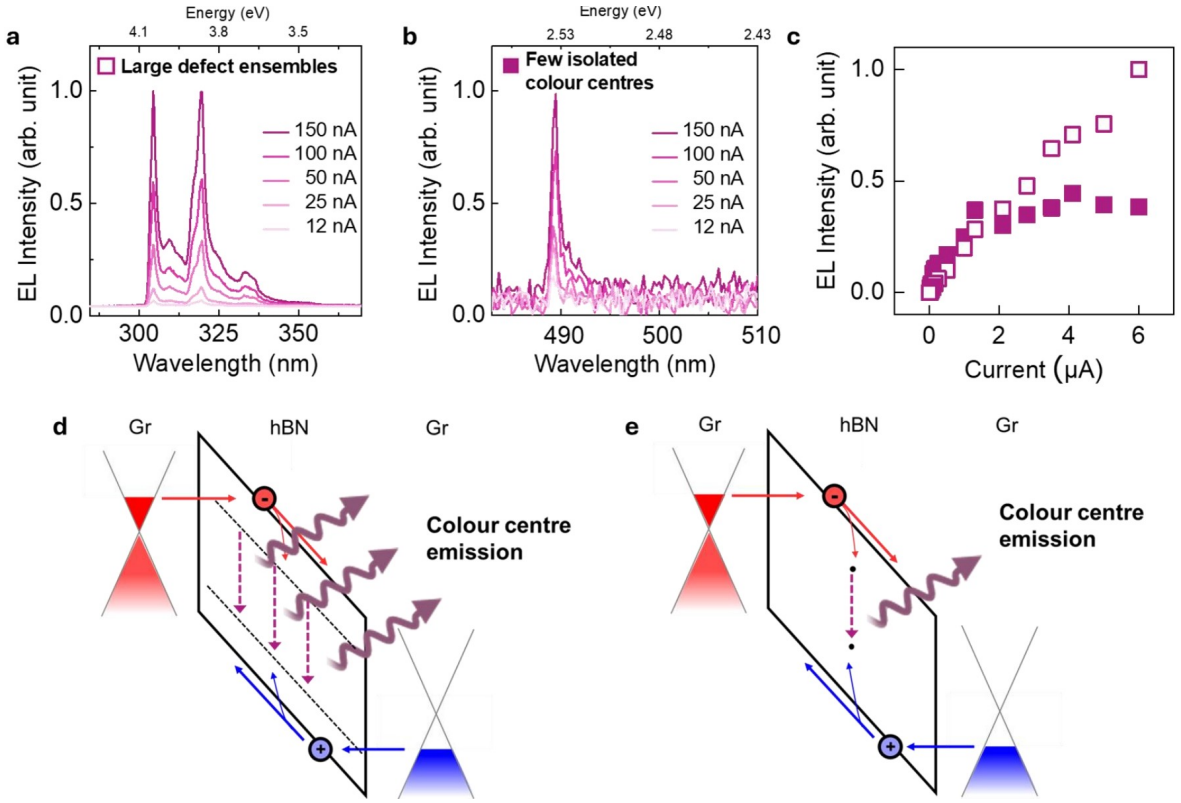


Figure 5.3: ***I-L characteristics of colour centres in hBN.*** ***(a)*** *Near-ultraviolet EL spectra from large ensembles of colour centres at 4.1 eV.* ***(b)*** *Visible EL spectra from few isolated colour centres.* ***(c)*** *I-L characteristics of large defect ensembles in (a) (empty squares) & few isolated colour centres emission in (b) (filled squares). All EL spectra are taken at a temperature of 10 K. Schematics of luminescence processes for large defect ensembles* ***(d)*** *and few isolated colour centres* ***(e)****. Large defect ensembles provide a large density of states which are not saturated under current injection. Few isolated colour centres can be readily saturated by small current injection due to limited density of states.*

tra of other electrically excited emitters with ZPLs spanning visible to NIR spectral ranges are shown in Figure 5.5. Additional analysis of polarisation measurements, highlighting their significance to the localised nature of the observed colour centres, is presented in Figure 5.6. All of the observed narrow EL lines in fabricated devices exhibit fully polarised emission, a convincing indication of the single photon emission nature of the defects. Next, optical stability was examined, taking the 519 nm along with 493 nm and 549 nm colour centres. The measurement is presented in Figure 5.7 as a colour map of spectral acquisitions with over 3 min of total duration. All three colour centres maintained their ZPL centre wavelength fluctuations below 0.7 nm, with FWHM values of 519 and 493 nm colour centres remaining below 2 nm. Note, that all three colour centres showed no reduction in lumines-

cence intensity over the duration of the whole measurement, highlighting stability of the device and electrical excitation method.

To unveil photon statistics of the emitted light from hBN colour centres and further confirm their non-classical nature, second order autocorrelation measurement was conducted on an electrically driven emitter with a ZPL at ∼492 nm (Figure 5.4b). The acquired histogram resulted in a subtle dip at zero time delay, $\tau = 0$. The dip can be better visualised by the binned data that falls below the average counts line at $\tau = 0$, signifying quantised photon emission from this colour centre. Interestingly, the 492 nm colour centre displayed bunching characteristics, therefore a three-level system $g^{(2)}(\tau)$ function of the form $g^{(2)}(\tau) = 1 - (1 + A) \cdot e^{\frac{-|\tau|}{\tau_1}} + A \cdot e^{\frac{-|\tau|}{\tau_2}}$ was used, where A is the bunching amplitude, and τ_1 and τ_2 are antibunching and bunching lifetimes, respectively. The fit parameters yielded lifetimes of 11.7 and 11.8 ns for τ_1 and τ_2, respectively. The strong bunching could be attributed to background emission or detector artefacts, such as afterpulsing. Nevertheless, a resulting value of $g^{(2)}(0) = 0.77 \pm 0.05$ (without a background correction) was observed, where the uncertainty was obtained by propagating the covariance of the fitted three-level model parameters. This demonstrates non-classical light emission from an isolated or a small ensemble of emitters.

hBN defects are well-known to exhibit narrowband quantum emission under optical excitation even at room temperature [90]. Therefore, EL operation of fabricated devices was conducted at 300 K. To begin, a common spatial EL emission profile was observed on a wide-field microscope. Under bias voltage of 24 V, strong and localised EL signals were present, shown in the luminescence image (Figure 5.8a). Emissions are mostly located inside and near the overlapped region of top and bottom graphene electrodes where charge carriers are injected into hBN defects. A weak signal outside the junction area is attributed to carrier diffusion and leakage paths into a nearby slot. This emission remains significantly weaker and does not contribute to the primary defect-related luminescence discussed here. Exemplary EL spectra from emitters are shown in Figure 5.8(b-d). The emitter in Figure 5.8d was further analysed in Figure 5.9, where the sharp emission centred around 521 nm was attributed to the ZPL transition of the defect in hBN [90, 203]. A Lorentzian fit to the ZPL reveals a narrow FWHM linewidth of 16 meV (3.50 nm). The second prominent sideband feature at 560 nm is the defect's PSB, red-shifted from the ZPL by 171 meV, typical of the high energy optical phonon modes in hBN [208]. Within the same device, other colour centres spanning a range of emission energies were also electrically excited. The conducted EL measurements on hBN colour centres revealed that the emitters maintain the same signature emission profiles, as during optical excitation even at room temperature. The emission consists of narrowband ZPL transition accompanied by less intense contribution from its

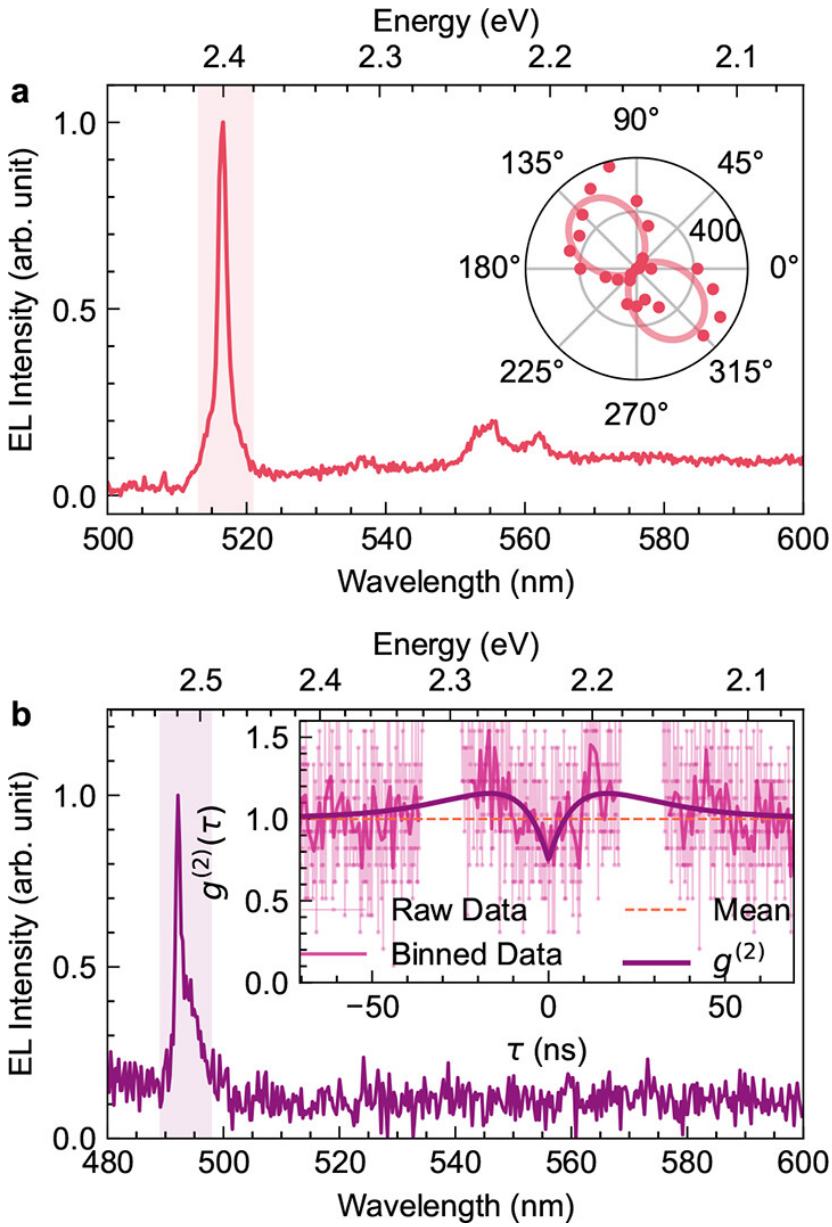


Figure 5.4: ***Optical properties of electrically driven hBN colour centres at cryogenic temperatures (10 K).*** ***(a)*** *EL spectrum of hBN colour centre with ZPL emission at 519 nm and inset showing the linear emission polarisation profile of the emitter.* ***(b)*** *EL spectrum of hBN colour centre with ZPL emission at 492 nm. Inset displays the second order autocorrelation measurement of this emitter, where light pink is raw acquired data to which the fitted $g^{(2)}(\tau)$ function yields $g^{(2)}(0) = 0.77$. For clearer presentation, binned data and histogram average value were added as dark pink and dashed orange lines, respectively.*

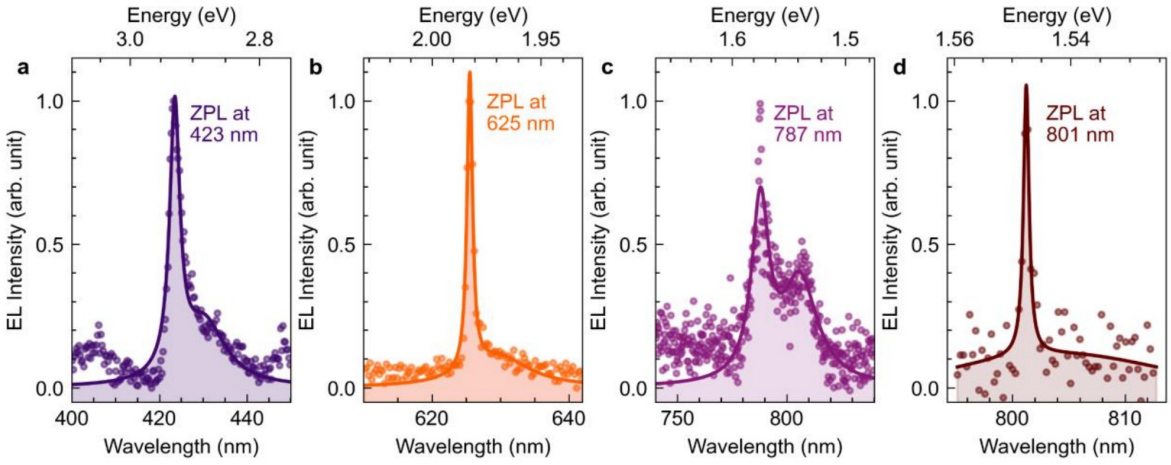


Figure 5.5: ***10 K EL emission spectra of colour centres spanning visible to NIR wavelength range. (a-d)*** *panels represent one EL spectra each of individual hBN colour centres observed from the same device. Double Lorentzian fits indicate ZPL centre wavelength values of 423 nm, 625 nm, 787 nm, and 801 nm for (a), (b), (c), and (d), respectively.*

acoustic modes and displays in-plane polarisation.

To highlight the stability of fabricated heterostructure devices to electrically excite hBN colour centres, a series of measurements was conducted for extended time periods on each device. An evaluation of electrically driven luminescence characteristics and emission stability of colour centres is described in the bottom panels of Figure 5.8, focusing attention to a colour centre with ZPL positioned at 518 nm. As seen in Figure 5.8d, the EL spectrum displays two dominant features: a higher energy, narrow peak, which is attributed to a localised acoustically broadened ZPL transition, and a lower energy PSB centred around 564 nm. The stability measurement consisted of recorded EL spectra with 1 min intervals over 23 min, underscoring the consistency of the luminescence in terms of intensity and wavelength position. The fit parameters of the ZPL line, discerned via a triple Lorentzian fitting approach on the spectra, are elaborated in Figure 5.8(e-g). The ZPL is described by the first Lorentzian peak of the total fitting function, which displays a centre wavelength within one nanometre fluctuation, with a FWHM value of $\sim$5 nm ($\sim$25 meV) over the whole time period. Additionally, during the measurement, intensity of the ZPL also maintained its brightness, as evident from the consistent EL intensity, which is derived from photon counts. Both heterostructure devices and colour centres showed outstanding stability.

Lastly, possible origin of the observed emissions is proposed. It is known that carbon-doped hBN flakes host a variety of carbon-related defects spanning the UV to the visible range. Specifically, carbon dimers are responsible for 4.1 eV UV emission [137], while donor-acceptor pairs [209], double-site [139], and more complex clusters of carbon and vacancy

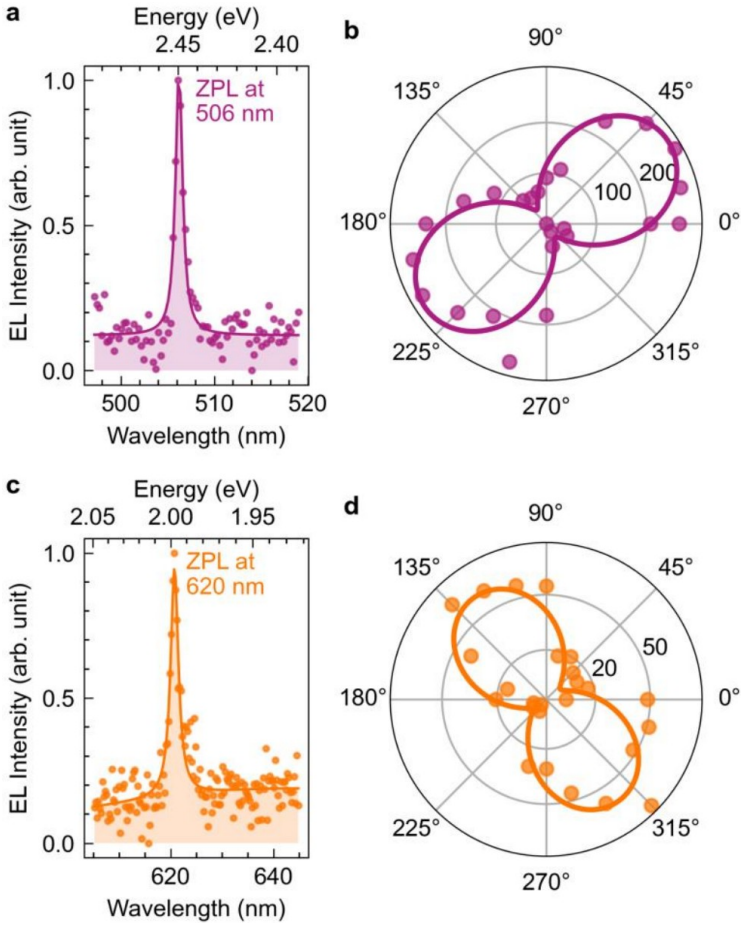


Figure 5.6: ***10 K EL emission polarisation profiles of visible colour centres.*** ***(a)*** *Spectrum of hBN colour centre with 506 nm ZPL centre wavelength position taken at 30 V with 23 ∼A current.* ***(b)*** *Polar plot displaying emission polarisation profile of the 506 nm colour centre.* ***(c)*** *Spectrum of hBN colour centre with 620 nm ZPL centre wavelength position taken at 30 V with 23 µA current.* ***(d)*** *Polar plot displaying emission polarisation profile of the 620 nm colour centre.*

configurations can produce emissions in the visible range. The high carbon concentration in the emissive layer hBN flakes used in the fabricated devices suggests that the observed transitions most likely originated from defects consisting of a system employing carbon atoms. The spectral composition of the emission supports this statement, as the ZPL transition is accompanied by two phonon sideband modes with the energy detuning values resembling those in the reported literature [210]. It is also common for hBN visible range colour centres that produce highly polarised linear emission to form C_{2v} symmetry defects [211].

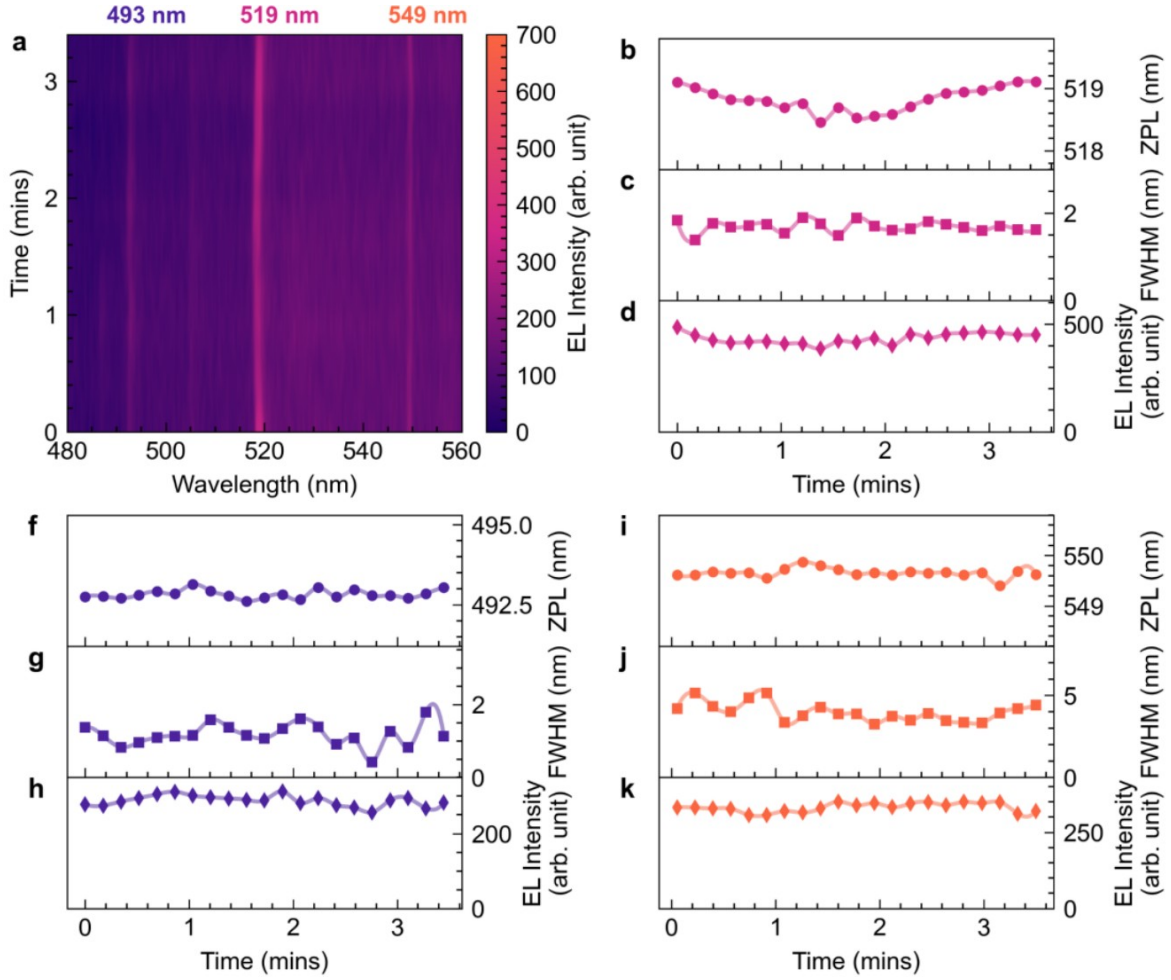


Figure 5.7: ***Cryogenic temperature 210 seconds measurement of EL stability of visible colour centres, conducted at 30 V with 23 μA current.*** ***(a)*** *Colour map plot of stability measurement that consists of continuous spectrum acquisitions with 10 seconds integration time each and wavelength range of 480 nm to 560 nm.* ***(b)***, ***(c)***, *and* ***(d)*** *describe fluctuations of ZPL, its FWHM and its intensity, respectively, as a function of time for the 519 nm colour centre shown in pink in (a) and in Figure 5.4a.* ***(e)***, ***(f)***, *and* ***(g)*** *show fluctuations of ZPL, its FWHM and its intensity, respectively, as a function of time for the 493 nm colour centre.* ***(h)***, ***(i)***, *and* ***(j)*** *show fluctuations of ZPL, its FWHM and its intensity, respectively, as a function of time for the 549 nm colour centre.*

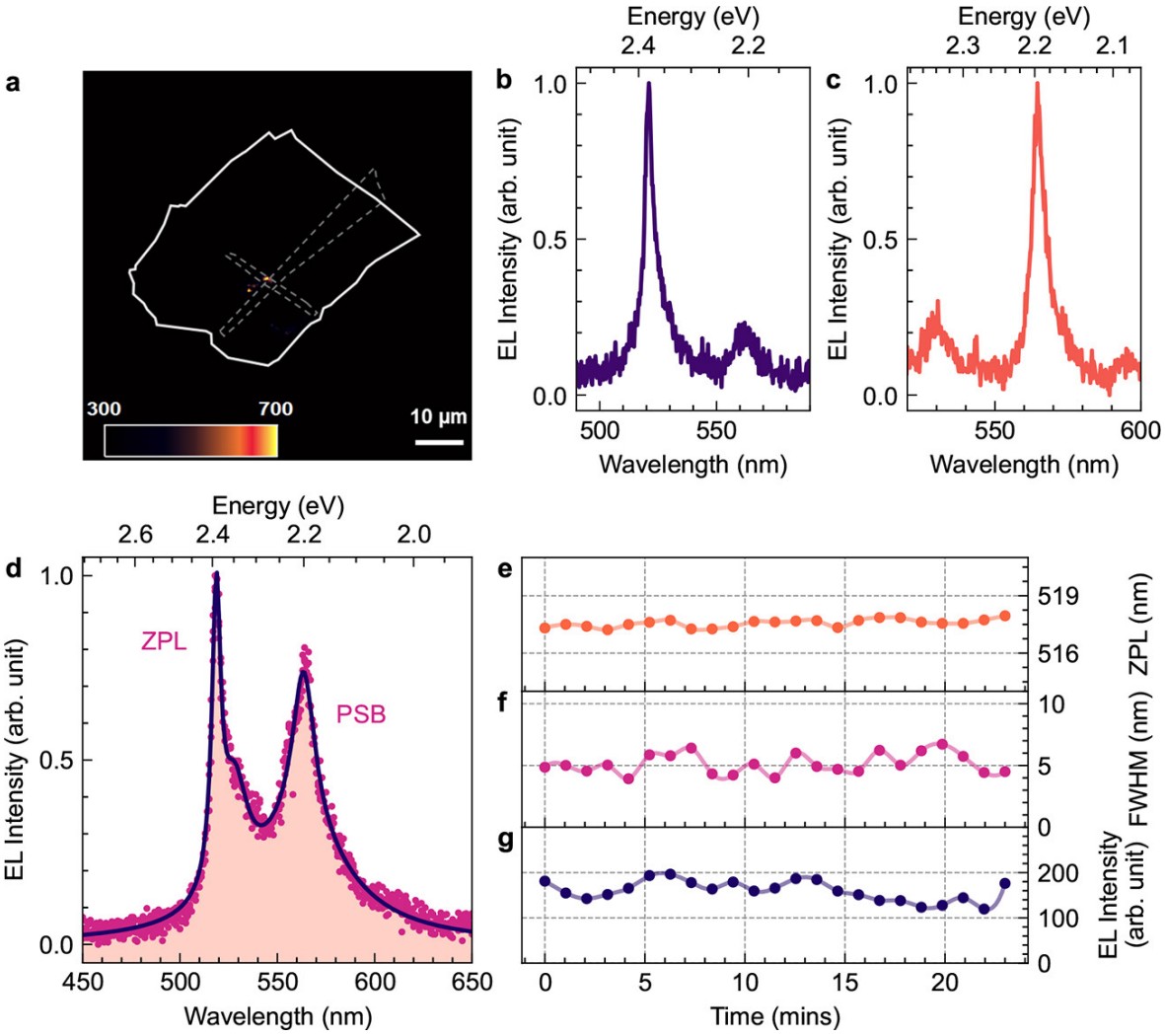


Figure 5.8: ***Room temperature EL measurements of hBN colour centres.*** ***(a)*** *Spatial profile of the EL emission, localised inside and near the graphene overlap region. hBN is highlighted with a white solid line. Gray dashed lines indicate top and bottom graphene electrodes.* ***(b,c)*** *Representative EL spectra from two colour centres found in two separate devices.* ***(d)*** *Exemplary EL spectrum of a colour centre used for the stability analysis.* ***(e-g)*** *Extracted centre wavelength, FWHM and intensity values, respectively, of the ZPL transition over 23 min duration with each data point representing a 60 s long spectrum acquisition. Time-averaged FWHM corresponds to ∼5 nm (∼ 25 meV).*

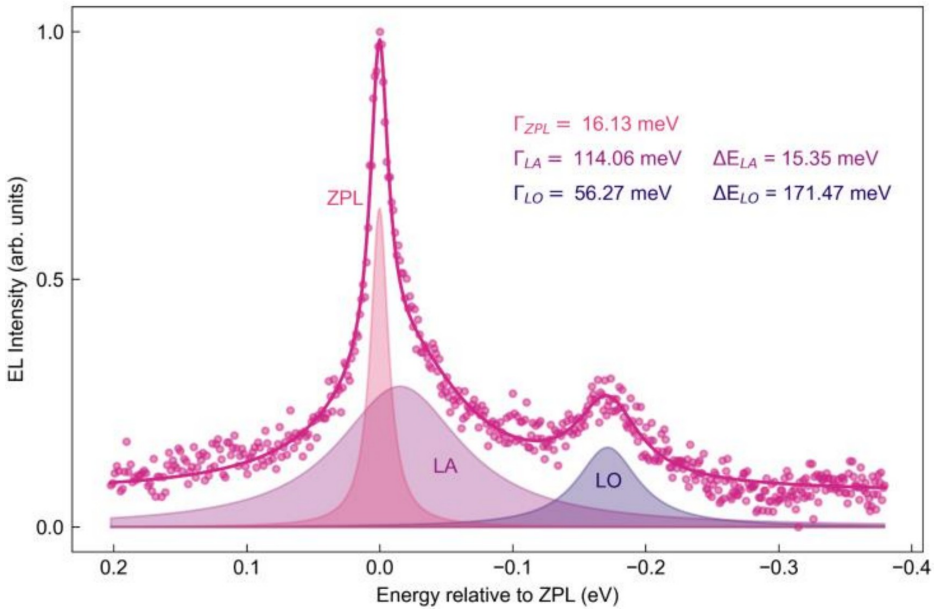


Figure 5.9: ***ZPL and PSB calculation of colour centre in Figure 5.8b.*** *The horizontal axis is the spectral energy relative to the ZPL energy 2.38 eV (521.08 nm).*

5.3 | Summary

To summarise, vdW heterostructure consisting of hBN and graphene layers were engineered and exhibited stable EL from colour centres in hBN, persistent even at room temperature. Remarkably, the emission spanned the visible and NIR spectral ranges, which are areas of interest for quantum technologies. Device performance was carefully analysed through investigation of electrical current and luminescence as a function of voltages, which assigned the major electrical excitation mechanism to tunnelling injections of electrons and holes. These results usher in a new era in electrically driven vdW devices for on-chip quantum technologies [67] and propel hBN as a material of choice to realise these devices. This work advances the hBN colour centres in quantum applications by laying important groundwork for future development of hBN quantum devices. The vertical heterostructure stacking is also compatible with large scale engineering [67], as well as integration with on-chip photonic waveguides and cavities, to then couple the circuit components.

6

Electrical Generation of hBN Quantum Emitters

This chapter explores additional capabilities enabled by the developed device architectures, with a particular focus on electrical generation of quantum emitters (colour centres) in hBN using locally applied electric fields. It is demonstrated that colour centres can be generated and subsequently electrically excited at the junction of electrodes, allowing for spatially localised emitter arrays. The device operating regimes required for controlled emitter formation, minimised background emissions, and prolonged electrical excitation are outlined in detail.

Results presented in this chapter were published in journal *ACS Applied Materials & Interfaces* [212] titled *"Electrical Generation of Color Centers in Hexagonal Boron Nitride"* and serve as practical guidelines for reliable operation of novel quantum optoelectronic devices.

6.1 | Context

Solid-state crystals are an attractive platform for advancements in quantum technologies [5, 67, 94], as they host crystal lattice defects that function as quantum emitters [12, 72]. Defects formed within wide band gap materials may introduce midgap energy levels that are isolated from the electronic bands. These levels consist of excited and ground states that can be optically addressed to generate narrowband single photons, even at room temperature [102]. Wide band gap materials also enable site-specific creation of colour centres with reproducible ZPL transitions [118, 119, 213], corresponding to electron decay from the excited state to ground state of the isolated two-level system. These properties, combined with various optical protocols, make such systems suitable for applications in quantum communication [3, 12, 80], electric and magnetic field sensing [24–26], and qubit generation [214].

For integration into on-chip quantum photonic circuits, electrical excitation of colour centres is desired [191, 192]. This is typically realised in materials with well-established doping techniques for the creation of p-n junctions [197–199]. hBN, as a vdW material, is particularly suitable for integration into on-chip quantum photonic circuits, enabling the realisation of compact solutions [215]. However, the large band gap ($\sim$6 eV) of hBN causes challenges for p- or n-type doping. Instead, hBN offers an alternative pathway to colour centre EL, leveraging the layered nature of vdW materials and exploiting quantum mechanisms for charge injection. Furthermore, hBN has been a well-established platform host of bright, high-purity colour centres spanning the visible to NIR wavelength range [90, 107, 207]. Yet, their electrical excitation is still in its infancy and has only seen progress in recent years due to the complexity of charge injection and stable colour centre excitation. Few studies applied different approaches of charge injection into the hBN layer for electrical excitation of its colour centres [145, 189, 216]. Thus, it is critical to further investigate not only the electrical excitation, but also the field-driven generation of hBN luminescent defects and the underlying device physics governing their formation. Understanding defect dynamics under high localised electric fields enables spatially deterministic creation of emitters within vdW heterostructures. Future works could then explore novel on-chip devices that use less destructive emitter generation methods via more advanced electrode engineering for precise generation of defects within a few nanometre scale.

This chapter shows fabrication of quantum tunnelling vdW devices to enable charge injection into hBN layers. Series of experiments were performed aimed to identify the electric field strengths required for generation of colour centres. Electrical characterisation of the devices was carried out to quantify changes in the electrical properties of hBN devices concurrent with defect generation. Time-resolved analysis highlights spontaneous appearance of luminescent colour centres as well as charge trap generation at high applied electric fields. Generated emitters displayed very narrowband ZPL transitions at cryogenic temperatures with their wavelength mapped as a function of the applied electric field. Additionally, detailed saturation analysis showed the importance of optimising device operation in order to minimise background emissions and ensure prolonged stability of both colour centres and devices. Lastly, this chapter reports on the observation of room-temperature electrical control of PL intensity from an electrically generated colour centre.

The study provides a guideline for generation and excitation of hBN colour centres with electric fields. Optimal conditions for minimised background and prolonged device operation are discussed. Room-temperature electrical control of PL was observed, highlighting future research directions.

6.2 | Results

hBN EL devices were fabricated using a dry transfer technique, as detailed in Chapter 3. The devices consisted of an emissive layer of hBN with a thickness ranging from 20 to 40 nm, sandwiched between monolayer graphene sheets forming vertical devices. An electric field was applied across graphene layers to enable charge carrier injection, electrical generation, and excitation of colour centres within the hBN layer. Figure 6.1a illustrates the structure of the hBN EL device, highlighting the applied electric field that facilitates charge tunnelling and excitation of luminescent colour centres present in hBN. As discussed in previous works [151, 189, 203, 204], injection of both charges in hBN devices with low-impurity density mainly follows Fowler-Nordheim tunnelling mechanism [205] at cryogenic temperatures, as indicated in equation 6.1.

$$\ln\left(\frac{I}{V^2}\right) = \ln\left(\frac{A_{\text{eff}} q^3 m}{8\pi h \Phi_B m^* d^2}\right) - \frac{8\pi\sqrt{2m^*}\Phi_B^{3/2} d}{3hq} \cdot \frac{1}{V} \tag{6.1}$$

where I is the tunnelling current, V is the bias voltage, A_{eff} is the effective tunnelling area, q is the elementary charge, m is the free electron mass, Φ_B is the tunnelling barrier height for charge carriers at the electrode and the insulator interface, h is Planck's constant, and m^* is the effective mass of charge carriers in the insulator. A linear relationship between $ln(I/V^2)$ and $1/V$ indicates the Fowler-Nordheim tunnelling mechanism when the equation is further formulated. Additional details on this analysis are in Appendix B.2. Note, that after operating the devices in high-field regime, which is above the stable region, for an extended period and generating numerous defects, the I-V characteristics undergo significant changes and follow a defect-related tunnelling mechanism rather than the pristine Fowler-Nordheim tunnelling behaviour [217–220]. This chapter focuses on two distinct operating regimes of the hBN EL device: low and high electric fields. In the high-field regime ($\gtrsim 0.75$ V.nm^{-1}), electrical charge injection generates hBN colour centres and electrically excites them for a short period of time (within 1 h). The low-field regime allows for prolonged excitation (several hours) of the generated luminescent defects. Generation of colour centres may arise from either the formation of new defects or changes in charged states of other pre-existing defects via electrical doping within the hBN emissive layer. This behaviour is schematically depicted in Figure 6.1b, where the low-field regime is represented by the excitation of only a few pre-existing colour centres, while the high-field regime shows the appearance of EL of additional colour centres alongside continued excitation of the original centres. Notably, non-luminescent defects are also formed during this process.

Throughout this chapter, carbon-doped hBN, hBN:C was used. Carbon incorporation introduces a higher density of defect states, increasing the probability of defect activation and

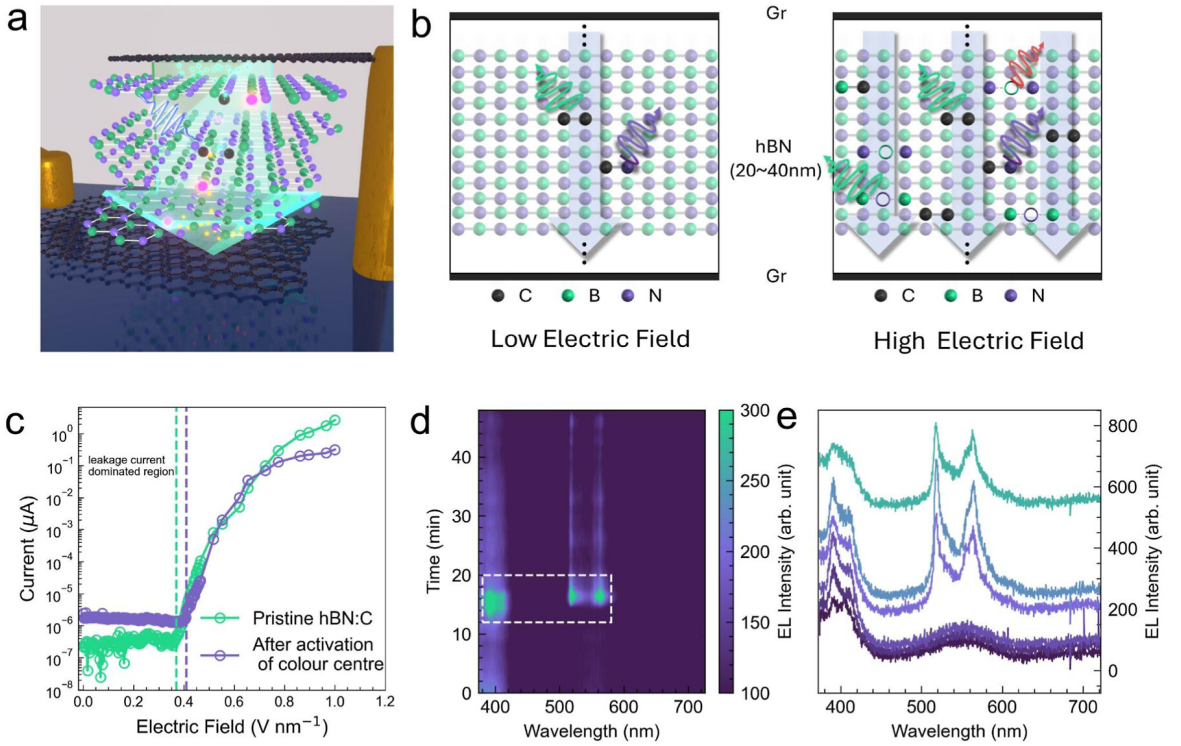


Figure 6.1: ***vdW device illustration, electrical characterisation, and room-temperature colour centre EL spectra.*** ***(a)*** *3D illustration of the hBN colour centre EL device.* ***(b)*** *Schematic of operation of hBN EL devices. A low applied electric field excites pre-existing colour centres within the hBN layer (left), while a high electric field generates new colour centres and charge traps as well as produces EL from the same and newly generated colour centres.* ***(c)*** *Typical I-V characterisation behaviour of a device prior and post colour centre generation.* ***(d)*** *Time evolution of a device operated in high-field regime (0.83 V.nm^{-1}) at room temperature. Highlighted white dashed line shows initial appearance of a high-energy (390 nm) narrowband emission peak. Within a few minutes, lower-energy emission at 519 nm appears while the narrowband 390 nm peak disappears, leaving dimmer broadband emission in that region. Spectra of the highlighted transition section are shown in* ***(e)*** *and offset vertically for clarity. Each spectrum corresponds to 60 s acquisition interval within the 12-20 minute range in (d).*

formation of luminescent colour centres under applied electric fields. The I-V characteristics of the device were measured up to approximately $\sim$1 μA and are summarised in Figure 6.1c. The green curve represents the pristine hBN:C I-V behaviour during initial device operation, prior to the formation of observable defects. The purple curve represents I-V characteristics after colour centres generation at 10 K. When an electric field is applied, the device response exhibits two distinct regions, where one region is dominated by leakage current and the other is governed by tunnelling current. Upon observing colour centres generated by electric fields, turn on voltage – bias at which current begins to increase drastically via field emission in the low-field regime – produces an observable shift (vertical dashed lines). This shift can occur in both directions attributed to charge trap generation or the filling of additional defect states [144, 146], suggesting that the charge-related properties of the device have been altered as a result of the electrical interactions between defects within the device. However, the device retains the I-V characteristics of the pristine hBN:C I-V, meaning that it continues to operate similarly despite the formation of low density defects.

Next, by using a scanning confocal microscope, spatial map of EL photon counts intensity was recorded when the device is operated in both low and high electric field regimes. Figure 6.2 contains an optical microscope image as well as a confocal microscope EL intensity map of one of the devices. From Figure 6.2b, low photon counts on the detector originate from well-defined tunnelling regions that are primarily at graphene edge overlaps and the surrounding area where carriers can diffuse due to the current spreading. The bright luminescence region confined to a single confocal spot corresponds to a locally positioned colour centre that is electrically excited. Within this single confocal spot, if the device is operated at a high electric field, over time newly generated luminescent defects spontaneously appear and slowly degrade in emission intensity. Studying further time resolved EL appearance of hBN colour centres. For example, Figure 6.3 shows that after some time has elapsed since the device was turned on, a colour centre peak emerged at 490 nm. Over time, peak intensity decreased because the device was still operated in a high-field regime. Prolonged excitation at high-field or excessively large-field magnitudes is also able to quench colour centres due to a multitude of effects including charge doping [144, 146, 147], breaking of bonds [221], and more. Further, this chapter shows that it is possible to extend electrical excitation of generated colour centres up to 36 h if the electric field strength is lowered post generation. Interestingly, these luminescent defects can also exhibit dynamic behaviour, emitting higher-energy photons initially, before undergoing a permanent rapid shift to a lower energy transition. This phenomenon is illustrated in Figure 6.1d,e. Under a high electric field operation, the hBN EL device initially exhibits negligible emission. After approximately 15 min, a distinct peak emerges at 390 nm, corresponding to high energy emission. Within 4 min, the emission transitions to a lower-energy ZPL centred at 517 nm. Figure 6.1d presents spectra

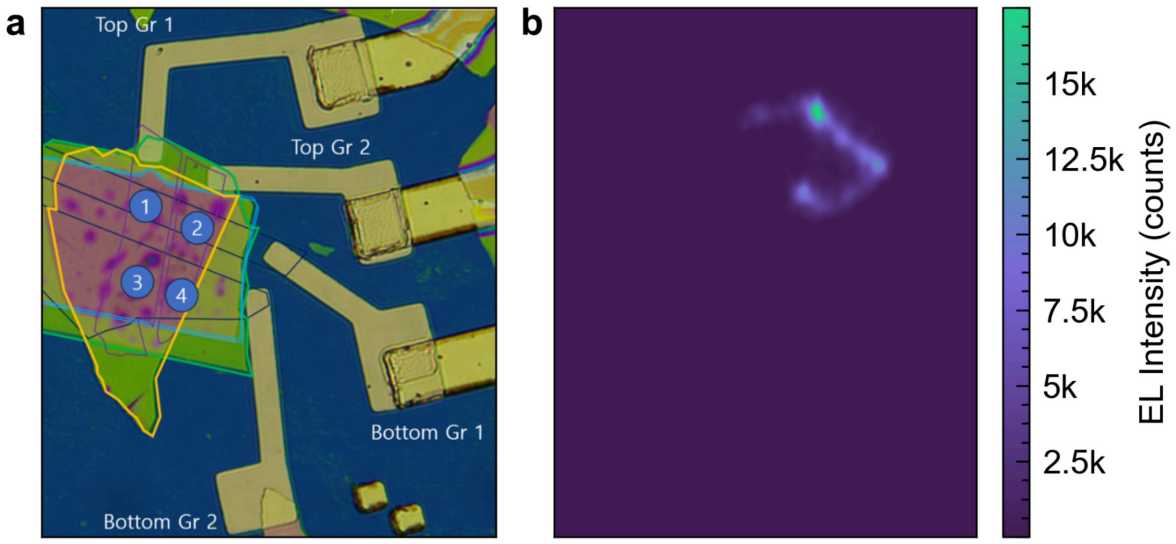


Figure 6.2: ***Optical and EL imaging of the fabricated device.*** ***(a)*** *Annotated optical image highlighting gold contacts connecting graphene electrodes in the heterostructure stack. Slot indices are labelled.* ***(b)*** *Confocal microscope raster scan of EL intensity captured with an avalanche photodiode detector. The observed luminescent regions correspond to the graphene overlap areas and are primarily localised along the edges of the electrode slot (Slot 1 in (a)), where charge injection occurs. Note, (a) and (b) are not to scale with each other.*

acquisitions showing this progression during high-field operation, while Figure 6.1e is the highlighted section of individual spectra.

The mechanism of colour centre generation under high electric fields is likely governed by a combination of factors. Under strong electric fields, highly energetic carriers can induce local bond breaking or atomic rearrangements within the hBN lattice, forming new defect complexes. In parallel, charge states of existing non-emissive defects can be modified, activating optical transitions. The observed time-dependent spectral evolution suggests an interplay between defect creation, charge trapping, and local electric field redistribution within the device.

As discussed prior, application of a high electric field results in the generation of colour centres that are also electrically excited. Emission wavelength distribution of these colour centres spans the visible to NIR range. The scatter plot representing ZPL transition wavelengths as a function of applied electric field at which the colour centres first appeared is shown in Figure 6.4a. More than half of the observed electrically generated colour centres have ZPL transition wavelengths falling within the 500-624 nm range. Interestingly, the electrical field generation method showed a high chance of generating colour centres with emission wavelengths in the range of 499-503 nm, which can occur anywhere within the range of 0.75 V.nm^{-1} to just above 1 V.nm^{-1}. Also note that generation of colour centres

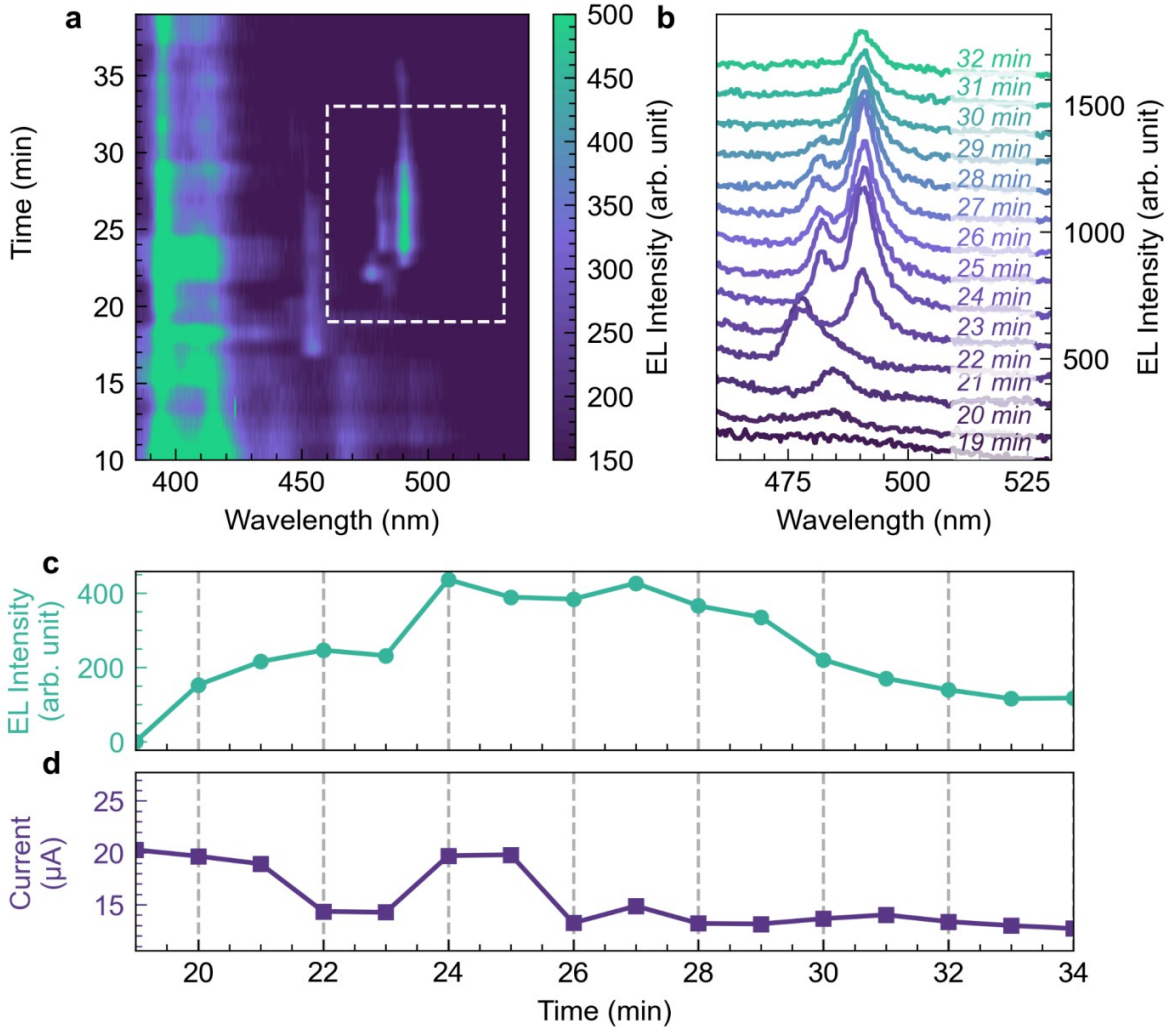


Figure 6.3: ***Room temperature time-resolved EL of hBN colour centres.*** ***(a)*** *Time-resolved EL spectra recorded at 1-minute acquisitions with the device operated in high field regime.* ***(b)*** *Highlighted EL spectra from the dashed white box region in (a) during the 19-32 minutes time frame, showing appearance of a strong luminescent peak around 490 nm.* ***(c)*** *Time-resolved EL peak intensity of a colour centre extracted from the spectrum in (b).* ***(d)*** *Corresponding current values according to each spectrum in (b) recorded simultaneously with the EL measurements.*

typically required a mean electric field of 0.88 V.nm^{-1}. Figure 6.5 investigates the dependency of ZPL values of generated colour centres on hBN thickness and across different devices. In the thickness range of 20-45 nm, the results confirmed that there is no specific relationship between these parameters, except for their distribution within the visible to NIR range. Tunnelling current values were not included in this analysis because tunnelling current conditions can vary drastically and are rather determined by the changing defect density and electronic environment of the hBN layer. Since the high-field regime also forms charge traps, tunnelling current magnitude is reduced upon generation of defects within hBN [221]. However, emissive hBN layer is 20-40 nm thick and consists of many layers allowing for generation of multiple new different colour centres over time within the volume of a confocal focus. Throughout this period, other defects in hBN are constantly generated, continuously altering electrical properties of hBN. As a result, depending on the condition of the emissive hBN layer, the tunnelling current value at which a colour centre is created varies more significantly than the electric field.

The generated colour centres commonly exhibit very narrowband emission transitions that are often spectrometer limited at a 300 L/mm grating, as demonstrated in the spectra in Figure 6.4b. From the previous work, it was shown that emissions exhibit double Lorentzian profiles that consist of a ZPL and a phonon sideband [189] and can be expressed in the form

$$L(x) = a_1 \cdot \frac{w_1^2}{(x - c_1)^2 + w_1^2} + a_2 \cdot \frac{w_2^2}{(x - c_2)^2 + w_2^2} \tag{6.2}$$

Here, a_i are amplitudes, w_i are width parameters, and c_i are central frequencies of the first and second Lorentzian components, respectively. Such a profile is commonly maintained for most colour centres throughout the visible to NIR spectrum regardless of the ZPL energy and is also demonstrated in this work with the obtained FWHM values in Figure 6.4c,d falling below 0.26 nm. The plotted spectra in Figure 6.4c,d were acquired in low and high applied electric fields, respectively, highlighting that such narrowband transitions occur in both regimes.

When the devices are operated in a high-field regime, in addition to generating and electrically pumping hBN colour centres, a second type of emission that spans broadly across the visible spectral range is also produced. Figure 6.6a shows three representative spectra obtained from an EL device at three distinct electric field regimes, highlighting two emission components that are particularly obvious during high-field operation. This work reports on observation of a broad emission spectrum that begins to dominate above 0.8 V.nm^{-1} and likely arises from thermal emission due to current flow in tunnelling regions or from transitions between sub-bands and midgap defects [145]. In contrast, the narrowband emission is characteristic of hBN colour centres, originating from localised defect states that emit pho-

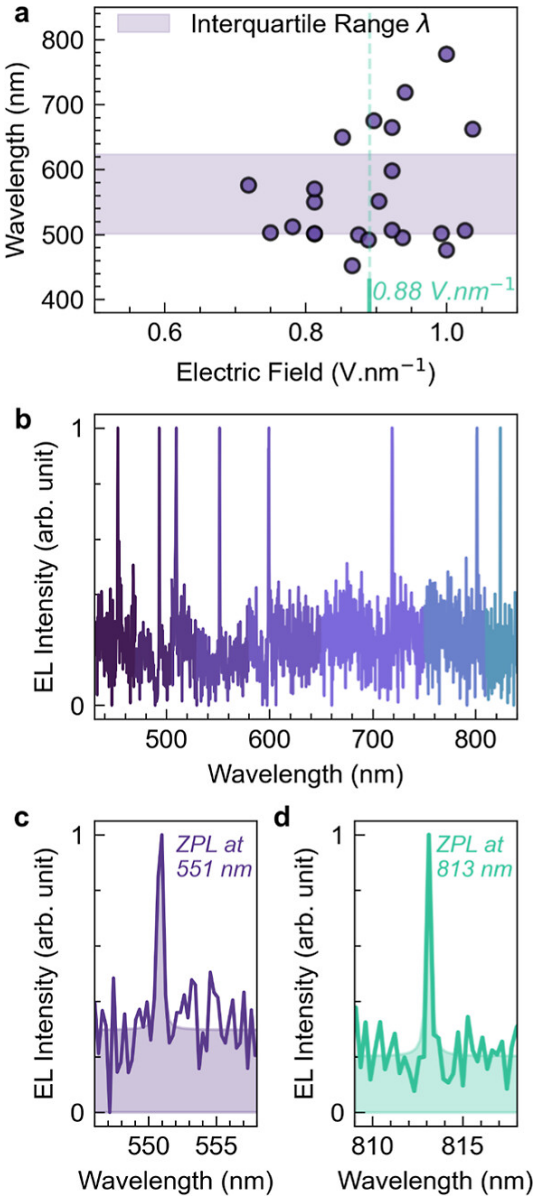


Figure 6.4: ***Electric field parameters for generating colour centres and representative EL spectra.*** ***(a)*** *Scatter plot representing wavelength distribution of colour centres generated at a specified electric field. More than half of the colour centres have transitions within the 500-624 nm range, as shown by the interquartile range shade. The mean electric field for generating colour centres in hBN is 0.88 V.nm^{-1}.* ***(b)*** *Selected representative spectra of generated colour centres spanning the whole visible to near-infrared range.* ***(c,d)*** *High-resolution spectra of those in (b), acquired in low- and high-field regimes, respectively. Double Lorentzian fits were used for fitting, yielding FWHM values of 0.17 and 0.25 nm for colour centres at 551 and 813 nm, respectively. Measurements conducted at 10 K.*

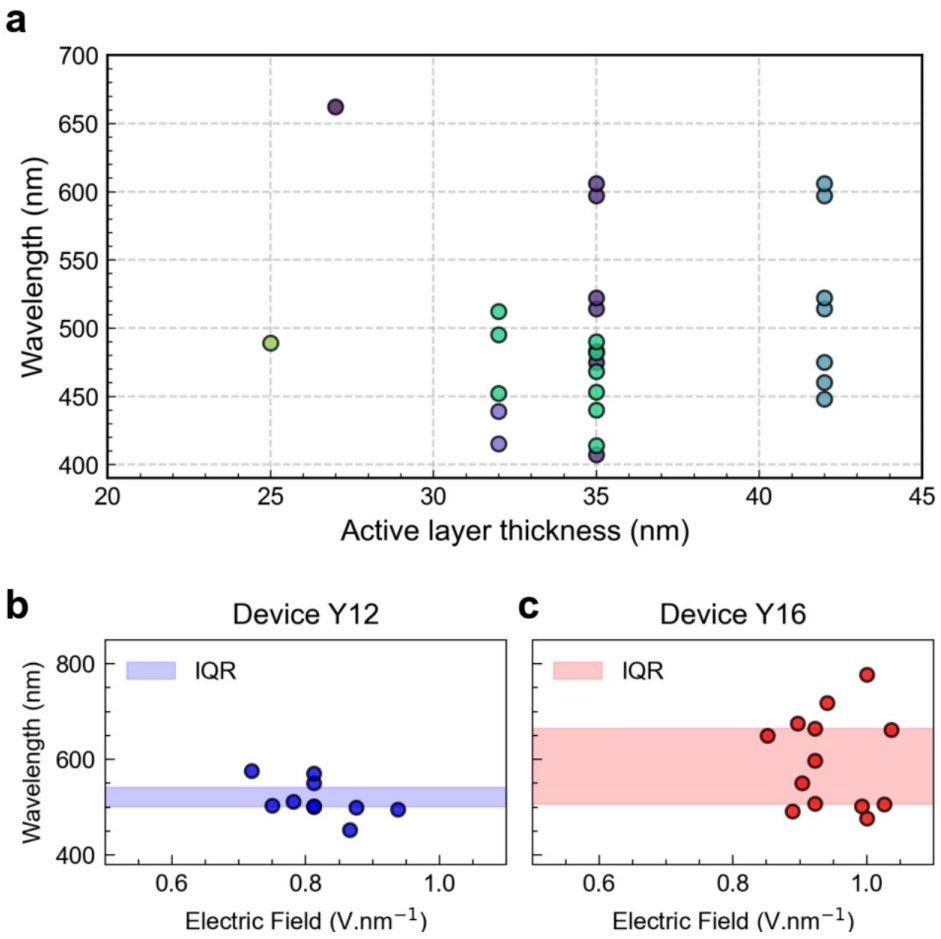


Figure 6.5: ***ZPL values of generated colour centres across multiple devices.*** ***(a)*** *ZPL wavelengths as a function of varying hBN active layer thickness. Each colour of the scattered plot corresponds to the same device.* ***(b)*** *and* ***(c)*** *ZPL wavelengths distribution as a function of applied electric field at which they were first observed, acquired from two different devices.*

tons through electronic transitions. As the electric field increases, the narrowband emission remains spectrally distinct, while the thermal emission becomes increasingly dominant in intensity. These observations emphasise the presence of two entirely different mechanisms contributing to the emission spectra within the tunnelling region of a device. It is important to consider the broad emission as it contributes a significant number of counts to the spectrum, particularly at high electric fields. This introduces challenges when performing measurements on single colour centres, such that an appropriate electric field operating regime must be carefully determined to minimise contribution of the background emission while ensuring efficient excitation of colour centres, as depicted in Figure 6.6.

The two emission mechanisms are further investigated by analysing their dependencies

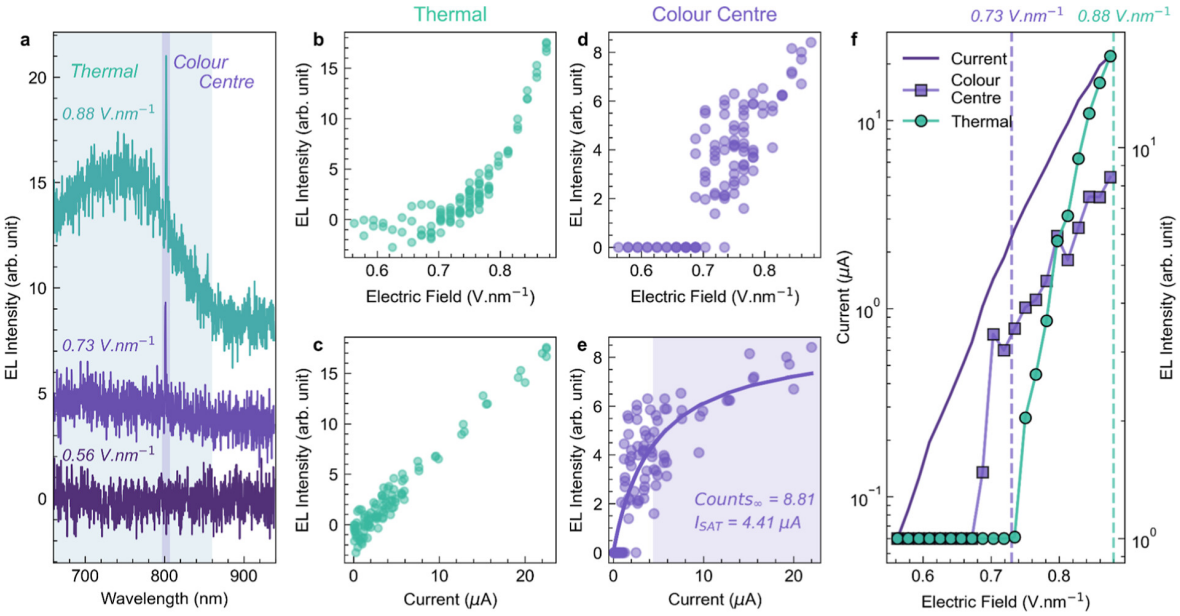


Figure 6.6: ***Thermal and electrically driven colour centre emissions.*** ***(a)*** *Three representative spectra taken at different electric field regimes; minimal field showing no emission, low field showing only colour centre EL, and high field showing both thermal and colour centre emissions. Thermal EL counts obtained from within the blue shaded region are plotted in* ***(b,c)*** *against the electric field and current, respectively. Colour centre EL counts obtained from double Lorentzian fits of the narrowband peak plotted in* ***(d,e)****, respectively. The blue shaded region in (e) highlights data points that are past the saturation current value.* ***(f)*** *Semilogarithmic plot of current and EL counts of both colour centre and thermal emissions against the applied electric field. Vertical dashed lines indicate the same electric fields at which representative spectra in (a) were acquired. Measurements conducted at 10 K.*

on the electric field and current, represented in Figure 6.6b-f. The broad thermal emission (green) exhibits a strong nonlinear increase in emission intensity as a function of applied electric field while having a more linear slope with applied current. In contrast, the narrowband colour centre emission (blue) shows a distinct saturation behaviour as a function of current that is characteristic of luminescent defects and is governed by the relationship $C = \frac{C_\infty I}{I+I_{SAT}}$ that yields a finite saturation luminescence counts value C_∞, where I and I_{SAT} represent tunnelling current prior and at saturation, respectively. This limit is imposed by the rate of change of the population of a ground energy state and the spontaneous decay of electrons from the excited state. The rate of spontaneous decay is dependent on the properties of the system that govern the lifetime of an electron in an excited state until it relaxes to the ground state via photon emission. The studied colour centre saturates at approximately 9 counts with 4.42 μA of tunnelling current flowing through the emissive hBN layer.

The semilogarithmic plot in Figure 6.6f summarises the interplay between these two mechanisms. As the current increases exponentially with the electric field, thermal emis-

sion is absent until $\sim$0.75 V.nm^{-1}, after which it begins to rapidly increase in counts and dominate emission spectrum contribution at fields above 0.8 V.nm^{-1}. Contrarily, the colour centre has a lower emission turn-on electric field, $\sim$0.68 V.nm^{-1}, and follows a smaller gradient slope. These observations further confirm that the two emission components arise from fundamentally different physical processes, with the broadband photons likely being due to thermal emission, while the colour centre luminescence is tied to quantum defect luminescence.

This work also investigated the dynamic response of colour centres and devices to applied electric fields. In these measurements, the electric field was varied over time while simultaneously recording the colour centre emission and tunnelling currents, as presented in Figure 6.7.

Figure 6.7a first examines the behaviour of a colour centre over time as the electric field changes. A colour centre was generated within the emissive hBN layer prior to the measurement by operating the device at 0.75 V.nm^{-1} for 10 min. The top panel shows the electric field variation over 14 min: starting at 0.69 V.nm^{-1}, increasing to 0.78 V.nm^{-1}, decreasing to 0.58 V.nm^{-1}, and increasing again to 0.88 V.nm^{-1}. The corresponding emission counts from the colour centre (bottom panel) exhibited a dynamic response to the applied electric field, revealing that no luminescence was observed below a threshold field value of 0.68 V.nm^{-1}. It is also demonstrated that the same colour centre was switched back into the luminescent state if the applied electric field was above the threshold value. However, at extreme electric fields, nearing 1 V.nm^{-1}, the colour centre would permanently switch off its luminescence. This behaviour is highlighted past the 13.5 min mark, when EL from this colour centre has disappeared.

Continuous increase of applied bias in the high-field regime typically resulted in permanent switching off of colour centres. Furthermore, extended operation of devices in a high-field regime also caused a similar effect, although it was often delayed. Thus, in addition to optimising operating conditions to minimise background contributions, it is also essential to map out safe electric field ranges to preserve colour centre emission. Figure 6.7b quantifies the time for which individual colour centres remained active at specific electric fields. Measurements repeated across multiple colour centres revealed that fields around 0.78 V.nm^{-1} rapidly quenched their emission. In contrast, reducing the electric field below 0.72 V.nm^{-1} allowed for a significantly prolonged operation. These optimised conditions achieved continuous electrical excitation of a single colour centre for up to 36 h.

To further investigate the dynamic response of devices to applied electric fields, tunnelling current was monitored over time as the electric field was varied. These measurements are depicted in Figure 6.7c-g. The tunnelling current exhibited a rapid response to changes in the applied electric field, adjusting instantaneously to a new set electric field.

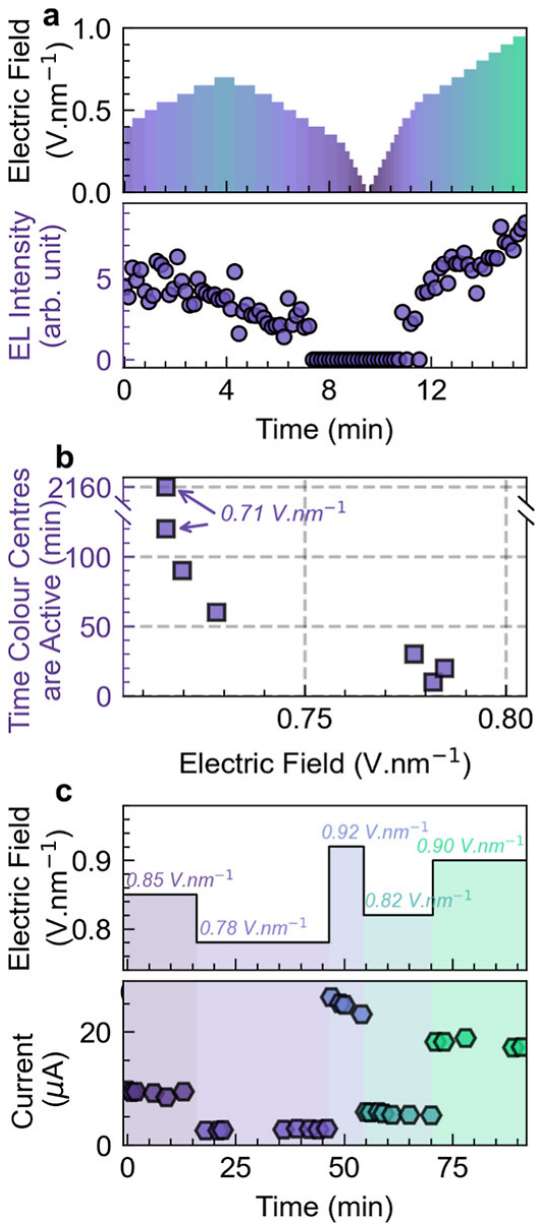


Figure 6.7: ***Device and colour centre time dynamics over varying electric fields.*** ***(a)*** *Time dynamics of EL from a colour centre at varying electric fields over time. Colour in the top panel corresponds to electric field strength.* ***(b)*** *Time dependence of colour centres continuously measured at specified electric fields.* ***(c)*** *Plots of tunnelling currents over time at varying applied electric fields during measurements of a device. Measurements conducted at 10 K.*

Application of a high electric field on hBN EL devices results in a multitude of physical changes of the emissive layer, which could be observed via tunnelling current behaviour. At high electric fields, tunnelling current would begin to drop, likely due to generation of charge traps. This is particularly noticeable at very high electric fields, above 0.9 V.nm^{-1}, where a severe current drop is observed within a time span of less than 10 min (Figure 6.7c). The effect also persists at slightly lower electric fields (>0.8 V.nm^{-1}) but with more gradual reduction in current. In contrast, electric fields below 0.8 V.nm^{-1} tend to maintain stable current values over time; in fact at 0.78 V.nm^{-1}, the current fluctuated around 2.7 μA for 28 min, demonstrating stable device operation under these conditions.

Last section of this chapter reports on observation of room temperature PL charge state control of an electrically generated colour centre under applied electric fields. While similar behaviour was observed from hBN colour centres [144, 146], this work demonstrates a correlation at room temperature. Figure 6.8 summarises the observed phenomena where a device hosting a colour centre with an emission energy of 432 nm demonstrated that, in PL measurements, applied electric fields varied the intensity of the colour centre and induced the appearance of an additional lower-energy peak within the 580-655 nm wavelength range. The intensity of this lower-energy peak exhibited dependence on the polarity of the applied electric field, with positive bias applied on the top graphene electrode enhancing the emission counts and negative bias reducing them. This effect was also observed, though with a lesser gradient, for the 432 nm peak. This is summarised in Figure 6.8b,c, where black points show mean intensity values at certain fields. Furthermore, the spectral position of the lower-energy peak was not fixed, shifting the ZPL transition within the 580-655 nm range. Interestingly, at sufficiently high positive bias (0.29 V.nm^{-1}), two distinct lower-energy peaks were observed alongside the persistent 432 nm peak. This behaviour could be attributed to an additional charge state present in the studied system [144, 146, 222].

6.3 | Summary

To summarise, engineered hBN EL devices were investigated for their ability to generate colour centres under applied electric fields. This was evident through I-V and time-resolved spectral and current analyses that showed formations of other non-luminescent defects, such as charge traps. This chapter highlighted the electric fields necessary for generation of visible to NIR wavelength range narrowband colour centres. Most importantly, this work determined the best conditions for operating tunnelling devices with minimised background and prolonged operation of both colour centres and devices. These findings conclude that generated colour centres are most optimally measured at electric field strengths

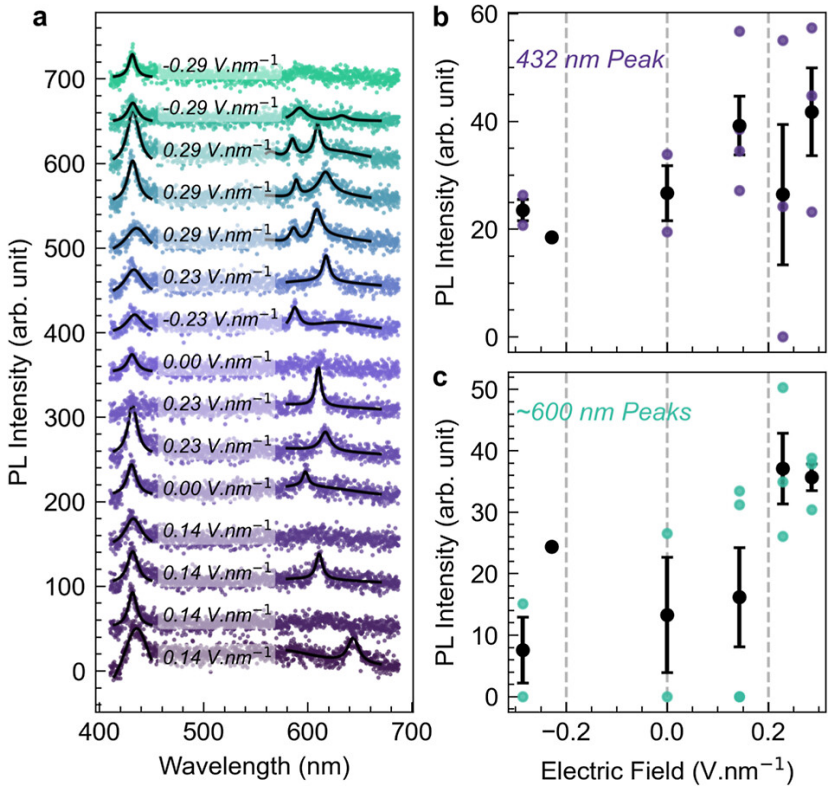


Figure 6.8: ***Room-temperature PL measurement of the colour centre under applied electric fields.*** ***(a)*** *Spectra of the colour centre acquired under varying applied electric fields.* ***(b)*** *Max intensity counts extracted from double Lorentzian fits of the peak at 420 nm.* ***(c)*** *Max intensity counts extracted from double Lorentzian fits of peaks around 600 nm. In cases where two peaks are observed, peaks with the highest intensity are recorded. Black points in (b,c) are average intensity values at corresponding electric fields. Error bars are calculated using standard error of the mean.*

in the range of 0.68-0.71 V.nm^{-1}. Within this range, the thermal background emission is absent, while colour centres and devices are stable on an hours-long time scale. Electrically generated colour centres also demonstrated room-temperature electrical control, an avenue for future research. This chapter advances the ongoing progress toward on-chip integration of quantum optoelectronic vdW systems based on hBN.

7

Conclusions & Outlook

This chapter summarises the key results and contributions of this thesis and places them within the broader context of quantum photonics research field. The main results are consolidated in thesis summary, highlighting advances in the electrical generation, excitation, and control of hBN quantum emitters. The chapter then outlines prospective research directions enabled by this work, focusing on electrically tunable and electrically driven quantum emitter systems as building blocks for future on-chip quantum technologies.

7.1 | Thesis Summary

This thesis explored generation, excitation, and control of hBN quantum emitters through their integration into novel vdW quantum optoelectronic heterostructures. By combining engineering of electrical devices based on 2D material building blocks with confocal spectroscopy, results presented here position hBN as a scalable solid-state platform for on-chip quantum photonic technologies.

A comprehensive theoretical and experimental framework was first established to define quantum light using coherence functions and intensity correlations. Distinction between classical and non-classical light was introduced through photon correlation measurements, providing key theoretical concepts and experimental metrics required to identify and benchmark single-photon emitters. These methods were subsequently employed throughout this thesis to characterise hBN emitters under both optical and electrical excitation.

Defect-based quantum emitters (colour centres in wide-bandgap materials) were reviewed as promising building blocks for emerging quantum technologies, positioning hBN as a particularly attractive host for quantum light sources. In contrast to bulk 3D materials, hBN supports bright, pure, and stable single-photon emission at room temperature, with emitters exhibiting high Debye–Waller factors and, crucially, compatibility with vdW het-

erostructure – an advantage leveraged throughout this thesis. Key challenges associated with hBN quantum emitters were addressed by introducing a novel method for emitter generation based on locally applied high electric fields within integrated devices. Device operating regimes were systematically analysed to enable controlled defect formation while preserving long-term electrical stability and minimising background emission. The generated emitters exhibited optical signatures consistent with established hBN colour centres, demonstrating a viable pathway towards on-chip generation of quantum emitters without the need for external irradiation or high-temperature annealing. Using this electrical generation approach, ZPL emission wavelengths typically fell within the 500-642 nm range. While precise deterministic control over ZPL energy remains an open challenge, methods described here showed emitter generation site-specifically (within graphene electrode slots). This highlights the scalability of this approach and already ensures direct integration into electrically tunable architectures.

This thesis then investigated electrical control of quantum emitters via the Stark effect. By integrating B-centres into specific vdW heterostructures, in-plane and out-of-plane electric fields were applied to probe the energy-level response of emitters. Resonant excitation spectroscopy was employed with results showing that out-of-plane electric fields produced weak energy shifts, while in-plane fields yielded a clear quadratic Stark response, with ZPL shifts reaching orders of magnitude larger than the natural linewidth. These are consistent with a centrosymmetric defect structure, supporting a split-interstitial model composed of either nitrogen or carbon atoms. Furthermore, these outline relevant field geometry for effective electrical tuning of the B-centre ZPL, establishing Stark control as a viable route for spectral alignment of emitter ZPL, a critical requirement for emitter-cavity coupling and multi-emitter interference.

A central result of this thesis is the demonstration of EL from hBN quantum emitters. Graphene-hBN-graphene heterostructures were fabricated and engineered to sustain extremely high electric fields, to enter a regime where quantum tunnelling prevails for charge injection of both electrons and holes into hBN layer. The resulting emitter EL was shown to be spectrally narrow, stable up to room temperature, polarised, and importantly of quantum origin, with emission characteristics closely matching those of optically excited hBN quantum emitters. This result represents a significant milestone, demonstrating an alternative route of electrical excitation of quantum emitters that bypasses conventional p–n or p–i–n junctions architectures by exploiting quantum tunnelling in novel materials, such as vdW heterostructures.

Taken together, the results presented in this thesis establish hBN as a versatile and promising material platform for quantum photonics. By demonstrating electrical generation, excitation, and control of its quantum emitters using novel vdW device architectures, this work

bridges a critical gap between fundamental emitter physics and practical quantum optoelectronic integration. The insights gained here lay the groundwork for future developments in electrically driven single-photon sources, tunable quantum emitters, and integrated vdW quantum photonic systems, with proposed future research directions described in the following section of this chapter.

7.2 | Outlook and Future Directions

Although the results of this thesis demonstrate substantial progress towards electrically generated, controlled, and excited quantum emitters in hBN, certain limitations are also revealed and must be addressed to realise practical quantum optoelectronic devices. Specifically, the current EL device performance remains limited in efficiency and brightness, with photon extraction being significantly lower compared to optically excited hBN emitters. Integration with photonic resonators, such as inverse patterned metasurfaces, presents an optimal route towards enhancing emission rates and collection efficiency. Furthermore, as shown in Chapter 6, operation at high electric fields introduces significant background emission, limiting single photon purity in this regime. And while device stability was shown to be robust over extended periods under optimised conditions, high-field operation required for emitter generation introduces charge traps and non-radiative defects, prematurely degrading the device. In addition, emission energies of electrically generated emitters remain stochastic, limiting control over ZPL wavelengths. These challenges could be addressed by optimising charge injection mechanisms through the use of alternative vdW electrode materials [216] or by incorporating electrical gates [223–226].

Nevertheless, this thesis showed that integrating quantum emitters into engineered electrical devices offers a powerful route for overcoming numerous limitations, including inhomogeneous emission wavelengths, linewidth broadening, inefficient photon emission, site-specific generation, and scalability. Electrical control enables additional functionalities, such as active wavelength tuning, charge-state manipulation, deterministic generation and excitation, while also providing a pathway towards fully on-chip operation. Ultimately, scalable quantum photonic technologies will require platforms in which generation, excitation, control, and detection of single photons are all achieved electrically within integrated photonic architectures. This motivates continued research into novel quantum optoelectronic devices that combine low-dimensional materials, such as vdW heterostructures, with solid-state quantum emitters. Results presented in this thesis advance in this path with future experimental directions outlined below.

7.2.0.1 | Electrical Control

Control of emission wavelength of a quantum source is a key enabling capability for scalable quantum photonic technologies. In solid-state systems, emitter-to-emitter variations in ZPL energies are unavoidable, even for nominally identical defects such as the hBN B-centre, due to local strain, charge fluctuations, and nearby defects in the host lattice. A direct next experimental step enabled by the results of this thesis is electrical tuning of individual B-centre emitters into resonance with nanophotonic optical cavities using in-plane electric fields. In practice, it is highly unlikely that a B-centre generated within a cavity will be naturally resonant with the cavity mode. Therefore, Stark effect tuning provides a practical route for achieving spectral alignment of the two. Cavity coupling would lead to enhanced photon extraction efficiency and controlled, directional routing of quantum light into on-chip photonic modes. A second promising direction involves electrical tuning of two spatially separated B-centres into mutual resonance, enabling entanglement of two distinct quantum systems via photon interference. Achieving electrically controlled emitter–emitter spectral alignment would represent a significant step towards multi-emitter quantum photonic circuits, distributed quantum networks, and scalable sources of entangled photons based on hBN.

Beyond spectral tuning, electrical fields offer access to additional degrees of freedom in emitter control. As shown in Chapter 6, electric fields can influence charge-state dynamics of hBN quantum emitters, leading to the emergence of multiple ZPL transitions at several well-spaced energies, while also enhancing their emission brightness. This behaviour opens the possibility of electrically programmable emission spectra from a single emitter, which could be exploited for multiplexed quantum light generation, wavelength-division quantum communication, or reconfigurable on-chip quantum light sources.

Electrical control also provides a pathway towards improving photon indistinguishability, a key requirement for quantum interference applications such as optical quantum computing and entanglement generation. Charge noise is one of the major sources of ZPL broadening in hBN emitters [100, 101]. Recent demonstrations using vdW heterostructure devices have shown that local charge noise can be suppressed leading to near lifetime-limited emission from visible hBN emitters [140]. Applying similar device engineering strategies to the B-centre is expected to reduce spectral diffusion and bring emission closer to its natural linewidth. This would enable two-photon interference experiments with substantially improved indistinguishability compared to earlier demonstrations [122], positioning the B-centre as a competitive candidate for qubit generation.

7.2.0.2 | Electrical Excitation

Electrical excitation of quantum emitters further advances towards fully integrated quantum optoelectronic devices. While this thesis has demonstrated electrically driven quantum emission from hBN emitters, an important future direction is the extension of electrical excitation schemes to quantum systems with access to spin.

In recent years, hBN has seen rapid progress within the community as a host of multiple classes of spin-active quantum emitters. These include spin-1 systems such as the VB^- centre [125], single spin-1 emitters in thin CVD hBN films[141, 169], and more recently spin-complex systems consisting of defect pairs that simultaneously exhibit both spin-1 and spin-1/2 transitions [227]. The latter are of particular interest as they have recently enabled optically detected nuclear magnetic resonance schemes, attracting significant attention due to their spin physics and potential applications in quantum storage [227]. Furthermore, similar defect signatures have been observed in other wide-bandgap materials, such as gallium nitride [88], highlighting the relevance of these systems across material platforms.

A natural next step is the investigation of spin readout under electrical excitation, enabling electrically driven optically detected magnetic resonance (EL-ODMR) in hBN. In such systems, qubit states are encoded in the spin sublevels of the defect ground state. These spin-dependent transitions can be coherently manipulated using microwave fields and electrically read out via current detection. Achieving spin-dependent EL would allow electrical spin initialisation, manipulation, and readout, while eliminating bulky external optical components. This opens the possibility of a quantum device architecture that combines site-specific emitter generation, excitation via tunnelling charge injection, and spin-state readout on a fully on-chip platform. Advancements in engineering of integrated quantum optoelectronic vdW heterostructure devices further bring solid-state emitters towards practical quantum technologies.

A

Stark Effect

This appendix provides theoretical background relevant to Chapter 4, where the response of quantum emitters to externally applied electric fields is investigated. In particular, it introduces the physical interpretation of the Stark effect in perspective of quantum emitters and outlines the mathematical framework used to interpret experimentally measured energy shifts.

A.1 | Theoretical Description

Stark effect describes the shift of an energy level in the presence of a static electric field. An electric field interacts with electric dipole and shifts its energy depending on how the dipole is oriented relative to the field. When the dipole aligns with the field, the system's energy is reduced. In a quantum system each energy orbital has a spatial distribution of electric charge set by its wavefunction. An applied electric field interacts with this charge distribution and modifies the energy of the state. Thus, optical transition energies (e.g., ZPL of an emitter) become field dependent.

Two distinct physical contributions arise. First, if an emitter has a permanent electric dipole moment along the field direction, the energy shifts linearly with field. This is a direct analogue of a compass needle in a magnetic field, where the permanent dipole interacts linearly at first order. Second, even if the permanent dipole is small or symmetry forbids it, an applied field can polarise the charge distribution, inducing an additional dipole proportional to the field. This induced response produces a quadratic energy shift and is quantified by the polarisability of the system. In solid-state quantum emitters, both effects can be present because crystal fields, strain, and local symmetry breaking can generate non-zero permanent dipoles and strong polarisabilities.

Experimentally, Stark effect is quantified by measuring optical transition energy at zero field and under various applied electric fields. Relevant result is therefore the difference of energy shifts between ground and excited states. This leads to a linear contribution proportional to the change in permanent dipole moment between the two states, and a quadratic contribution proportional to the change in their polarisability. These parameters provide insight into the electronic structure and local symmetry of the emitter. This is because a centrosymmetric defect has symmetric charge distribution compared to a non-centrosymmetric defect, thus Stark shift responses of the systems will be either mostly quadratic or linear, respectively.

An intuitive way to conceptualise this behaviour is by comparing an inversion symmetric system to one that already possesses a permanent electric dipole moment. In the former case, the permanent dipole moment μ is zero, however, an applied electric field F can induce a dipole whose magnitude will be governed by the system's polarisability α. In contrast, a system already with an intrinsic dipole moment μ will experience a direct first-order interaction with the applied field F. As a result, the electric-field-induced energy shift of a quantum system can be expressed as

$$\Delta E(F) = -\mu F - \frac{1}{2}\alpha F^2 \tag{A.1}$$

Since optical spectroscopy probes the energy difference between the excited and ground states of a quantum emitter, the Stark shift of an optical transition is given by the difference between their individual energy shifts. This modifies Eq. A.2 to

$$\Delta E(F) = -\Delta\mu_{perm} F - \frac{1}{2}\Delta\alpha F^2 \tag{A.2}$$

where $\Delta\mu_{perm}$ and $\Delta\alpha$ are the differences in permanent dipole moment and polarisability between the excited and ground states. To highlight, *the linear Stark term reflects an intrinsic asymmetry of the defect, while the quadratic term reflects how easily its electronic wavefunctions are distorted by an external electric field.*

B

Quantum Tunnelling

This appendix is particularly relevant to chapters 5 and 6. It provides a detailed discussion of charge injection mechanisms in monolayyer graphene-hBN devices, outlining the different tunnelling processes by which electrons and holes are injected from graphene into the hBN layer. Fowler-Nordheim tunnelling is compared with alternative mechanisms, trap-assisted tunnelling and Poole-Frenkel emission. Temperature dependent I-V measurements are presented to identify the dominant transport mechanism across different temperature regimes. In addition, the electrical characteristics of fabricated devices are compared prior and post emitter generation, revealing a reduction in the effective tunnelling barrier height, which is indicative of defect formation and creation of charge traps within hBN layer.

B.1 | Charge Injection Mechanisms

Electrical injection mechanism analysis begins with Figure B.1a, where charge carriers can be injected into hBN via Fowler-Nordheim tunnelling, trap-assisted tunnelling, and Poole-Frenkel emission [217].

Fowler-Nordheim tunnelling (FNT) describes field-induced tunnelling of charge carriers under a strong electric field. Applied bias bends the energy bands sufficiently to allow carriers to tunnel directly from graphene electrode into the conduction or valence band of hBN without the involvement of intermediate states. The resulting current exhibits a strong, non-linear dependence on the electric field and is typically dominant in high-quality, low-defect dielectrics at large fields, where direct tunnelling through the barrier is energetically favourable.

Trap-assisted tunnelling (TAT) occurs when defects or impurities within hBN bandgap introduce localised electronic states that facilitate multi-step tunnelling. Charge carriers can tunnel from the graphene electrode into a defect state and subsequently tunnel onward into

the hBN bands or nearby defect. This mechanism effectively lowers the apparent tunnelling barrier. TAT is strongly dependent on defect density and becomes increasingly significant in devices where structural imperfections or electrically generated defects are present.

Poole–Frenkel emission (PFE) is a thermally assisted transport mechanism in which charge carriers are emitted from trapped states into the conduction or valence band under an applied electric field. Applied electric field reduces Coulombic potential that confines trapped carriers, thus lowering the activation energy required for emission. PFE exhibits a pronounced temperature dependence and is typically observed at elevated temperatures, under moderate electric fields and in materials with high density of charged traps.

For high-quality hBN and in high electric field, FNT applies, in which case I-V characteristics are dominated by tunnelling current of holes in the heterostructures of graphene-hBN-graphene. This is because tunnelling barrier for holes is smaller than for electrons [203, 204]. Figure B.1b shows I-V characteristics of a representative Device 1 that used carbon-doped hBN (hBN:C) and displays rapid current increase beyond 10 V. Figure B.1c compares tunnel barrier heights for four hBN:C devices (including Device 1 from Figure B.1b) to a pristine hBN device. Compared to pristine hBN (high quality hBN) device, Device 1 in Figure B.1c shows slightly smaller barrier height. This is caused by the high density of defects present in hBN:C layer, which effectively reduce tunnelling barrier height, as schematically shown in Figure B.1a. Although most commonly observed I-V characteristics are of Device 1 and Device 2 in Figure B.1c, however, it is also possible to record I-V characteristics of Device 3 and Device 4 with significantly lower barrier heights, indicating an even higher density of defects.

As discussed earlier, in the case of FNT, I-V characteristics are independent of temperature [205]. Therefore, it is possible to simulate I-V curve using the Fowler-Nordheim formula. The current relationship can be described via B.1. A linear relationship between $ln(I/V^2)$ and $1/V$ is observed when equation B.1 is further formulated into equation B.2). Both expressions include constants applicable to an hBN based devices, where I is tunnelling current, V is bias voltage, A_{eff} is the effective tunnelling area, q is elementary charge, m is free electron mass, Φ_B is tunnelling barrier height for charge carriers at the electrode and the insulator interface, h is the Planck's constant, and m^* is the effective mass of charge carriers in the insulator.

$$I = \frac{A_{\text{eff}} q^3 m V^2}{8\pi h \Phi_B m^* d^2} \cdot \exp\left[-\frac{8\pi\sqrt{2m^*}\,\Phi_B^{3/2} d}{3hqV}\right] \tag{B.1}$$

$$\ln\left(\frac{I}{V^2}\right) = \ln\left(\frac{A_{\text{eff}} q^3 m}{8\pi h \Phi_B m^* d^2}\right) - \frac{8\pi\sqrt{2m^*}\Phi_B^{3/2} d}{3hq} \cdot \frac{1}{V} \tag{B.2}$$

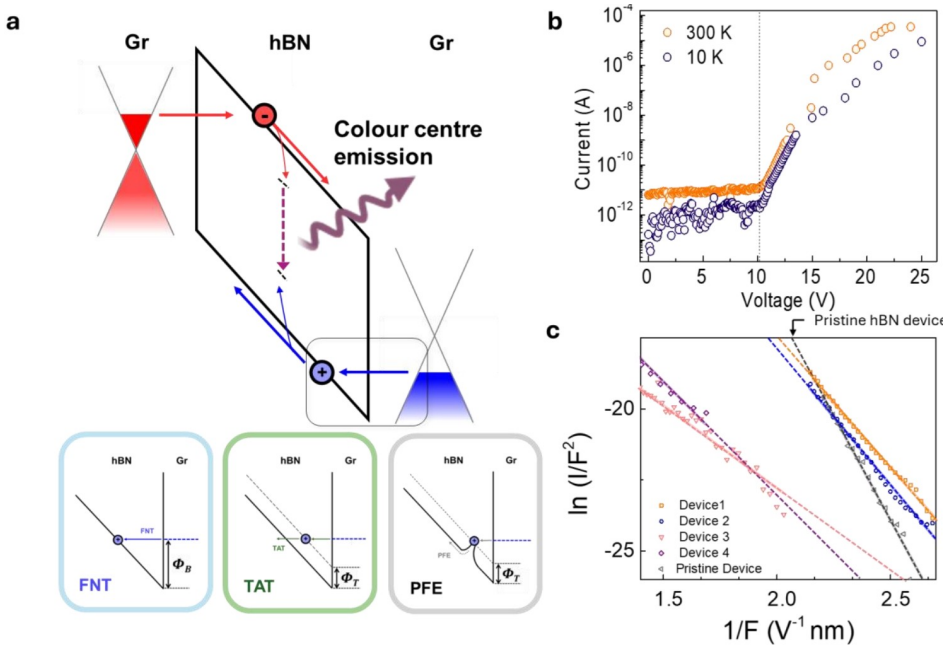


Figure B.1: ***Electrical characteristics at the interface of graphene and hBN.*** ***(a)*** *Schematics of carrier injections via field mission processes.* ***(b)*** *Temperature dependence of I-V characteristics of hBN:C Device 1.* ***(c)*** *Fowler-Nordheim plot of I-V characteristics for various devices.*

Having defined Fowler-Nordheim model, continue onto simulation of the I-V characteristic of fabricated devices. Figure B.2 compares experimental I-V (a,b) and simulated I-V (c,d) of pristine hBN and hBN:C, respectively. The simulated curve in Figure B.2c produces results consistent with those observed in pristine hBN device (Figure B.2a), yielding an experimental barrier height (Φ_B) of approximately 1.8 eV.

Moving on to hBN:C device, where I-V characteristics are strongly affected by the presence of defects at higher temperatures. In Figure B.2b, fabricated device exhibits systematic current increase as temperature increases. This behaviour can be explained by PFE through defects as schematically illustrated in the inset of Figure B.2d. In the PFE mechanism, tunnel-injected charge carriers to defects can be thermally excited and drifted under applied electric field. Thus, defect barrier height is estimated to be ~ 1 eV via the Arrhenius plot (Figure B.3). Based on the PFE model, simulation of I-V characteristics of the device (Figure B.2d) shows a good agreement with the experimental data (Figure B.2b) [218]. Although hole injection is assumed for the simplicity in the analysis, deep-level defects can also assist tunnel injection of electrons which is of interest for the future research. Additionally, it is important to note that high voltage operation for prolonged periods of time can significantly alter I-V characteristics as shown in chapter 6 and discussed further in this appendix.

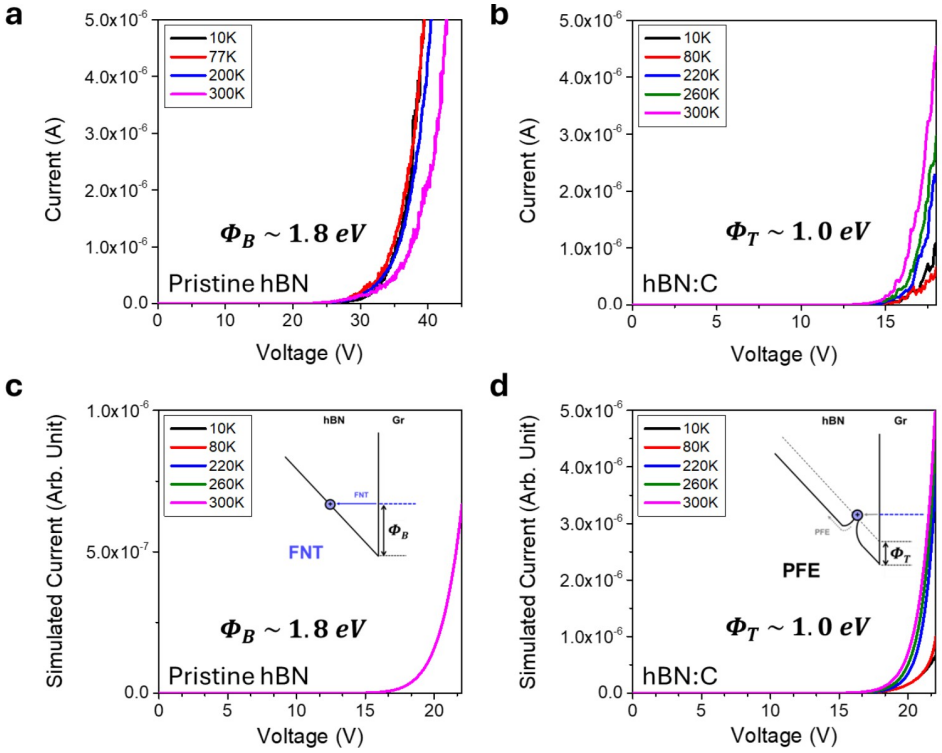


Figure B.2: ***Temperature dependence of electrical characteristics at the interface of graphene and hBN.*** ***(a)***, ***(b)*** *Experimental temperature dependence of I-V characteristics of pristine hBN device and hBN:C device respectively.* ***(c)***, ***(d)*** *Simulated I-V characteristics of pristine hBN and hBN:C respectively.*

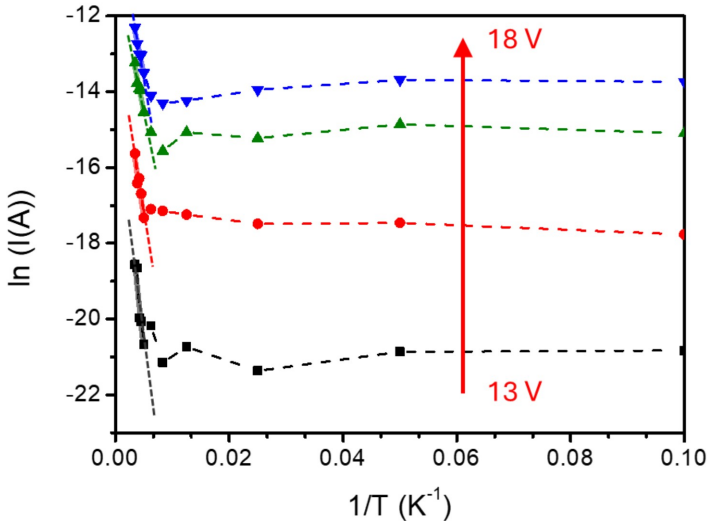


Figure B.3: ***Temperature dependent tunnelling mechanism analysis of Device 1.*** *Arrhenius plots at an applied voltage of 13 V to 18 V from 10 K to 290 K.*

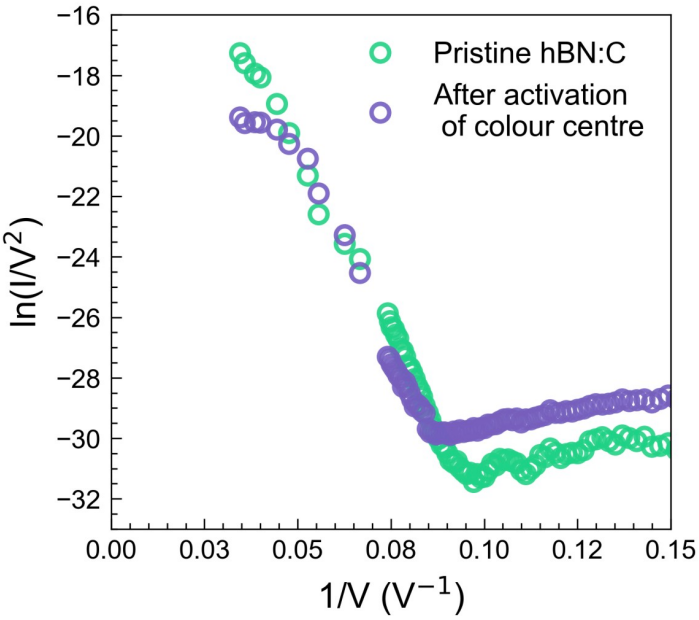


Figure B.4: ***Fowler-Nordheim plot corresponding to the I-V characteristics of hBN heterostructure device for electrical generation and excitation of emitters.*** *After generating hBN colour centres, tunnelling current (blue dots) shows a change compared to a newly fabricated unmeasured device (green dots).*

B.2 | Electrical Characterisation of Emitter Generation

Electrical properties, in particular I-V measurements were conducted on devices prior and post any optical measurements. Field emission model is employed to analyse characteristics of fabricated devices. Based on the results of the previous studies where the same heterostructure was used [151, 189, 203, 204], Fowler-Nordheim tunnelling [205] was considered the dominant mechanism at low impurity densities. Figure B.4 represents a Fowler-Nordheim plot based on I-V characteristics a heterostructure device engineered for electrical generation and excitation of hBN emitters.

Here, the data shows a clear linear relationship when the Fowler-Nordheim plot is applied. Notably, this relationship persists both prior and post optical measurement, with the device retaining I-V characteristics similar to pristine state. This indicates that the device continues to operate consistently despite the formation of observable defects. Furthermore, while FNT remains the dominant mechanism, a slight reduction in barrier height is observed, indirectly indicating the additional formation of defects as we have also confirmed through optical measurements in Chapters 5 and 6.

Bibliography

[1] Nicolas Gisin and Rob Thew. "Quantum communication". en. In: *Nature Photonics* 1.3 (Mar. 2007), pp. 165–171. ISSN: 1749-4885, 1749-4893.

[2] H. J. Kimble. "The quantum internet". en. In: *Nature* 453.7198 (2008), pp. 1023–1030. ISSN: 0028-0836, 1476-4687.

[3] Jeremy L. O'Brien, Akira Furusawa, and Jelena Vučković. "Photonic quantum technologies". en. In: *Nature Photonics* 3.12 (Dec. 2009), pp. 687–695. ISSN: 1749-4885, 1749-4893.

[4] W. B. Gao et al. "Coherent manipulation, measurement and entanglement of individual solid-state spins using optical fields". en. In: *Nature Photonics* 9.6 (2015), pp. 363–373. ISSN: 1749-4885, 1749-4893.

[5] Gary Wolfowicz et al. "Quantum guidelines for solid-state spin defects". en. In: *Nature Reviews Materials* 6.10 (Apr. 2021), pp. 906–925. ISSN: 2058-8437.

[6] Stefania Castelletto and Alberto Boretti. "Perspective on Solid-State Single-Photon Sources in the Infrared for Quantum Technology". en. In: *Advanced Quantum Technologies* 6.10 (Oct. 2023), p. 2300145. ISSN: 2511-9044, 2511-9044.

[7] David D. Awschalom et al. "Quantum technologies with optically interfaced solid-state spins". en. In: *Nature Photonics* 12.9 (2018), pp. 516–527. ISSN: 1749-4885, 1749-4893.

[8] Hong-Hua Fang et al. "Quantum sensing with optically accessible spin defects in van der Waals layered materials". en. In: *Light: Science Applications* 13.1 (Nov. 2024), p. 303. ISSN: 2047-7538.

[9] Mete Atatüre et al. "Material platforms for spin-based photonic quantum technologies". In: *Nature Reviews Materials* 3.5 (Apr. 2018), pp. 38–51. ISSN: 2058-8437.

[10] T. D. Ladd et al. "Quantum computers". en. In: *Nature* 464.7285 (Mar. 2010), pp. 45–53. ISSN: 0028-0836, 1476-4687.

[11] Nicolas Maring et al. "A versatile single-photon-based quantum computing platform". en. In: *Nature Photonics* 18.6 (2024), pp. 603–609. ISSN: 1749-4885, 1749-4893.

[12] Christophe Couteau et al. "Applications of single photons to quantum communication and computing". en. In: *Nature Reviews Physics* 5.6 (May 2023), pp. 326–338. ISSN: 2522-5820.

[13] PsiQuantum team et al. "A manufacturable platform for photonic quantum computing". en. In: *Nature* 641.8064 (May 2025), pp. 876–883. ISSN: 0028-0836, 1476-4687.

[14] H. Aghaee Rad et al. "Scaling and networking a modular photonic quantum computer". en. In: *Nature* 638.8052 (Feb. 2025), pp. 912–919. ISSN: 0028-0836, 1476-4687.

[15] Google Quantum AI et al. "Quantum error correction below the surface code threshold". en. In: *Nature* 638.8052 (Feb. 2025), pp. 920–926. ISSN: 0028-0836, 1476-4687.

[16] Sergey Bravyi et al. "High-threshold and low-overhead fault-tolerant quantum memory". en. In: *Nature* 627.8005 (Mar. 2024), pp. 778–782. ISSN: 0028-0836, 1476-4687.

[17] Microsoft Azure Quantum et al. "Interferometric single-shot parity measurement in InAs–Al hybrid devices". en. In: *Nature* 638.8051 (Feb. 2025), pp. 651–655. ISSN: 0028-0836, 1476-4687.

[18] Charles H. Bennett and Gilles Brassard. "Quantum cryptography: Public key distribution and coin tossing". en. In: *Theoretical Computer Science* 560 (Dec. 2014), pp. 7–11. ISSN: 03043975.

[19] Haoran Zhang et al. “Towards global quantum key distribution”. en. In: *Nature Reviews Electrical Engineering* 2.12 (Nov. 2025), pp. 806–818. ISSN: 2948-1201.

[20] M. K. Bhaskar et al. “Experimental demonstration of memory-enhanced quantum communication”. en. In: *Nature* 580.7801 (Apr. 2020), pp. 60–64. ISSN: 0028-0836, 1476-4687.

[21] M. Pompili et al. “Realization of a multinode quantum network of remote solid-state qubits”. en. In: *Science* 372.6539 (Apr. 2021), pp. 259–264. ISSN: 0036-8075, 1095-9203.

[22] N. Kalb et al. “Entanglement distillation between solid-state quantum network nodes”. en. In: *Science* 356.6341 (2017), pp. 928–932. ISSN: 0036-8075, 1095-9203.

[23] S. L. N. Hermans et al. “Qubit teleportation between non-neighbouring nodes in a quantum network”. en. In: *Nature* 605.7911 (May 2022), pp. 663–668. ISSN: 0028-0836, 1476-4687.

[24] J. R. Maze et al. “Nanoscale magnetic sensing with an individual electronic spin in diamond”. en. In: *Nature* 455.7213 (Oct. 2008), pp. 644–647. ISSN: 0028-0836, 1476-4687.

[25] M. Block et al. “Optically Enhanced Electric Field Sensing Using Nitrogen-Vacancy Ensembles”. en. In: *Physical Review Applied* 16.2 (Aug. 2021), p. 024024. ISSN: 2331-7019.

[26] Ziwei Qiu et al. “Nanoscale electric field imaging with an ambient scanning quantum sensor microscope”. en. In: *npj Quantum Information* 8.1 (Sept. 2022), p. 107. ISSN: 2056-6387.

[27] D. J. McCloskey et al. “A diamond voltage imaging microscope”. en. In: *Nature Photonics* (2022). ISSN: 1749-4885, 1749-4893.

[28] Jean-Philippe Tetienne et al. “Quantum imaging of current flow in graphene”. en. In: *Science Advances* 3.4 (Apr. 2017), e1602429. ISSN: 2375-2548.

[29] A. J. Healey et al. “Quantum microscopy with van der Waals heterostructures”. en. In: *Nature Physics* 19.1 (Jan. 2023), pp. 87–91. ISSN: 1745-2473, 1745-2481.

[30] Andreas Gottscholl et al. “Spin defects in hBN as promising temperature, pressure and magnetic field quantum sensors”. en. In: *Nature Communications* 12.1 (2021), p. 4480. ISSN: 2041-1723.

[31] H. Kraus et al. “Magnetic field and temperature sensing with atomic-scale spin defects in silicon carbide”. en. In: *Scientific Reports* 4.1 (2014), p. 5303. ISSN: 2045-2322.

[32] Qnami. *NV Magnetometry*. White Paper. Release date: 03 July 2020. Hofackerstrasse 40B, 4132 Muttenz, Switzerland: Qnami AG, 2020.

[33] Max Planck. “Ueber das Gesetz der Energieverteilung im Normalspectrum”. en. In: *Annalen der Physik* 309.3 (Jan. 1900), pp. 553–563. ISSN: 0003-3804, 1521-3889.

[34] A. Einstein. “Über einen die Erzeugung und Verwandlung des Lichtes betreffenden heuristischen Gesichtspunkt”. en. In: *Annalen der Physik* 322.6 (Jan. 1905), pp. 132–148. ISSN: 0003-3804, 1521-3889.

[35] Richard P. Feynman. *QED: The Strange Theory of Light and Matter*. Princeton, NJ: Princeton University Press, 1985.

[36] Mark Fox. *Quantum optics: an introduction*. en. Oxford master series in physics. Oxford: Oxford University Press, 2006. ISBN: 978-0-19-856672-4.

[37] Roy J. Glauber. “The Quantum Theory of Optical Coherence”. en. In: *Physical Review* 130.6 (June 1963), pp. 2529–2539. ISSN: 0031-899X.

[38] L. Mandel and E. Wolf. “Coherence Properties of Optical Fields”. en. In: *Reviews of Modern Physics* 37.2 (Apr. 1965), pp. 231–287. ISSN: 0034-6861.

[39] R. H. Brown and R. Q. Twiss. “A New Type of Interferometer for Use in Radio Astronomy”. In: *The London, Edinburgh, and Dublin Philosophical Magazine and Journal of Science* 45.366 (July 1954), pp. 663–682.

[40] H. J. Kimble, M. Dagenais, and L. Mandel. “Photon Antibunching in Resonance Fluorescence”. en. In: *Physical Review Letters* 39.11 (Sept. 1977), pp. 691–695. ISSN: 0031-9007.

[41] J. Beugnon et al. “Quantum interference between two single photons emitted by independently trapped atoms”. en. In: *Nature* 440.7085 (Apr. 2006), pp. 779–782. ISSN: 0028-0836, 1476-4687.

[42] Frank Diedrich and Herbert Walther. “Nonclassical radiation of a single stored ion”. en. In: *Physical Review Letters* 58.3 (Jan. 1987), pp. 203–206. ISSN: 0031-9007.

[43] Pengfei Wang et al. “Single ion qubit with estimated coherence time exceeding one hour”. en. In: *Nature Communications* 12.1 (Jan. 2021), p. 233. ISSN: 2041-1723.

[44] P. Michler et al. “Quantum correlation among photons from a single quantum dot at room temperature”. en. In: *Nature* 406.6799 (Aug. 2000), pp. 968–970. ISSN: 0028-0836, 1476-4687.

[45] N. Somaschi et al. “Near-optimal single-photon sources in the solid state”. en. In: *Nature Photonics* 10.5 (May 2016), pp. 340–345. ISSN: 1749-4885, 1749-4893.

[46] John C. Howell et al. “Realization of the Einstein-Podolsky-Rosen Paradox Using Momentum- and Position-Entangled Photons from Spontaneous Parametric Down Conversion”. en. In: *Physical Review Letters* 92.21 (May 2004), p. 210403. ISSN: 0031-9007, 1079-7114.

[47] M.J. Collins et al. “Integrated spatial multiplexing of heralded single-photon sources”. en. In: *Nature Communications* 4.1 (Oct. 2013), p. 2582. ISSN: 2041-1723.

[48] Noel H. Wan et al. “Large-scale integration of artificial atoms in hybrid photonic circuits”. en. In: *Nature* 583.7815 (2020), pp. 226–231. ISSN: 0028-0836, 1476-4687.

[49] Linsen Li et al. “Heterogeneous integration of spin–photon interfaces with a CMOS platform”. en. In: *Nature* 630.8015 (2024), pp. 70–76. ISSN: 0028-0836, 1476-4687.

[50] C. M. Knaut et al. “Entanglement of nanophotonic quantum memory nodes in a telecom network”. en. In: *Nature* 629.8012 (May 2024), pp. 573–578. ISSN: 0028-0836, 1476-4687.

[51] Michael Dobinson et al. “Electrically triggered spin–photon devices in silicon”. en. In: *Nature Photonics* 19.10 (Oct. 2025), pp. 1132–1137. ISSN: 1749-4885, 1749-4893.

[52] Gary Wolfowicz et al. “Vanadium spin qubits as telecom quantum emitters in silicon carbide”. en. In: *Science Advances* 6.18 (May 2020), eaaz1192. ISSN: 2375-2548.

[53] Igor A. Khramtsov and Dmitry Yu. Fedyanin. “Single-Photon Sources Based on Novel Color Centers in Silicon Carbide P–I–N Diodes: Combining Theory and Experiment”. en. In: *Nano-Micro Letters* 13.1 (Dec. 2021), p. 83. ISSN: 2311-6706, 2150-5551.

[54] Khashayar Khazen and Hans Jurgen Von Bardeleben. “NV-centers in SiC: A solution for quantum computing technology?” en. In: *Frontiers in Quantum Science and Technology* 2 (Jan. 2023), p. 1115039. ISSN: 2813-2181.

[55] Sridhar Majety et al. “Wafer-scale integration of freestanding photonic devices with color centers in silicon carbide”. en. In: *npj Nanophotonics* 2.1 (Jan. 2025), p. 3. ISSN: 2948-216X.

[56] Pascale Senellart, Glenn Solomon, and Andrew White. “High-performance semiconductor quantum-dot single-photon sources”. en. In: *Nature Nanotechnology* 12.11 (Nov. 2017), pp. 1026–1039. ISSN: 1748-3387, 1748-3395.

[57] Wei Luo et al. “Recent progress in quantum photonic chips for quantum communication and internet”. en. In: *Light: Science Applications* 12.1 (2023), p. 175. ISSN: 2047-7538.

[58] Xudong Wang et al. “Large-scale quantum dot–lithium niobate hybrid integrated photonic circuits enabling on-chip quantum networking”. en. In: *Nature Materials* 24.12 (Dec. 2025), pp. 1898–1905. ISSN: 1476-1122, 1476-4660.

[59] Liang Zhai et al. “Quantum interference of identical photons from remote GaAs quantum dots”. en. In: *Nature Nanotechnology* 17.8 (Aug. 2022), pp. 829–833. ISSN: 1748-3387, 1748-3395.

[60] Ł. Dusanowski et al. “Single photon emission up to liquid nitrogen temperature from charged excitons confined in GaAs-based epitaxial nanostructures”. en. In: *Applied Physics Letters* 106.23 (2015), p. 233107. ISSN: 0003-6951, 1077-3118.

[61] Yi Yang et al. “High-Purity Single-Photon Emission in Near-Infrared InAs Colloidal Quantum Dots with Strong Exciton Confinement”. en. In: *Nano Letters* 25.18 (May 2025), pp. 7595–7602. ISSN: 1530-6984, 1530-6992.

[62] S. L. Bayliss et al. “Optically addressable molecular spins for quantum information processing”. en. In: *Science* 370.6522 (Dec. 2020), pp. 1309–1312. ISSN: 0036-8075, 1095-9203.

[63] Sofia Pazzagli et al. “Self-Assembled Nanocrystals of Polycyclic Aromatic Hydrocarbons Show Photostable Single-Photon Emission”. en. In: *ACS Nano* 12.5 (May 2018), pp. 4295–4303. ISSN: 1936-0851, 1936-086X.

[64] Daniel W. Laorenza and Danna E. Freedman. “Could the Quantum Internet Be Comprised of Molecular Spins with Tunable Optical Interfaces?” en. In: *Journal of the American Chemical Society* 144.48 (Dec. 2022), pp. 21810–21825. ISSN: 0002-7863, 1520-5126.

[65] Yu-Ming He et al. “Single quantum emitters in monolayer semiconductors”. en. In: *Nature Nanotechnology* 10.6 (2015), pp. 497–502. ISSN: 1748-3387, 1748-3395.

[66] M. Koperski et al. “Single photon emitters in exfoliated WSe2 structures”. en. In: *Nature Nanotechnology* 10.6 (2015), pp. 503–506. ISSN: 1748-3387, 1748-3395.

[67] Alejandro R.-P. Montblanch et al. “Layered materials as a platform for quantum technologies”. en. In: *Nature Nanotechnology* 18.6 (June 2023), pp. 555–571. ISSN: 1748-3387, 1748-3395.

[68] Steffen Michaelis de Vasconcellos et al. “Single-Photon Emitters in Layered Van der Waals Materials”. en. In: *physica status solidi (b)* 259.4 (Apr. 2022), p. 2100566. ISSN: 0370-1972, 1521-3951.

[69] Moses B Gaither-Ganim et al. “Organic molecule single-photon sources”. en. In: *Oxford Open Materials Science* 3.1 (Jan. 2023), itac017. ISSN: 2633-6979.

[70] Tim Schröder et al. “How Blinking Affects Photon Correlations in Multichromophoric Nanoparticles”. en. In: *ACS Nano* 15.11 (Nov. 2021), pp. 18037–18047. ISSN: 1936-0851, 1936-086X.

[71] Chao Zhang et al. “Spontaneous Parametric Down-Conversion Sources for Multiphoton Experiments”. en. In: *Advanced Quantum Technologies* 4.5 (May 2021), p. 2000132. ISSN: 2511-9044, 2511-9044.

[72] Igor Aharonovich, Dirk Englund, and Milos Toth. "Solid-state single-photon emitters". en. In: *Nature Photonics* 10.10 (Oct. 2016), pp. 631–641. ISSN: 1749-4885, 1749-4893.

[73] Marcus W. Doherty et al. "The nitrogen-vacancy colour centre in diamond". en. In: *Physics Reports* 528.1 (2013), pp. 1–45. ISSN: 03701573.

[74] Junyi Lee et al. "Integrated single photon emitters". en. In: *AVS Quantum Science* 2.3 (Oct. 2020), p. 031701. ISSN: 2639-0213.

[75] Carlo Bradac et al. "Quantum nanophotonics with group IV defects in diamond". en. In: *Nature Communications* 10.1 (Dec. 2019), p. 5625. ISSN: 2041-1723.

[76] Prasoon K. Shandilya et al. "Optomechanical interface between telecom photons and spin quantum memory". en. In: *Nature Physics* 17.12 (Dec. 2021), pp. 1420–1425. ISSN: 1745-2473, 1745-2481.

[77] Yinhui Kan et al. "Ångström-tunable polarization-resolved solid-state photon sources". en. In: *Nature Photonics* 19.9 (2025), pp. 960–967. ISSN: 1749-4885, 1749-4893.

[78] Nils Becker and Elke Neu. "The Silicon Vacancy Center in Diamond". In: *Semiconductors and Semimetals*. Vol. 103. Elsevier, 2020, pp. 201–235.

[79] P.-J. Stas et al. "Robust multi-qubit quantum network node with integrated error detection". en. In: *Science* 378.6619 (Nov. 2022), pp. 557–560. ISSN: 0036-8075, 1095-9203.

[80] Eric Bersin et al. "Telecom Networking with a Diamond Quantum Memory". en. In: *PRX Quantum* 5.1 (Jan. 2024), p. 010303. ISSN: 2691-3399.

[81] Stephanie Simmons. "Scalable Fault-Tolerant Quantum Technologies with Silicon Color Centers". en. In: *PRX Quantum* 5.1 (Mar. 2024), p. 010102. ISSN: 2691-3399.

[82] W. Redjem et al. "All-silicon quantum light source by embedding an atomic emissive center in a nanophotonic cavity". en. In: *Nature Communications* 14.1 (2023), p. 3321. ISSN: 2041-1723.

[83] Alessandro Buzzi et al. “Spectral tuning and nanoscale localization of single color centers in silicon via controllable strain”. en. In: *Nature Communications* 16.1 (Oct. 2025), p. 8829. ISSN: 2041-1723.

[84] Yu Zhou et al. “Silicon carbide: A promising platform for scalable quantum networks”. en. In: *Applied Physics Reviews* 12.3 (2025), p. 031301. ISSN: 1931-9401.

[85] Fei-Fei Yan et al. “Room-temperature coherent control of implanted defect spins in silicon carbide”. en. In: *npj Quantum Information* 6.1 (May 2020), p. 38. ISSN: 2056-6387.

[86] Max Meunier et al. “Telecom single-photon emitters in GaN operating at room temperature: embedment into bullseye antennas”. en. In: *Nanophotonics* 12.8 (Apr. 2023), pp. 1405–1419. ISSN: 2192-8606, 2192-8614.

[87] Yu Zhou et al. “Room temperature solid-state quantum emitters in the telecom range”. en. In: *Science Advances* 4.3 (Mar. 2018), eaar3580. ISSN: 2375-2548.

[88] Jialun Luo et al. “Room temperature optically detected magnetic resonance of single spins in GaN”. en. In: *Nature Materials* 23 (Feb. 2024), pp. 512–518. ISSN: 1476-1122, 1476-4660.

[89] Alexander Senichev et al. “Room-temperature single-photon emitters in silicon nitride”. en. In: *SCIENCE ADVANCES* (2021).

[90] Toan Trong Tran et al. “Robust Multicolor Single Photon Emission from Point Defects in Hexagonal Boron Nitride”. en. In: *ACS Nano* 10.8 (Aug. 2016), pp. 7331–7338. ISSN: 1936-0851, 1936-086X.

[91] Gabriele Grosso et al. “Tunable and high-purity room temperature single-photon emission from atomic defects in hexagonal boron nitride”. en. In: *Nature Communications* 8.1 (2017), p. 705. ISSN: 2041-1723.

[92] L. J. Martínez et al. “Efficient single photon emission from a high-purity hexagonal boron nitride crystal”. en. In: *Physical Review B* 94.12 (2016), p. 121405. ISSN: 2469-9950, 2469-9969.

[93] Mads K. Boll et al. “Photophysics of quantum emitters in hexagonal boron-nitride nano-flakes”. en. In: *Optics Express* 28.5 (Mar. 2020), p. 7475. ISSN: 1094-4087.

[94] Leyi Loh et al. "Towards quantum light-emitting devices based on van der Waals materials". en. In: *Nature Reviews Electrical Engineering* 1.12 (Oct. 2024), pp. 815–829. ISSN: 2948-1201.

[95] Seokho Moon et al. "Hexagonal Boron Nitride for Next-Generation Photonics and Electronics". en. In: *Advanced Materials* 35.4 (Jan. 2023), p. 2204161. ISSN: 0935-9648, 1521-4095.

[96] Lee C. Bassett et al. "Quantum defects by design". en. In: *Nanophotonics* 8.11 (Nov. 2019), pp. 1867–1888. ISSN: 2192-8614, 2192-8606.

[97] E. U. Condon. "A Theory of Intensity Distribution in Band Systems". In: *Phys. Rev.* 28 (1926), pp. 1182–1201.

[98] B.A. McCullian et al. "Quantifying the Spectral Diffusion of N- V Centers by Symmetry". en. In: *Physical Review Applied* 18.6 (Dec. 2022), p. 064011. ISSN: 2331-7019.

[99] Toan Trong Tran et al. "Resonant Excitation of Quantum Emitters in Hexagonal Boron Nitride". en. In: *ACS Photonics* 5.2 (Feb. 2018), pp. 295–300. ISSN: 2330-4022, 2330-4022.

[100] Boris Spokoyny et al. "Effect of Spectral Diffusion on the Coherence Properties of a Single Quantum Emitter in Hexagonal Boron Nitride". en. In: *The Journal of Physical Chemistry Letters* 11.4 (Feb. 2020), pp. 1330–1335. ISSN: 1948-7185, 1948-7185.

[101] Simon White et al. "Phonon dephasing and spectral diffusion of quantum emitters in hexagonal boron nitride". en. In: *Optica* 8.9 (2021), p. 1153. ISSN: 2334-2536.

[102] Martin Esmann, Stephen C. Wein, and Carlos Antón-Solanas. "Solid-State Single-Photon Sources: Recent Advances for Novel Quantum Materials". en. In: *Advanced Functional Materials* 34.30 (July 2024), p. 2315936. ISSN: 1616-301X, 1616-3028.

[103] W.H. Balmain. "XLVI. Observations on the formation of compounds of boron and silicon with nitrogen and certain metals". en. In: *The London, Edinburgh, and Dublin Philosophical Magazine and Journal of Science* 21.138 (Oct. 1842), pp. 270–277. ISSN: 1941-5966, 1941-5974.

[104] Joshua D. Caldwell et al. “Photonics with hexagonal boron nitride”. en. In: *Nature Reviews Materials* 4.8 (Aug. 2019), pp. 552–567. ISSN: 2058-8437.

[105] Filippo Pizzocchero et al. “The hot pick-up technique for batch assembly of van der Waals heterostructures”. en. In: *Nature Communications* 7.1 (June 2016), p. 11894. ISSN: 2041-1723.

[106] C. R. Dean et al. “Boron nitride substrates for high-quality graphene electronics”. en. In: *Nature Nanotechnology* 5.10 (Oct. 2010), pp. 722–726. ISSN: 1748-3387, 1748-3395.

[107] Igor Aharonovich, Jean-Philippe Tetienne, and Milos Toth. “Quantum Emitters in Hexagonal Boron Nitride”. en. In: *Nano Letters* 22.23 (Dec. 2022), pp. 9227–9235. ISSN: 1530-6984, 1530-6992.

[108] Kenji Watanabe, Takashi Taniguchi, and Hisao Kanda. “Direct-bandgap properties and evidence for ultraviolet lasing of hexagonal boron nitride single crystal”. en. In: *Nature Materials* 3.6 (June 2004), pp. 404–409. ISSN: 1476-1122, 1476-4660.

[109] Darshana Wickramaratne, Leigh Weston, and Chris G. Van de Walle. “Monolayer to Bulk Properties of Hexagonal Boron Nitride”. en. In: *The Journal of Physical Chemistry C* 122.44 (Nov. 2018), pp. 25524–25529. ISSN: 1932-7447, 1932-7455.

[110] G. Cassabois, P. Valvin, and B. Gil. “Hexagonal boron nitride is an indirect bandgap semiconductor”. en. In: *Nature Photonics* 10.4 (Apr. 2016), pp. 262–266. ISSN: 1749-4885, 1749-4893.

[111] Joo Song Lee, Nilanjan Basu, and Hyeon Suk Shin. “Large-area single-crystal hexagonal boron nitride: From growth mechanism to potential applications”. en. In: *Chemical Physics Reviews* 4.4 (Dec. 2023), p. 041306. ISSN: 2688-4070.

[112] Yanqing Guo et al. “Nucleation and growth mechanism of hexagonal boron nitride on metal borides surfaces: A combined theoretical and experimental study”. en. In: *Applied Surface Science* 684 (Mar. 2025), p. 161837. ISSN: 01694332.

[113] Shiqiang Lu et al. “Towards n-type conductivity in hexagonal boron nitride”. en. In: *Nature Communications* 13.1 (June 2022), p. 3109. ISSN: 2041-1723.

[114] Yuejin Wang et al. “Enhancement of p-type conductivity of monolayer hexagonal boron nitride by driving Mg incorporation through low-energy path with N-rich condition”. en. In: *Applied Physics Letters* 116.21 (May 2020), p. 212101. ISSN: 0003-6951, 1077-3118.

[115] Toan Trong Tran et al. “Quantum emission from hexagonal boron nitride monolayers”. en. In: *Nature Nanotechnology* 11.1 (Jan. 2016), pp. 37–41. ISSN: 1748-3387, 1748-3395.

[116] Romain Bourrellier et al. “Bright UV Single Photon Emission at Point Defects in h -BN”. en. In: *Nano Letters* 16.7 (July 2016), pp. 4317–4321. ISSN: 1530-6984, 1530-6992.

[117] M. Mackoit-Sinkevičienė et al. “Carbon dimer defect as a source of the 4.1 eV luminescence in hexagonal boron nitride”. en. In: *Applied Physics Letters* 115.21 (Nov. 2019), p. 212101. ISSN: 0003-6951, 1077-3118.

[118] Clarisse Fournier et al. “Position-controlled quantum emitters with reproducible emission wavelength in hexagonal boron nitride”. en. In: *Nature Communications* 12.1 (Dec. 2021), p. 3779. ISSN: 2041-1723.

[119] Angus Gale et al. “Site-Specific Fabrication of Blue Quantum Emitters in Hexagonal Boron Nitride”. en. In: *ACS Photonics* 9.6 (June 2022), pp. 2170–2177. ISSN: 2330-4022, 2330-4022.

[120] Fariah Hayee et al. “Revealing multiple classes of stable quantum emitters in hexagonal boron nitride with correlated optical and electron microscopy”. en. In: *Nature Materials* 19.5 (May 2020), pp. 534–539. ISSN: 1476-1122, 1476-4660.

[121] Jake Horder et al. “Coherence Properties of Electron-Beam-Activated Emitters in Hexagonal Boron Nitride Under Resonant Excitation”. en. In: *Physical Review Applied* 18.6 (Dec. 2022), p. 064021. ISSN: 2331-7019.

[122] Clarisse Fournier et al. “Two-Photon Interference from a Quantum Emitter in Hexagonal Boron Nitride”. en. In: *Physical Review Applied* 19.4 (Apr. 2023), p. L041003. ISSN: 2331-7019.

[123] Ivan Zhigulin et al. “Photophysics of blue quantum emitters in hexagonal boron nitride”. en. In: *Materials for Quantum Technology* 3.1 (Mar. 2023), p. 015002. ISSN: 2633-4356.

[124] Milad Nonahal et al. “Deterministic Fabrication of a Coupled Cavity–Emitter System in Hexagonal Boron Nitride”. en. In: *Nano Letters* 23.14 (2023), pp. 6645–6650. ISSN: 1530-6984, 1530-6992.

[125] Andreas Gottscholl et al. “Initialization and read-out of intrinsic spin defects in a van der Waals crystal at room temperature”. In: *Nature Materials* 19.5 (Feb. 2020), pp. 540–545. ISSN: 1476-4660.

[126] Sumukh Vaidya et al. “Quantum sensing and imaging with spin defects in hexagonal boron nitride”. en. In: *Advances in Physics: X* 8.1 (Dec. 2023), p. 2206049. ISSN: 2374-6149.

[127] Mehran Kianinia et al. “Generation of Spin Defects in Hexagonal Boron Nitride”. en. In: *ACS Photonics* 7.8 (Aug. 2020), pp. 2147–2152. ISSN: 2330-4022, 2330-4022.

[128] Tieshan Yang et al. “Spin defects in hexagonal boron nitride for strain sensing on nanopillar arrays”. en. In: *Nanoscale* 14.13 (2022), pp. 5239–5244. ISSN: 2040-3364, 2040-3372.

[129] Islay O. Robertson et al. “Detection of Paramagnetic Spins with an Ultrathin van der Waals Quantum Sensor”. en. In: *ACS Nano* 17.14 (2023), pp. 13408–13417. ISSN: 1936-0851, 1936-086X.

[130] Nathan Chejanovsky et al. “Structural Attributes and Photodynamics of Visible Spectrum Quantum Emitters in Hexagonal Boron Nitride”. en. In: *Nano Letters* 16.11 (Nov. 2016), pp. 7037–7045. ISSN: 1530-6984, 1530-6992.

[131] Chao Lyu et al. “Single-photon emission from two-dimensional hexagonal boron nitride annealed in a carbon-rich environment”. en. In: *Applied Physics Letters* 117.24 (Dec. 2020), p. 244002. ISSN: 0003-6951, 1077-3118.

[132] Annemarie L. Exarhos et al. “Optical Signatures of Quantum Emitters in Suspended Hexagonal Boron Nitride”. en. In: *ACS Nano* 11.3 (Mar. 2017), pp. 3328–3336. ISSN: 1936-0851, 1936-086X.

[133] Haidong Liang et al. "Site-Selective Creation of Blue Emitters in Hexagonal Boron Nitride". en. In: *ACS Nano* 19.15 (Apr. 2025), pp. 15130–15138. ISSN: 1936-0851, 1936-086X.

[134] Chi Li et al. "Scalable and Deterministic Fabrication of Quantum Emitter Arrays from Hexagonal Boron Nitride". en. In: *Nano Letters* 21.8 (Apr. 2021), pp. 3626–3632. ISSN: 1530-6984, 1530-6992.

[135] Xiaohui Xu et al. "Creating Quantum Emitters in Hexagonal Boron Nitride Deterministically on Chip-Compatible Substrates". In: *Nano Letters* 21.19 (Oct. 2021), pp. 8182–8189. ISSN: 1530-6992.

[136] Lin Gan et al. "Large-Scale, High-Yield Laser Fabrication of Bright and Pure Single-Photon Emitters at Room Temperature in Hexagonal Boron Nitride". en. In: *ACS Nano* 16.9 (2022), pp. 14254–14261. ISSN: 1936-0851, 1936-086X.

[137] Cesar Jara et al. "First-Principles Identification of Single Photon Emitters Based on Carbon Clusters in Hexagonal Boron Nitride". en. In: *The Journal of Physical Chemistry A* 125.6 (Feb. 2021), pp. 1325–1335. ISSN: 1089-5639, 1520-5215.

[138] Sherif Abdulkader Tawfik et al. "First-principles investigation of quantum emission from hBN defects". en. In: *Nanoscale* 9.36 (2017), pp. 13575–13582. ISSN: 2040-3364, 2040-3372.

[139] Noah Mendelson et al. "Identifying carbon as the source of visible single-photon emission from hexagonal boron nitride". en. In: *Nature Materials* 20.3 (Mar. 2021), pp. 321–328. ISSN: 1476-1122, 1476-4660.

[140] Hamidreza Akbari et al. "Lifetime-Limited and Tunable Quantum Light Emission in h-BN via Electric Field Modulation". In: *Nano Letters* 22.19 (Sept. 2022), pp. 7798–7803. ISSN: 1530-6992.

[141] Hannah L. Stern et al. "A quantum coherent spin in hexagonal boron nitride at ambient conditions". en. In: *Nature Materials* 23.10 (Oct. 2024), pp. 1379–1385. ISSN: 1476-1122, 1476-4660.

[142] Gichang Noh et al. "Stark Tuning of Single-Photon Emitters in Hexagonal Boron Nitride". In: *Nano Letters* 18.8 (June 2018), pp. 4710–4715. ISSN: 1530-6992.

[143] Niko Nikolay et al. “Very Large and Reversible Stark-Shift Tuning of Single Emitters in Layered Hexagonal Boron Nitride”. In: *Physical Review Applied* 11.4 (Apr. 2019). ISSN: 2331-7019.

[144] Simon J. U. White et al. “Electrical control of quantum emitters in a Van der Waals heterostructure”. In: *Light: Science & Applications* 11.1 (June 2022). ISSN: 2047-7538.

[145] Magdalena Grzeszczyk et al. “Electroluminescence from pure resonant states in hBN-based vertical tunneling junctions”. en. In: *Light: Science Applications* 13.1 (July 2024), p. 155. ISSN: 2047-7538.

[146] Mihyang Yu et al. “Electrical charge control of h-BN single photon sources”. In: *2D Materials* 9.3 (June 2022), p. 035020. ISSN: 2053-1583.

[147] Alessio Scavuzzo et al. “Electrically tunable quantum emitters in an ultrathin graphene–hexagonal boron nitride van der Waals heterostructure”. en. In: *Applied Physics Letters* 114.6 (Feb. 2019), p. 062104. ISSN: 0003-6951, 1077-3118.

[148] Corinne Steiner et al. “Current-induced brightening of vacancy-related emitters in hexagonal boron nitride”. en. In: *Physical Review Research* 7.3 (Aug. 2025), p. L032037. ISSN: 2643-1564.

[149] Noah Mendelson et al. “Engineering and Tuning of Quantum Emitters in Few-Layer Hexagonal Boron Nitride”. en. In: *ACS Nano* 13.3 (Mar. 2019), pp. 3132–3140. ISSN: 1936-0851, 1936-086X.

[150] Zhenghan Wu et al. “High-precision AFM cutting of graphene via improved electrode-free local anodic oxidation for electronic band engineering”. en. In: *Nanoscale* 17.44 (2025), pp. 25657–25663. ISSN: 2040-3364, 2040-3372.

[151] Su-Beom Song et al. “Deep-ultraviolet electroluminescence and photocurrent generation in graphene/hBN/graphene heterostructures”. en. In: *Nature Communications* 12.1 (Dec. 2021), p. 7134. ISSN: 2041-1723.

[152] Young Duck Kim. “Electrically driven deep ultraviolet light emission from hexagonal boron nitride van der Waals heterostructures”. In: *Light-Emitting Devices, Materials, and Applications XXVII*. Vol. PC12441. Proceedings of SPIE. Conference Presentation. SPIE, Mar. 2023, PC124410M.

[153] Momoko Onodera et al. "Carbon annealed HPHT-hexagonal boron nitride: Exploring defect levels using 2D materials combined through van der Waals interface". en. In: *Carbon* 167 (Oct. 2020), pp. 785–791. ISSN: 00086223.

[154] K. S. Novoselov et al. "Electric field effect in atomically thin carbon films". In: *Science* 306.5696 (2004), pp. 666–669.

[155] Xiao-Ye Wang, Akimitsu Narita, and Klaus Müllen. "Precision synthesis versus bulk-scale fabrication of graphenes". en. In: *Nature Reviews Chemistry* 2.1 (Dec. 2017), p. 0100. ISSN: 2397-3358.

[156] Satoru Masubuchi et al. "Autonomous robotic searching and assembly of two-dimensional crystals to build van der Waals superlattices". en. In: *Nature Communications* 9.1 (Apr. 2018), p. 1413. ISSN: 2041-1723.

[157] Satoru Fukamachi et al. "Large-area synthesis and transfer of multilayer hexagonal boron nitride for enhanced graphene device arrays". In: *Nature Electronics* 6 (2023), pp. 126–136.

[158] Zengguang Cheng et al. "Toward Intrinsic Graphene Surfaces: A Systematic Study on Thermal Annealing and Wet-Chemical Treatment of SiO2 -Supported Graphene Devices". en. In: *Nano Letters* 11.2 (Feb. 2011), pp. 767–771. ISSN: 1530-6984, 1530-6992.

[159] Yung-Chang Lin et al. "Graphene Annealing: How Clean Can It Be?" en. In: *Nano Letters* 12.1 (Jan. 2012), pp. 414–419. ISSN: 1530-6984, 1530-6992.

[160] Tommi Kaplas et al. "Effect of High-Temperature Annealing on Graphene with Nickel Contacts". en. In: *Condensed Matter* 4.1 (Feb. 2019), p. 21. ISSN: 2410-3896.

[161] Ivan Zhigulin et al. "Stark Effect of Blue Quantum Emitters in Hexagonal Boron Nitride". en. In: *Physical Review Applied* 19.4 (Apr. 2023), p. 044011. ISSN: 2331-7019.

[162] Chi Li et al. "Integration of hBN Quantum Emitters in Monolithically Fabricated Waveguides". In: *ACS Photonics* 8.10 (Aug. 2021), pp. 2966–2972. ISSN: 2330-4022.

[163] Tobias Vogl et al. "Radiation tolerance of two-dimensional material-based devices for space applications". In: *Nature Communications* 10.1 (Mar. 2019). ISSN: 2041-1723.

[164] Mehran Kianinia et al. “Quantum emitters in 2D materials: Emitter engineering, photophysics, and integration in photonic nanostructures”. In: *Applied Physics Reviews* 9.1 (Jan. 2022). ISSN: 1931-9401.

[165] Ralph Nicholas Edward Malein et al. “Stimulated Emission Depletion Spectroscopy of Color Centers in Hexagonal Boron Nitride”. In: *ACS Photonics* 8.4 (Apr. 2021), pp. 1007–1012. ISSN: 2330-4022.

[166] James Callum Stewart et al. “Quantum Emitter Localization in Layer-Engineered Hexagonal Boron Nitride”. In: *ACS Nano* 15.8 (Aug. 2021), pp. 13591–13603. ISSN: 1936-086X.

[167] Xingyu Gao et al. “Femtosecond Laser Writing of Spin Defects in Hexagonal Boron Nitride”. In: *ACS Photonics* 8.4 (Apr. 2021), pp. 994–1000. ISSN: 2330-4022.

[168] Nathan Chejanovsky et al. “Single-spin resonance in a van der Waals embedded paramagnetic defect”. In: *Nature Materials* 20.8 (May 2021), pp. 1079–1084. ISSN: 1476-4660.

[169] Hannah L. Stern et al. “Room-temperature optically detected magnetic resonance of single defects in hexagonal boron nitride”. In: *Nature Communications* 13.1 (Feb. 2022). ISSN: 2041-1723.

[170] Nicholas V. Proscia et al. “Microcavity-coupled emitters in hexagonal boron nitride”. In: *Nanophotonics* 9.9 (May 2020), pp. 2937–2944. ISSN: 2192-8606.

[171] Johannes E. Fröch et al. “Coupling Hexagonal Boron Nitride Quantum Emitters to Photonic Crystal Cavities”. In: *ACS Nano* 14.6 (May 2020), pp. 7085–7091. ISSN: 1936-086X.

[172] Maximilian Ruf et al. “Optically Coherent Nitrogen-Vacancy Centers in Micrometer-Thin Etched Diamond Membranes”. In: *Nano Letters* 19.6 (May 2019), pp. 3987–3992. ISSN: 1530-6992.

[173] Tian Zhong et al. “Nanophotonic coherent light–matter interfaces based on rare-earth-doped crystals”. In: *Nature Communications* 6.1 (Sept. 2015). ISSN: 2041-1723.

[174] Yang Xia et al. "Room-Temperature Giant Stark Effect of Single Photon Emitter in van der Waals Material". In: *Nano Letters* 19.10 (Sept. 2019), pp. 7100–7105. ISSN: 1530-6992.

[175] Xiangzhi Li et al. "Nonmagnetic Quantum Emitters in Boron Nitride with Ultranarrow and Sideband-Free Emission Spectra". In: *ACS Nano* 11.7 (May 2017), pp. 6652–6660. ISSN: 1936-086X.

[176] Simon J.U. White et al. "Optical Repumping of Resonantly Excited Quantum Emitters in Hexagonal Boron Nitride". In: *Physical Review Applied* 14.4 (Oct. 2020). ISSN: 2331-7019.

[177] Maximilian Rühl et al. "Stark Tuning of the Silicon Vacancy in Silicon Carbide". In: *Nano Letters* 20.1 (Dec. 2019), pp. 658–663. ISSN: 1530-6992.

[178] Lorenzo De Santis et al. "Investigation of the Stark Effect on a Centrosymmetric Quantum Emitter in Diamond". In: *Physical Review Letters* 127.14 (Sept. 2021). ISSN: 1079-7114.

[179] Brian Shevitski et al. "Blue-light-emitting color centers in high-quality hexagonal boron nitride". In: *Physical Review B* 100.15 (Oct. 2019). ISSN: 2469-9969.

[180] Ph. Tamarat et al. "Stark Shift Control of Single Optical Centers in Diamond". In: *Physical Review Letters* 97.8 (Aug. 2006). ISSN: 1079-7114.

[181] Péter Udvarhelyi et al. "Spectrally Stable Defect Qubits with no Inversion Symmetry for Robust Spin-To-Photon Interface". In: *Physical Review Applied* 11.4 (Apr. 2019). ISSN: 2331-7019.

[182] Akash Laturia, Maarten L. Van de Put, and William G. Vandenberghe. "Dielectric properties of hexagonal boron nitride and transition metal dichalcogenides: from monolayer to bulk". In: *npj 2D Materials and Applications* 2.1 (Mar. 2018). ISSN: 2397-7132.

[183] J R Maze et al. "Properties of nitrogen-vacancy centers in diamond: the group theoretic approach". In: *New Journal of Physics* 13.2 (Feb. 2011), p. 025025. ISSN: 1367-2630.

[184] L. Weston et al. “Native point defects and impurities in hexagonal boron nitride”. In: *Physical Review B* 97.21 (June 2018). ISSN: 2469-9969.

[185] Viktor Ivády et al. “Ab initio theory of the negatively charged boron vacancy qubit in hexagonal boron nitride”. In: *npj Computational Materials* 6.1 (Apr. 2020). ISSN: 2057-3960.

[186] G. Kresse and J. Hafner. “Ab initio molecular-dynamics simulation of the liquid-metal–amorphous-semiconductor transition in germanium”. In: *Physical Review B* 49.20 (May 1994), pp. 14251–14269. ISSN: 1095-3795.

[187] P. E. Blöchl. “Projector augmented-wave method”. In: *Physical Review B* 50.24 (Dec. 1994), pp. 17953–17979. ISSN: 1095-3795.

[188] John P. Perdew, Kieron Burke, and Matthias Ernzerhof. “Generalized Gradient Approximation Made Simple”. In: *Physical Review Letters* 77.18 (Oct. 1996), pp. 3865–3868. ISSN: 1079-7114.

[189] Gyuna Park et al. “Narrowband Electroluminescence from Color Centers in Hexagonal Boron Nitride”. en. In: *Nano Letters* 24.48 (Dec. 2024), pp. 15268–15274. ISSN: 1530-6984, 1530-6992.

[190] Xiaolong Liu and Mark C. Hersam. “2D materials for quantum information science”. en. In: *Nature Reviews Materials* 4.10 (Oct. 2019), pp. 669–684. ISSN: 2058-8437.

[191] Alberto Boretti et al. “Electrically Driven Quantum Light Sources”. en. In: *Advanced Optical Materials* 3.8 (Aug. 2015), pp. 1012–1033. ISSN: 2195-1071, 2195-1071.

[192] Zhiliang Yuan et al. “Electrically Driven Single-Photon Source”. en. In: *Science* 295.5552 (Jan. 2002), pp. 102–105. ISSN: 0036-8075, 1095-9203.

[193] Xing Lin et al. “Electrically-driven single-photon sources based on colloidal quantum dots with near-optimal antibunching at room temperature”. en. In: *Nature Communications* 8.1 (Oct. 2017), p. 1132. ISSN: 2041-1723.

[194] Li Zhang et al. “Electrically driven single-photon emission from an isolated single molecule”. en. In: *Nature Communications* 8.1 (Sept. 2017), p. 580. ISSN: 2041-1723.

[195] Maximilian Nothaft et al. "Electrically driven photon antibunching from a single molecule at room temperature". en. In: *Nature Communications* 3.1 (Jan. 2012), p. 628. ISSN: 2041-1723.

[196] Svetlana Khasminskaya et al. "Fully integrated quantum photonic circuit with an electrically driven light source". en. In: *Nature Photonics* 10.11 (Nov. 2016), pp. 727–732. ISSN: 1749-4885, 1749-4893.

[197] N. Mizuochi et al. "Electrically driven single-photon source at room temperature in diamond". en. In: *Nature Photonics* 6.5 (May 2012), pp. 299–303. ISSN: 1749-4885, 1749-4893.

[198] A. Lohrmann et al. "Diamond based light-emitting diode for visible single-photon emission at room temperature". en. In: *Applied Physics Letters* 99.25 (Dec. 2011), p. 251106. ISSN: 0003-6951, 1077-3118.

[199] A. Lohrmann et al. "Single-photon emitting diode in silicon carbide". en. In: *Nature Communications* 6.1 (July 2015), p. 7783. ISSN: 2041-1723.

[200] Carmen Palacios-Berraquero et al. "Atomically thin quantum light-emitting diodes". en. In: *Nature Communications* 7.1 (Sept. 2016), p. 12978. ISSN: 2041-1723.

[201] Shi Guo et al. "Electrically Driven Site-Controlled Single Photon Source". en. In: *ACS Photonics* 10.8 (Aug. 2023), pp. 2549–2555. ISSN: 2330-4022, 2330-4022.

[202] Seung Hee Lee et al. "Electroluminescence from h-BN by using Al 2 O 3 /h-BN multiple heterostructure". en. In: *Optics Express* 27.14 (July 2019), p. 19692. ISSN: 1094-4087.

[203] Jun-Ho Lee et al. "Semiconductor-less vertical transistor with ION/IOFF of 106". en. In: *Nature Communications* 12.1 (Feb. 2021), p. 1000. ISSN: 2041-1723.

[204] Yoshiaki Hattori et al. "Determination of Carrier Polarity in Fowler–Nordheim Tunneling and Evidence of Fermi Level Pinning at the Hexagonal Boron Nitride/Metal Interface". en. In: *ACS Applied Materials Interfaces* 10.14 (Apr. 2018), pp. 11732–11738. ISSN: 1944-8244, 1944-8252.

[205] R. H. Fowler and L. Nordheim. "Electron Emission in Intense Electric Fields". en. In: *Semiconductor Devices: Pioneering Papers*. WORLD SCIENTIFIC, Mar. 1991, pp. 683–691. ISBN: 978-981-02-0209-5.

[206] Akbar Basha Dhu-al-jalali-wal-ikram Shaik and Penchalaiah Palla. "Optical quantum technologies with hexagonal boron nitride single photon sources". en. In: *Scientific Reports* 11.1 (June 2021), p. 12285. ISSN: 2045-2322.

[207] Raj N. Patel et al. "Probing the Optical Dynamics of Quantum Emitters in Hexagonal Boron Nitride". en. In: *PRX Quantum* 3.3 (Sept. 2022), p. 030331. ISSN: 2691-3399.

[208] Johann A. Preuss et al. "Resonant and phonon-assisted ultrafast coherent control of a single hBN color center". en. In: *Optica* 9.5 (May 2022), p. 522. ISSN: 2334-2536.

[209] Ding Zhong et al. "Carbon-Related Quantum Emitter in Hexagonal Boron Nitride with Homogeneous Energy and 3-Fold Polarization". en. In: *Nano Letters* 24.4 (Jan. 2024), pp. 1106–1113. ISSN: 1530-6984, 1530-6992.

[210] Daniel Wigger et al. "Phonon-assisted emission and absorption of individual color centers in hexagonal boron nitride". en. In: *2D Materials* 6.3 (Apr. 2019), p. 035006. ISSN: 2053-1583.

[211] Shiyuan Gao, Hsiao-Yi Chen, and Marco Bernardi. "Radiative properties of quantum emitters in boron nitride from excited state calculations and Bayesian analysis". en. In: *npj Computational Materials* 7.1 (June 2021), p. 85. ISSN: 2057-3960.

[212] Ivan Zhigulin et al. "Electrical Generation of Color Centers in Hexagonal Boron Nitride". en. In: *ACS Applied Materials Interfaces* 17.16 (Apr. 2025), pp. 24129–24136. ISSN: 1944-8244, 1944-8252.

[213] Tobias Lühmann, Jan Meijer, and Sébastien Pezzagna. "Charge-Assisted Engineering of Color Centers in Diamond". en. In: *physica status solidi (a)* 218.5 (Mar. 2021), p. 2000614. ISSN: 1862-6300, 1862-6319.

[214] Michal Gulka et al. "Room-temperature control and electrical readout of individual nitrogen-vacancy nuclear spins". en. In: *Nature Communications* 12.1 (July 2021), p. 4421. ISSN: 2041-1723.

[215] Milad Nonahal et al. “Engineering Quantum Nanophotonic Components from Hexagonal Boron Nitride”. en. In: *Laser Photonics Reviews* 17.8 (Aug. 2023), p. 2300019. ISSN: 1863-8880, 1863-8899.

[216] Mihyang Yu et al. “Electrically Pumped h -BN Single-Photon Emission in van der Waals Heterostructure”. en. In: *ACS Nano* 19.1 (Jan. 2025), pp. 504–511. ISSN: 1936-0851, 1936-086X.

[217] Fu-Chien Chiu. “A Review on Conduction Mechanisms in Dielectric Films”. en. In: *Advances in Materials Science and Engineering* 2014 (2014), pp. 1–18. ISSN: 1687-8434, 1687-8442.

[218] J. Frenkel. “On Pre-Breakdown Phenomena in Insulators and Electronic Semi-Conductors”. en. In: *Physical Review* 54.8 (Oct. 1938), pp. 647–648. ISSN: 0031-899X.

[219] A. Schenk. “A model for the field and temperature dependence of Shockley-Read-Hall lifetimes in silicon”. en. In: *Solid-State Electronics* 35.11 (Nov. 1992), pp. 1585–1596. ISSN: 00381101.

[220] U. Chandni et al. “Evidence for Defect-Mediated Tunneling in Hexagonal Boron Nitride-Based Junctions”. en. In: *Nano Letters* 15.11 (Nov. 2015), pp. 7329–7333. ISSN: 1530-6984, 1530-6992.

[221] Alok Ranjan et al. “Molecular Bridges Link Monolayers of Hexagonal Boron Nitride during Dielectric Breakdown”. en. In: *ACS Applied Electronic Materials* 5.2 (Feb. 2023), pp. 1262–1276. ISSN: 2637-6113, 2637-6113.

[222] Matthias Widmann et al. “Electrical Charge State Manipulation of Single Silicon Vacancies in a Silicon Carbide Quantum Optoelectronic Device”. en. In: *Nano Letters* 19.10 (Oct. 2019), pp. 7173–7180. ISSN: 1530-6984, 1530-6992.

[223] Ya-Qing Bie et al. “A MoTe2-based light-emitting diode and photodetector for silicon photonic integrated circuits”. en. In: *Nature Nanotechnology* 12.12 (Dec. 2017), pp. 1124–1129. ISSN: 1748-3387, 1748-3395.

[224] Shunfeng Wang et al. “Efficient Carrier-to-Exciton Conversion in Field Emission Tunnel Diodes Based on MIS-Type van der Waals Heterostack”. en. In: *Nano Letters* 17.8 (Aug. 2017), pp. 5156–5162. ISSN: 1530-6984, 1530-6992.

[225] June-Chul Shin et al. “Electrically Confined Electroluminescence of Neutral Excitons in WSe2 Light-Emitting Transistors”. en. In: *Advanced Materials* 36.14 (Apr. 2024), p. 2310498. ISSN: 0935-9648, 1521-4095.

[226] Yi Zhu et al. “High-Efficiency Monolayer Molybdenum Ditelluride Light-Emitting Diode and Photodetector”. en. In: *ACS Applied Materials Interfaces* 10.50 (Dec. 2018), pp. 43291–43298. ISSN: 1944-8244, 1944-8252.

[227] Xingyu Gao et al. “Single nuclear spin detection and control in a van der Waals material”. en. In: *Nature* 643.8073 (2025), pp. 943–949. ISSN: 0028-0836, 1476-4687.